Energy Research Program

Publishable final report

Program control:
Climate and energy funds

Program management:
Austrian Research Promotion Agency (FFG)

Final Report
created on
21.08.2019

Project title: SilentAirHP

Project number: 848891

Call for Tender	1st Call for Proposals for Energy Research Program
Project Launch	01.10.2015
End of Project	31.03.2019
Total Project Duration (in months)	42 months
Project Holder (Institution)	AIT Austrian Institute of Technology GmbH
Contact Person	DI Dr. Christoph Reichl
Postal Address	Giefinggasse 4, 1210 Wien
Phone	+43 50550 6605
Fax	+43 50550 6679
E-mail	Christoph.Reichl@ait.ac.at
Website	www.ait.ac.at

SilentAirHP

Advanced methods for evaluating and developing noise reduction measures for air heat pumps

Authors:
DI Dr. Christoph Reichl
DI Dr. Johann Emhofer

1 Table of Contents

2 Introduction

2.1 Task Definition

Air-to-water heat pumps (A/W heat pumps) have become increasingly popular in recent years due to their advantages such as small space requirements, comparatively low purchase costs, simple installation, etc. and are among the most sold heat pump systems for heating or cooling residential buildings in Europe. In addition to the annoying noise of the compressor, the high air volume flow required by the heat pump often causes annoying noise from the fan and evaporator. Especially during the transitional season, additional noise is generated due to icing of the evaporator. All these annoying noises often trigger neighbourhood conflicts with health, psychological and financial consequences, and can thus become a competitive disadvantage of the technology in the future and hinder its widespread use, especially in residential areas. The measures currently proposed in the literature, in the acoustic guidelines of heat pump associations, etc. to minimise the disturbing noise emissions include constructive, component-specific, control and active measures, whereby their effect on noise emissions is usually only assessed **qualitatively**. The simultaneous effects of these noise reduction measures on performance, COP (Coefficient of Performance), noise emission and psychoacoustic perception are currently **not quantitatively** evaluated, which means that the heat pump industry (in particular heat pump manufacturers, installers, planners) does not know which of the common measures is most optimal for the heat pump system as a whole.

SilentAirHP therefore primarily aims at **developing advanced numerical and experimental methods for the quantitative evaluation of noise reducing measures for A/W-HP** in order to support national manufacturers in the medium term in the new development or retrofitting of their A/W-HP. In order to achieve this goal, the project will develop acoustic measurement methods which can distinguish and localise sound sources with frequency resolution. In parallel, overall system simulations are carried out which take into account the sound emission (even during icing of the outdoor unit). These models are necessary in order to subsequently develop control engineering noise reduction measures. In addition, a modular L/W heat pump is being built, which is as close as possible to the industry, and which will be used for experimental investigations of noise reduction measures. Besides the quantification of selected "passive" measures, the use of anti-ice coatings for icing and defrosting, as well as noise cancelling as an "active" measure will be tested, adapted and evaluated in the project. Together with the Institute for Sound Research (ÖAW), selected sound reduction measures will also be psychoacoustically analysed and evaluated.

The **project result** comprises on the one hand a **quantitatively evaluated catalogue of measures** for known and novel noise reduction measures, and on the other hand a **detailed**

system description of an A/W-HP is presented, which for the first time can take into account both the icing behaviour and the noise emissions.

The present project was submitted as an individual project because it allows the results to be made **available to all national heat pump manufacturers without restriction**. In order to ensure that national manufacturers have a knowledge advantage over international suppliers, the results were presented continuously at industry events during the project.

2.2 Focus of the Project

The project is divided into four main parts, according to the task definition. These are the numerical method development, the experimental method development, the experimental setup and finally the systematic sound measurements.

The numerical method development focuses on the one hand on system simulation, combining energetic and acoustic approaches. On the other hand, intensive work has been done in the field of 3D modelling with great attention to the icing of the evaporator. The experimental method development includes the acoustic dome, sound localization by means of acoustic microphone rings with a thermal imaging camera and correlated transient vibration, acoustics and flow velocity/turbulence measurements. Furthermore, sound transmission measurements at the heat exchanger were further developed and research was conducted in the field of counter-noise. The systematic sound measurements were carried out on the experimental heat pump by varying different sound reduction measures.

2.3 Fit in the Program

The SilentAirHP project presented in this report has a high degree of coverage with the tendering objectives formulated by the FFG for the 1st Call for Proposals for the Energy Research programme. SilentAirHP makes an important **contribution to meeting the energy, climate and technology policy requirements**. The research work carried out by SilentAirHP is thus suitable for making a significant contribution to the wide market launch of air-to-water heat pumps. Especially in renovated existing buildings in urban settlements, the currently greatest disadvantages of these systems - the noise caused during operation, which increases with icing - can be reduced in the medium term in such a way that there are no significant adverse effects on neighbours or residents and no energy-related disadvantages.
Furthermore, the project results contribute to **increasing the affordability of sustainable energy and innovative energy technologies**. The research work in the project aimed at making the above-mentioned heat pump systems quieter and less noisy in the medium term without reducing the energy performance and therefor increasing the operating costs.
SilentAirHP helps to ensure that Austria's technological leadership and competitiveness in the field of innovative energy technologies is maintained and expanded. This strengthens Austria as a location for innovation and supports the implementation of climate policy goals.

Thus, the project contributes to achieving the goal of **establishing and securing Austria's technological leadership and strengthening its international competitiveness**.

2.4 Methods Used

The following table shows the methods used in the project.

Table 1: Overview of the methods used in SilentAirHP

		gauge	adaption	refinement	development	comment
Transient Local Measurement Methods	Sound Localization + Source Reconstruction	Acoustic Measurement Dome with 60 Microphones + Data Acquisition			X	new Construction of the Test Facility, Implementation of Hardware and Software, Analysis
	Sound Localization	Acoustic Camera	X	X	(X)	Experimental Setup adapted, Experiences collected in the Project
	Vibration	Vibration Sensors	X	X		Adjustments to Data Acquisition
	Image Capturing Techniques	Optical Camera	X			further developed and applied
	Flow Measurements	CTA	X	X		Measurements taken and correlated with microphone and vibration sensors
Transient Global Measurement Methods	Weighing	High Resolution Comparator Scale	X	X		integrated in Data Acquisition
	Electrical energy	Performance Measurement	X			State-of-the-Art
	Pressure	Pressure Sensors	X			State-of-the-Art
	Temperature	PT100, PT1000	X			State-of-the-Art
	Sound Power Level	Microphone	X	(X)	(X)	State-of-the-Art, Implementation of Time-Synchronous Data Acquisition and Analysis Methods

	Mass Flows	Coriolis Mass Flow Sensors, Ind. Volume Flow Sensors CTA	X			State-of-the-Art
Numeric Methods	Sound Localization	-			X	Development within the Project Testing
	1D System Simulation	-			X	Development based on Work from previous AIT Projects in Air Duct Acoustics, new Development for Air Heat Pumps
	Flow Calculations		X			State-of-the-Art, requires Adaptation to the experimental Setup

2.5 Structure of the Work

The work carried out within the framework of the project presented here thus forms an interplay of experimental work using modern scientific methods, supplemented by computer-aided models for the integration and evaluation of the data obtained. The exact procedure with presented content in detail, the obtained results and conclusions as well as an outlook with recommendations and a catalogue of measures are described below.

3 Content Representation

3.1 Numerical Method Development

Development of the sound localization analysis

A prototype of the acoustic camera (see Figure 1 left) was built, calibrated and prepared for first test measurements on a test heat pump. The 64 microphones were connected to the same data acquisition system that was used for the acoustic dome (acoustic measurement cupola). The analysis of the measured data (see Fig. 1 right) enabled the visualization of sound sources directly on a computer model of the heat pump (see Fig. 3). [1] [2] [3] [4]

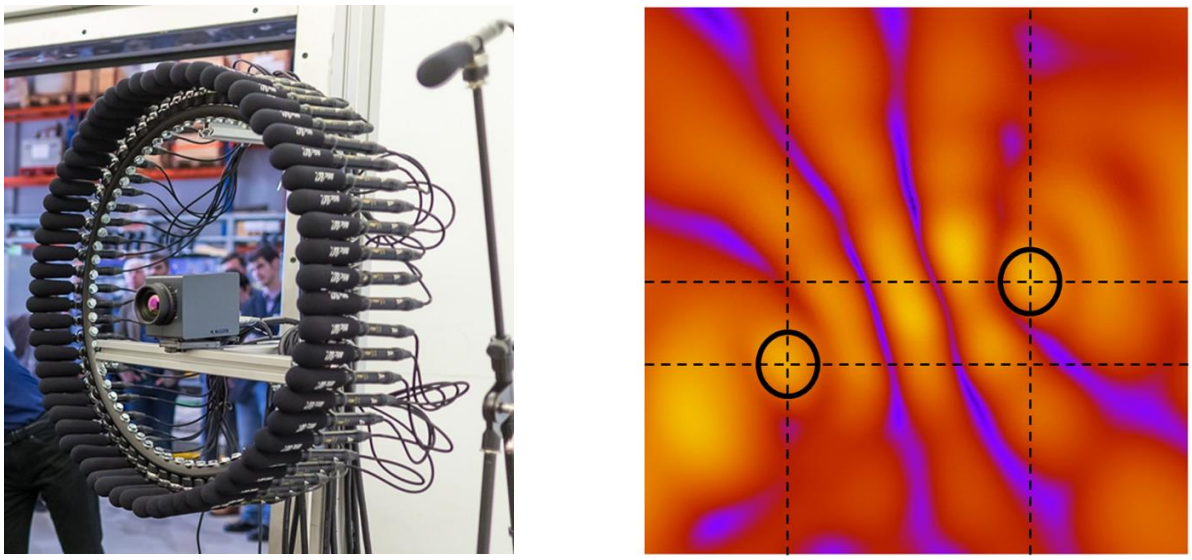

Figure 1: (left) Setup of the prototype of the acoustic camera with centrally mounted thermal camera; (right) Analysis of the measurement data of a test measurement of two uncorrelated sound sources at slightly different heights

A much more precise version of the acoustic camera could be built (see Figure 2) and put into operation. Final calibration work was successfully completed. [5]

Figure 2: Construction of the high-precision variant of the acoustic camera. The right picture shows the positioning mechanism.

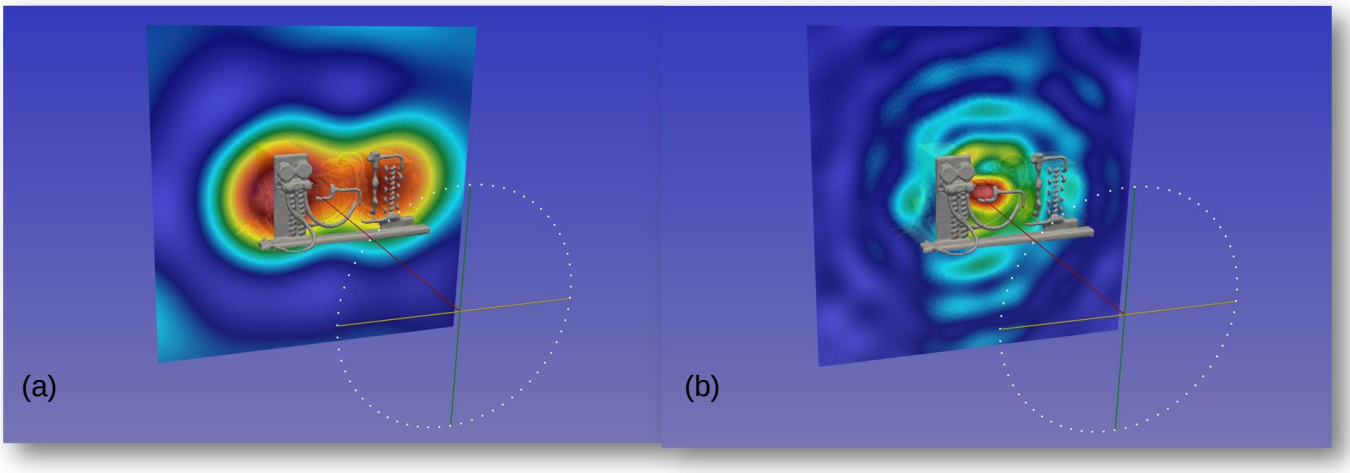

Figure 3: 3D visualization of the sound emissions of an experimental heat pump at (a) 1250 Hz and (b) 4000 Hz. The dotted circle in the foreground symbolizes the acoustic camera.

Development of the energetic 1D model of the A/W-HP

A dynamic 1D model of the heat pump was created using the description languages Dymola/Modelica [6] [7]. Two different libraries providing heat pump models were investigated. One is the commercially available TIL library [8] and the other is the freely available ThermoCycle library [9]. Finally, the TIL library was preferred, because with this library it was possible to realize the circuit with a four-way valve for circuit reversal. Figure 4 shows a simulation of the SilentAirHP at a stable operating point. The models created in this way have about 10 000 equations and around 100 state variables. They have already been used to design the SilentAirHP and to test the control with conventional PI controllers.
It has also been investigated whether the models can be used for model-based control without much effort. Due to the large number of state variables, however, this is not possible at present.

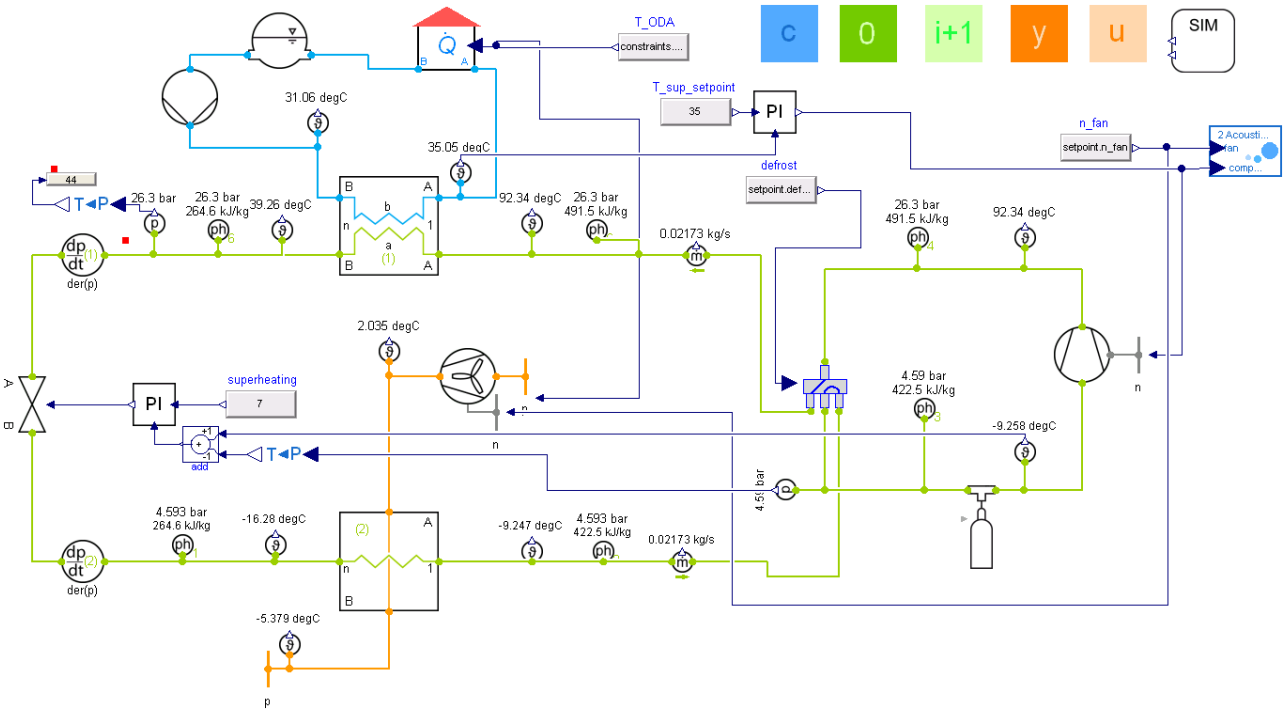

Figure 4: Simulation of SilentAirHP at design point A2W35.

Extension of the energetic 1D model of the air-to-water heat pump

Furthermore, the components with the highest noise emissions (compressor, fan, air duct) were extended from the existing models to analyse the acoustic effects at different operating points (see also Figure 5). In addition, new components have been developed which can be connected to the extended components in Modelica to represent the noise reduction. It was important that the acoustic extensions are not only applicable to the components of the TIL library, but that any other Modelica components can be extended with acoustic sound functions. The resulting *Sound Source Extension* (SSE-) Library [10] is freely available within the scope of the Modelica License 2 model.

A simplified model of ice growth at the evaporator was also developed and validated from existing detailed models. From this model, the increasing pressure loss and the deteriorating heat conduction at the evaporator during icing can be simulated. The increased pressure loss in turn has an effect on the control and therefore on the fan speed and finally on the sound.

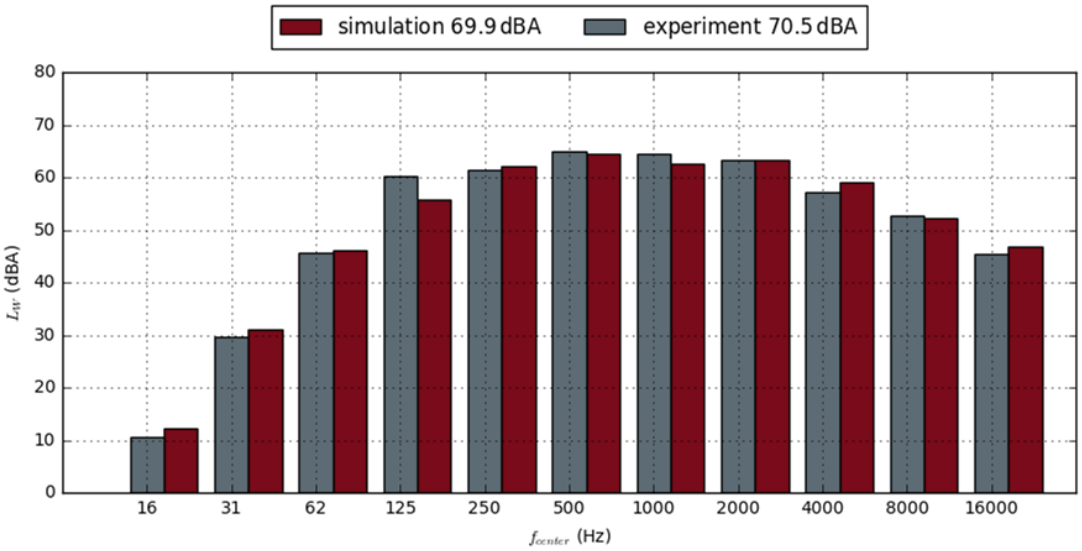

Figure 5: Comparison of experimental data of the SilentAirtHP with simulation results of the first test measurements from April 2017: The individual components were measured and the total sound power level was compared.

The functionalities available in SilentAirHP are summarized in Table 2.

Table 2: SilentAirHP extensions realized in Modelica

Component	Type	Method
Compressors	Extension of the Existing Model	Frequency Band-Resolved Sound Characteristic
Compressor Encapsulation	New Component	Frequency Band-Resolved Sound Absorption
Structure-Borne Noise Damper	New Component	Frequency Band-Resolved Sound Absorption
Fan	Extension of the Existing Model	Frequency Band-Resolved Sound Characteristic
Air Duct	New Component for Airborne Noise Reduction (straight)	Frequency Band-Resolved Sound Absorption
Air Duct	New Component Deflection Silencer	Frequency Band-Resolved Sound Absorption over Characteristic Curves from Manufacturers
Evaporator	Extension of the Existing Model	Icing Models

Development of the control strategy

Since some control-related questions had already arisen during the planning of the experimental heat pump, the simulation of a simple control system was started at an early stage of the project. At this time, two PI controllers for controlling the flow temperature and superheat were simulated. The acoustic control was carried out on a sound source (fan) by means of control on the fan speed. In a further step, the coupling of different sound sources followed. A control based on the fan speed was implemented and tested. However, no significant advantages could be achieved in the test heat pump, since the noise emissions of the compressor predominate [11].

Furthermore, it was found that a model-based control approach with simplified models can be used to calculate a maximum night reduction of the compressor speed. In other words, if the compressor is the loudest component (as in the case of the SilentAirHP), the heat pump's demand for heating/cooling energy can be divided during part load operation for one day in such a way that the heat pump runs at full load during the day and operates at the lowest possible thermal output and thus at low compressor speed or sound power overnight. How far the speed can be reduced depends on a number of external parameters such as outside temperature, heating/cooling load, etc.

Calibration of the 1D models

The calibration was carried out with the results of the measurements.

Flow model

At the beginning of the project, simulations of the icing of the SilentAirHP heat exchanger were already carried out (see Figures 6 and 7). Furthermore, numerous simulation calculations were carried out and evaluated [12].

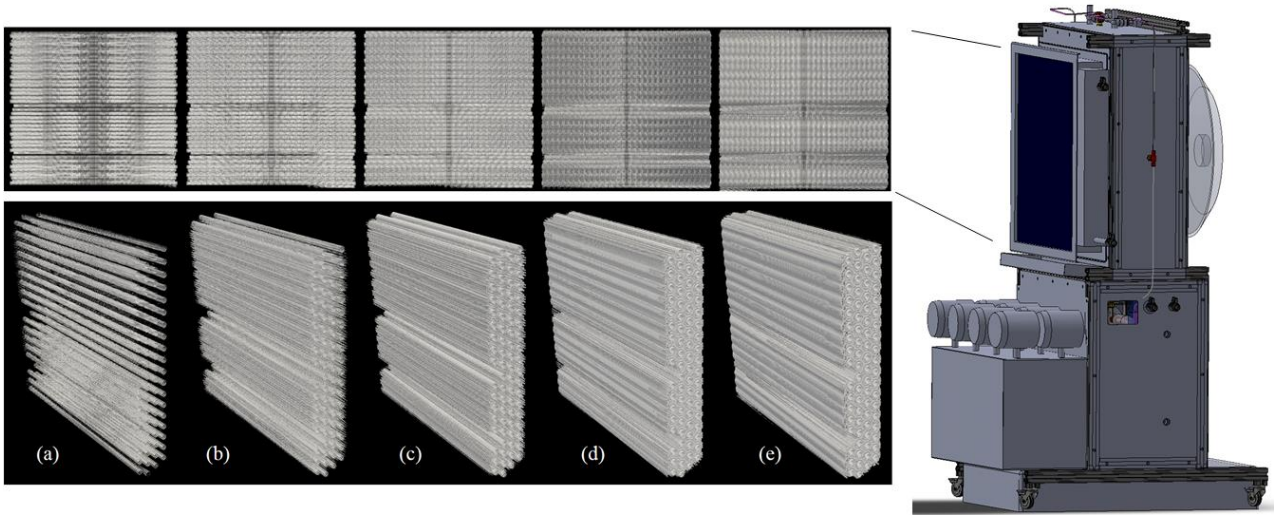

Figure 6: Temporal behaviour of the ice build-up on the SilentAirHP heat exchanger.

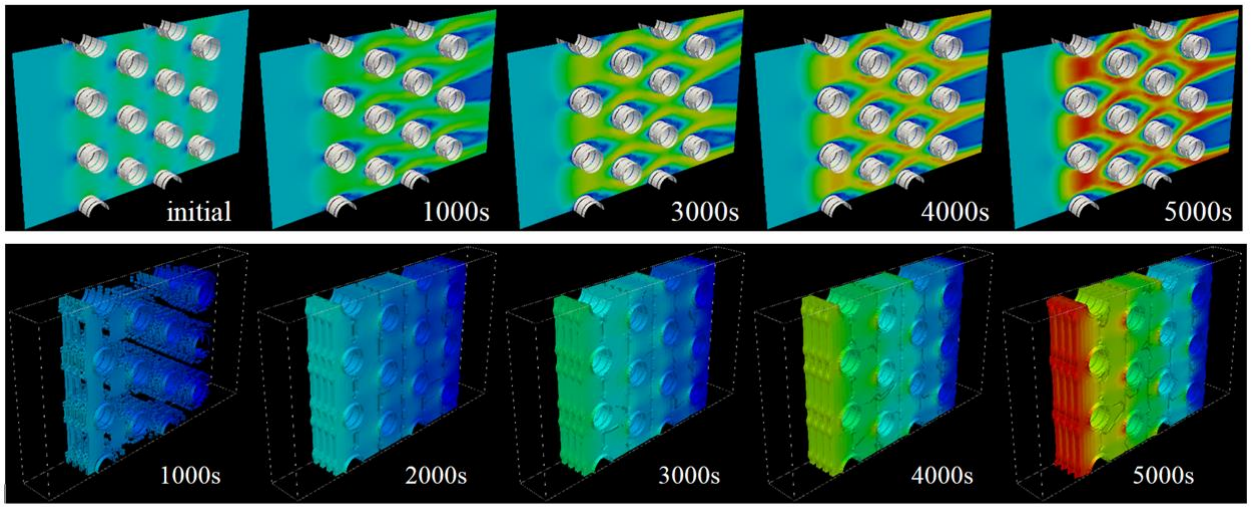

Figure 7: Temporal behaviour of the ice build-up on a small symmetrical section of the heat exchanger. At the top, the flow velocity is shown, below the pressure loss with gradual icing.

The time-dependent icing of the heat exchanger in the SilentAirHP heat pump was observed by measuring the mass increase and analysing the captured images of the heat exchanger during icing to extract the frost layer thickness. After the implementation of the icing model, the methodology was applied to calculate frost (i) on the entire heat exchanger assembly according to the experimental setup and (ii) for a comprehensive parameter study on a symmetrical part of the heat exchanger. The parameter study includes different tube and fin temperatures, different mass flows through the heat exchanger and different boundary conditions on the air supply side of the heat exchanger, which influence the absolute water content in the supply air. The results of the symmetrical parameter study were used to reconstruct the behaviour of the entire heat exchanger design. Experimental observations were finally compared with both the reconstructions and the simulations with the entire heat exchanger design.

The icing of the SilentAirHP heat transfer has been analyzed with different experimental techniques. These include thermodynamic measurements for the thermal operating parameters of the heat pump, weight measurements using a scale and image acquisition techniques from standard cameras and thermal cameras to visualise ice growth and extract the frost layer thickness.

The temperature at the refrigerant inlet and outlet of the evaporator was measured with calibrated temperature sensors of PT100 class A. The sensors were mounted as close as possible to the inlet using thermal paste on the outside of the copper tubes. In addition, the sensors were insulated to reduce heat exchange with the ambient air.

The heat pump assembly was placed on a scale capable of measuring weight as a function of time. By calculating the difference between the increasing weight and the initial weight, the frost quantity on the heat exchanger can be extracted. As the weight of the heat pump assembly was 1.5 times higher than the maximum load of the scale, a force transmitter was installed and the system was calibrated by placing known weights on the dry heat exchanger

and recording a calibration curve before the icing tests were started.

Two cameras were used to capture the frost formation on the heat exchanger: A thermal imaging camera capable of recording thermographic still images and standard still images simultaneously, and a camcorder that records a detailed view of a part of the heat exchanger used to extract the frost layer thickness. The detailed camcorder was tilted at 45 degrees to the heat exchanger normal (and main flow direction). The distance between the fins is given by 4 mm, so that the camera only sees a reference distance of 2.83 mm (see Fig. 8). Since the fins of the heat exchanger are positioned vertically and the camcorder has been aligned with an exact horizontal viewing axis for detailed video, the fins of the heat exchanger are reproduced parallel to the pixel rows of the images. This makes it possible to calculate sums of rows (horizontal, blue) and columns (vertical, green) across the pixels (see Figure 9). The column totals (shown in green in Figure 9) show the periodicity of the fins. The line totals (shown in blue in Figure 9) show the influence of the refrigerant pipes, which are arranged at four different depths, whereby the two nearest pipes with their lower temperature lead to an increase in the frost layer thickness. The difference between these areas decreases as more and more frost accumulates.

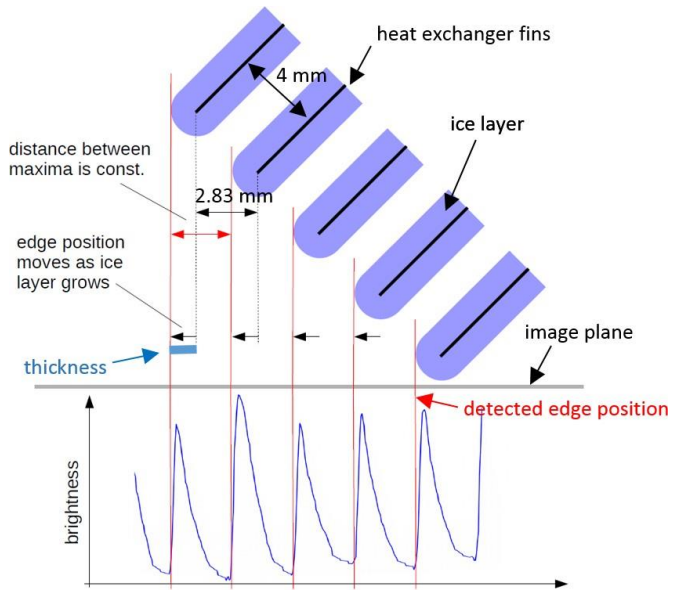

Figure 8: Method for extracting the frost layer thickness based on image acquisition. The pixels of the camera show increased brightness during the icing of the slats. Taking into account the inclination of the camera to the heat exchanger is 45 degrees, a frost layer thickness can be calculated using an edge detection algorithm.

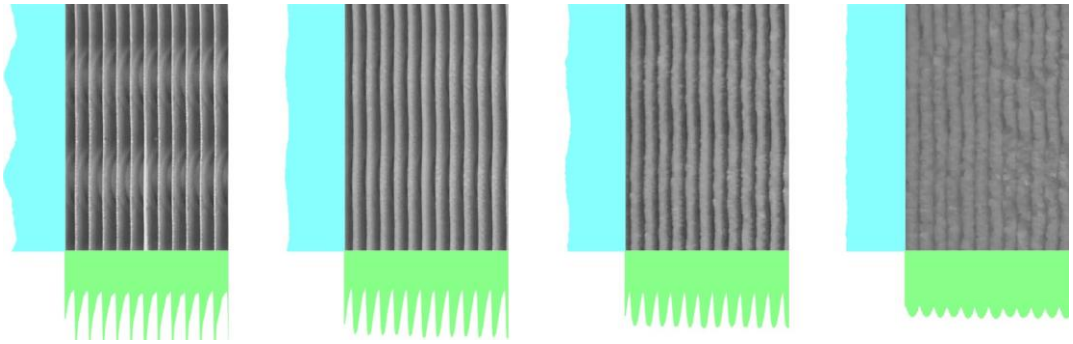

Figure 9: Detailed view of the frost layer recorded by a camcorder for four different times during the icing process. Vertical sums over the green image pixel columns show the periodicity of the slats; Horizontal sums over the image pixel columns show the influence of the tubes on the frost formation due to their low temperature.

Assuming that frost grows evenly around the slats, the position of the moving edge in the image (using the brightness of the image) allows the frost layer thickness to be calculated. This calculation is performed using a projection of the slat distance to the image plane. Frost mass and frost layer thickness increase as a function of time during subsequent icing of the heat exchanger. The growth rate is linear in several parts, which leads to a "natural" separation into several time ranges (see grey vertical lines in Fig. 10). For each of these parts the weight increase (blue) and the frost layer thickness (red) are constant. The weight divided by the frost layer thickness (shown in yellow) corresponds to the density of the newly grown frost layer, assuming that the existing frost remains unchanged. In the last part of the measurement (after about 3 hours) the relative humidity was increased by additional humidifiers to achieve the maximum matting. The suddenly available moisture leads to a sudden increase in the frost layer thickness without significantly influencing the weight gain, resulting in a low density of the additional frost (small yellow area in Fig. 10 at time 3:05).

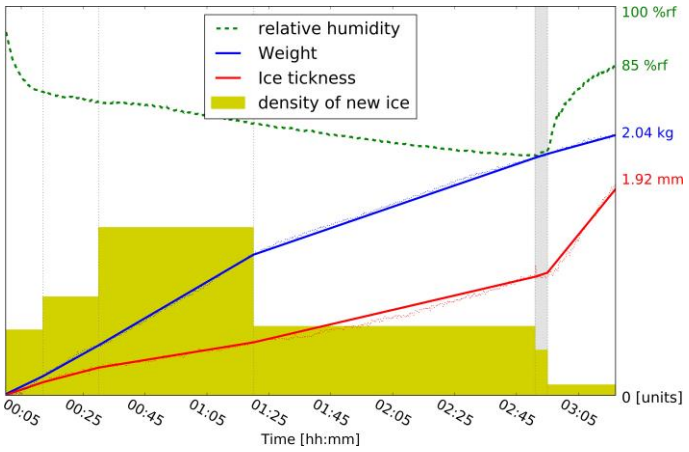

Figure 10: Frost mass, ice layer thickness and calculated frost density of the new ice layer as a function of time. After about 3 hours of frost accumulated, the relative humidity was quickly increased by additional humidifiers in order to achieve full icing.

The four-row SilentAirHP heat exchanger including the volume between the heat exchanger and the fan was modelled. Temperature, flow field and frost layer were calculated with the

Navier-Stokes solver OpenFOAM®, which was extended with a custom icing code. The fan was not modeled with its real geometry, but with a suitable boundary condition. On the one hand the geometric models are described (with a summary of the boundary conditions used for the simulations), on the other hand the icing model and its implementation in OpenFOAM® is described and the calculations and numerical results are presented. Two geometric models have been constructed: a complete SilentAirHP heat exchanger model and a smaller fully symmetric part of the heat exchanger. The geometry and mesh generation was realized with snappyHexMesh and is fully automated and parameterized. [13]

The complete heat exchanger model includes a representation of the four-row SilentAirHP shell-and-tube heat exchanger. This includes fins and tubes. This model does not include the half-round tube connectors on the sides. The refrigerant flow was not modeled. Instead, the temperature boundary conditions for the probes on tubes and fins were defined. An additional air volume between the heat exchanger and the fan with a depth of 300 mm is also included. Fig. 11 shows the geometrical layout of the complete heat exchanger model (left) and a detailed view of the heat exchanger (right). The network consists of about 11 million computing cells.

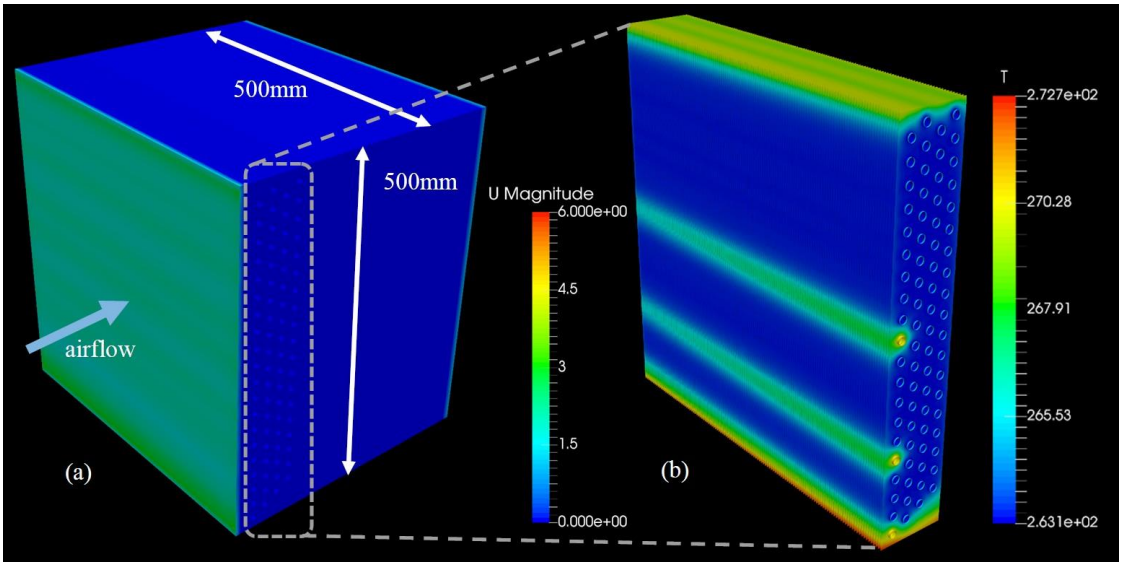

Figure 11: Geometric structure for complete heat exchanger simulations. The areas in the left figure (a) are colored with the velocity amount, which shows a slightly uneven distribution on the air supply side (left side) due to the asymmetrical geometrical arrangement of the heat exchanger. The dashed bounding box marks the position of the heat exchanger, which is enlarged in the right figure (b). There the fin and tube surfaces are coloured with the corresponding temperature according to configuration A.

A symmetrical extraction of the heat exchanger was set up for parametric investigations of the dependence of the frost accumulation on the fin temperature and the boundary conditions on the supply air side (temperature and humidity) (see Fig. 12 left). It contains the full depth of the heat exchanger of 120 mm, but has only four tube rows (one of which is divided into two halves) and four fins with a total width of 16 mm. Figure 12 right shows a

detail of the rake network with 16 cell layers between two fins. Depending on the number of cell layers between the fins, the total cell count of the symmetrical meshes ranges from 269,000 (4 layers), 534,000 (8 layers) to a maximum of 1.1 million cells for 16 layers.

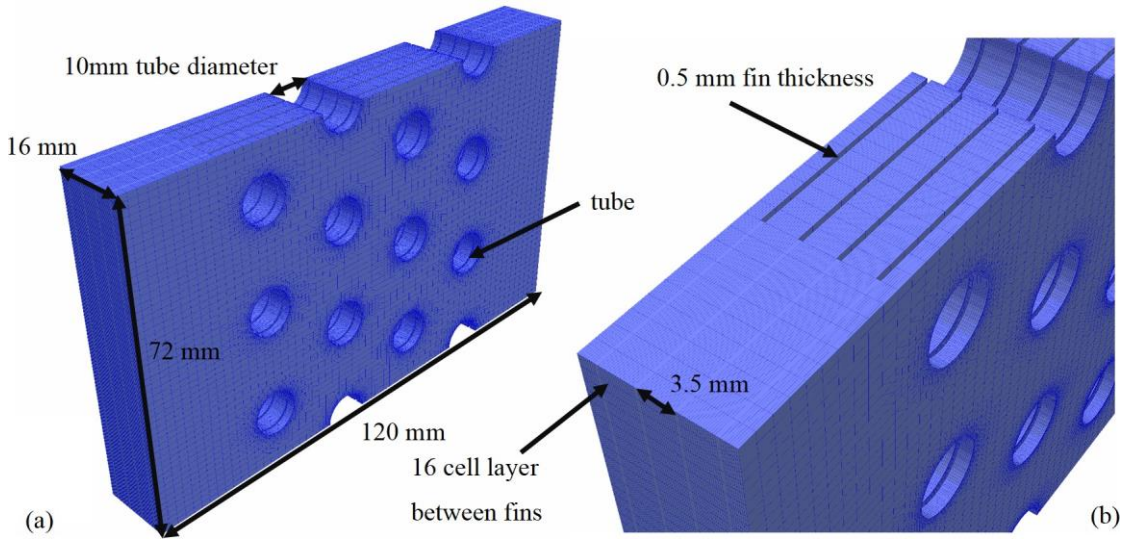

Figure 12: (a) Symmetrical part of the heat exchanger with a total depth of 120 mm, containing all 4 tube layers in the direction of flow. In this model there are 4 fins and 12 tubes (10 and 4 halves, which are divided for symmetry reasons). (b) Detailed view showing the computing network with 16 cell layers between two ribs.

The boundary conditions include the temperatures at the fin, tubes and the inlet and outlet side of the heat exchanger assembly. Furthermore, velocity profiles on the discharge side must be set at the location of the fan. Humidity was set on the air supply side.

Two temperature configurations (configuration A and B) were used to simulate the total heat exchanger assembly. Configuration A (see Fig. 13 a, b) corresponds to the test setup with an evaporating refrigerant, while configuration B (Fig. 13 c, d) corresponds to a fictitious setup with a non-evaporating fluid as refrigerant, resulting in a linear temperature distribution along the tubes. Fig. 13 right shows the temperature at tubes and fins for configuration A. Fig. 17 shows an isometric view of the fin plane with temperature configuration B.

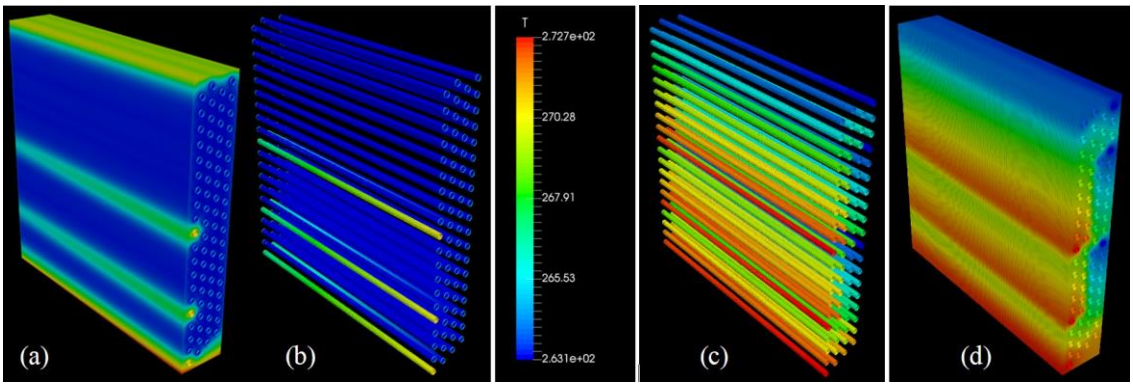

Figure 13: Temperature boundary conditions on the pipes for configuration A (b) and B (c). After solving the temperature diffusion equation (Laplace equation) the temperature profiles at the fins are extracted and visualized for configuration A (a) and B (d).

In the heat exchanger arrangement the air flow is driven by a fan on the exhaust side. The off-center moment introduced by the fan was modeled either by a swirl boundary condition (see Fig. 16) or at a constant velocity on the air supply side for temperature configuration A. The differences are only small and the resulting velocity distribution on the air outlet side of the heat exchanger is shown in Fig. 14 a. A different fan boundary condition was also tested and is shown for temperature configuration B in Fig. 15 a.

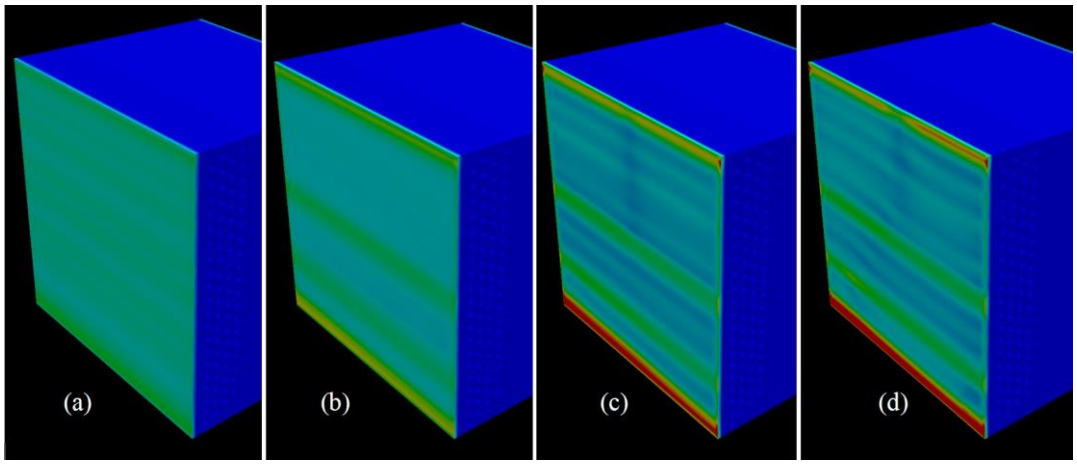

Figure 14: Fin and tube temperature configuration A. Velocity amount on the exhaust air side (colour range 0 - 6m/s) for 4 different times during subsequent icing of the heat exchanger.

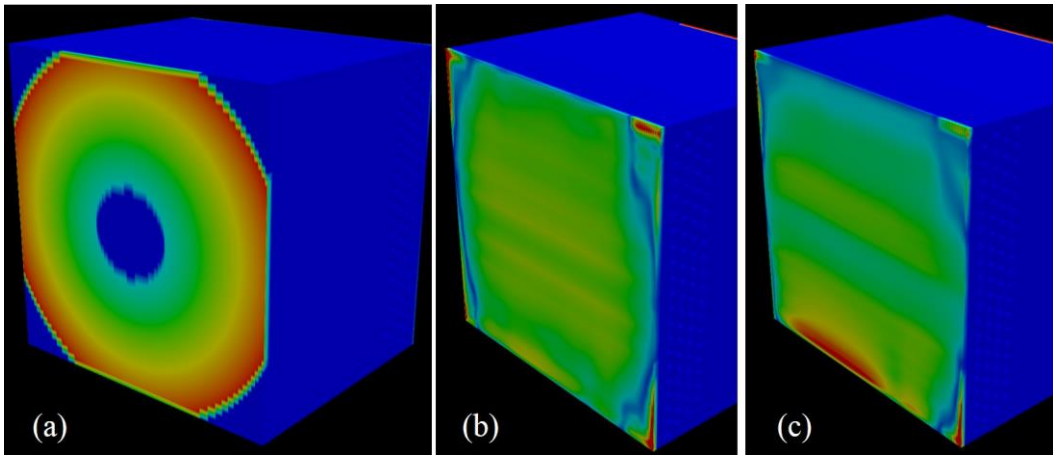

Figure 15: Fin and tube temperature configuration B. (a) Velocity amount on the air suction side (colour range 0 - 30m/s). (b, c) Velocity amount on the air supply side (colour range 0 - 4m/s) for two different times during subsequent icing of the heat exchanger.

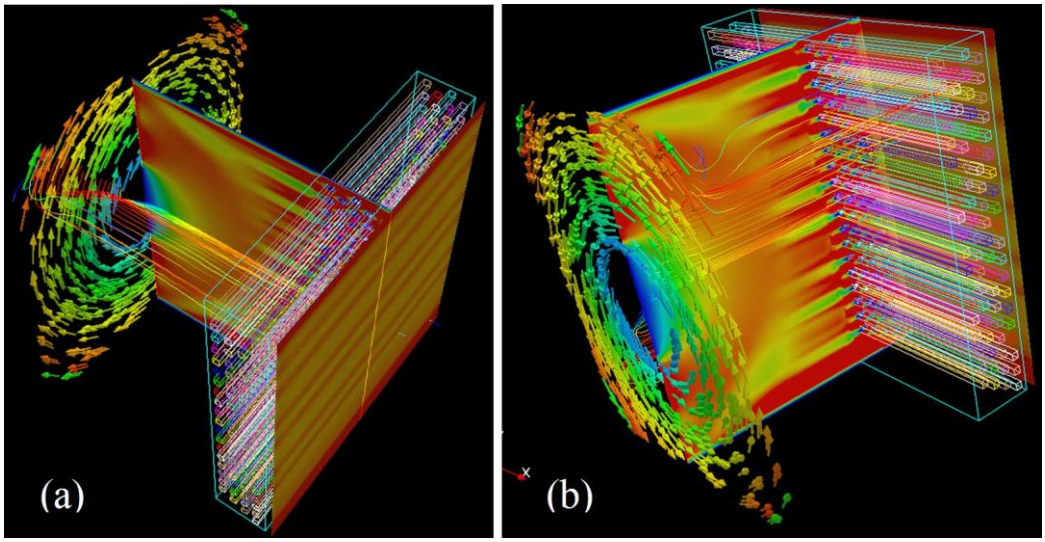

Figure 16: Swirl boundary condition to simulate the fan on the exhaust side of the simulation area. Vectors, streamlines and contour diagrams are colored with a velocity amount in the range of 1-3m/s. The velocity reaches values up to 20m/s.

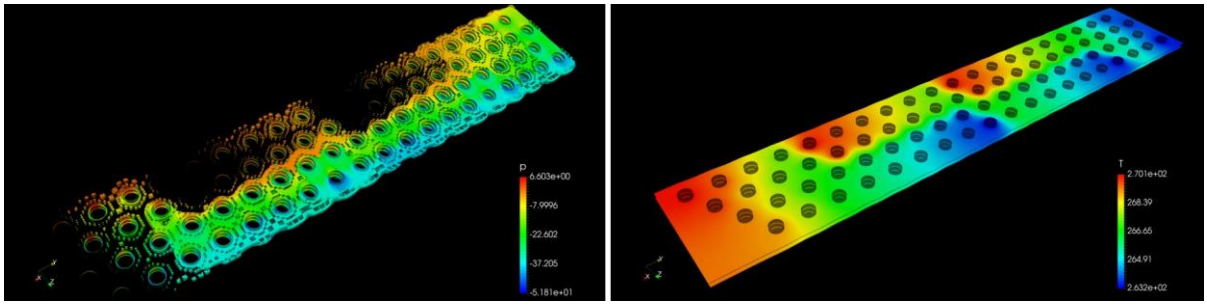

Figure 17: (left) Accumulated frost mass, coloured according to the static pressure for setting the fin and tube temperature configuration B; (right) Temperature boundary condition at the fins for configuration B.

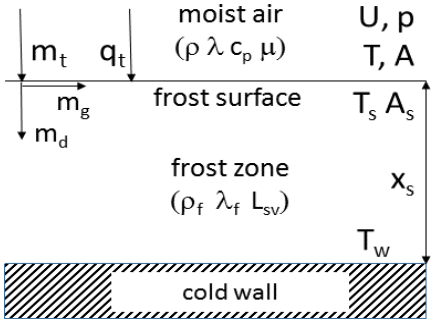

Abbildung 18: The parameters of the icing process.

The key data of the icing process considered in this paper are outlined in Fig. 18. During this process, humid air flows over a cold wall, and a frost zone is created by the heat and mass transfer over the frost surface. The analysis of frost growth over a cold wall starts with the equilibrium of the total mass flow of water vapour, which is transferred from the surrounding moist air over the frost surface into the frost zone:

$$\dot{m}_t = \frac{d}{dt}(x_s \rho_f) = \underbrace{\rho_f \frac{dx_s}{dt}}_{\dot{m}_g} + \underbrace{x_s \frac{d\rho_f}{dt}}_{\dot{m}_d} = h_m(A - A_s) \qquad (1)$$

Where ρ_f [kg/m3] is the frost density, x_s[m] the thickness of the frost zone, hm[m/s] the mass transfer coefficient, while A[kg/m3] and As[kg/m3] represent the absolute humidity in the surrounding humid air and at the frost surface, respectively.

The balance given in equation (1) states that the total mass flow $\dot{m}$ t, which comes from the surrounding humid air (last term on the right), can consist of two parts: one that diffuses into the existing frost zone and changes its thickness ($\dot{m}$g), and the other that compresses the frost ($\dot{m}$d). For the integration of equation (1) it is assumed that the mass transfer within the frost zone is quasi-stable and one-dimensional (growing only in the direction normal to the wall). The frost density is defined by an empirical function depending on the frost surface temperature Ts[K]:

$$\rho_f = a_{\rho_f} e^{b_{\rho_f} t_s} \qquad (2)$$

Where the empirical function requires the frost surface temperature given in Celsius $t_s = T_s - 273.15$ [oC] and $a_{\rho f} = 650$ [kg/m3] and $b_{\rho f} = 0.277$ [oC-1] are the empirical coefficients.

In the literature, the validity of the empirical correlation has been tested in the temperature range $25°C < t_s < 0°C$, while other correlations can also be found for different icing conditions. For simplicity, in the present work, however, Eq. (2) is used because it allows a simple conversion of the derivation of the frost density time in relation to the frost growth rate. Assuming that the frost properties are constant over the entire frost zone, the frost growth rate is obtained by calculating the derivative of Eq. (1) and introducing it in Eq. (2):

$$\frac{dx_s}{dt} = \frac{h_m(A - A_s)}{\rho_f[1 + b_{\rho_f}(T_s - T_w)]} \qquad (3)$$

With T_w[K] representing the temperature of the cold wall. The frost growth rate from Eq. (3) is used to update the actual thickness of the frost zone at each time step.

The heat balance over the frost surface indicates that the total energy qt (last term on the right) transferred from the surrounding humid air consists of the conduction through the frost zone qc and the latent sublimation heat within the frost zone ql:

$$\dot{q}_t = \underbrace{\lambda_f \left.\frac{dT}{dx}\right|_s}_{\dot{q}_c} + \underbrace{\dot{m}_t L_{sv}}_{\dot{q}_l} = h_c(T - T_s) \qquad (4)$$

Where hc [m/s] is the heat transfer coefficient, while the frost conductivity λ_f [W/mK] and the latent heat of sublimation L_{sv} [kJ/kg] are empirically defined.
Assuming that the frost properties remain constant along the thickness of the frost zone (Eq. 2 and 5), the introduction of Eq. (1) in Eq. (4), the following expression is obtained for the

temperature of the frost surface T_s after a small rearrangement.

$$T_s = \frac{T_w + \frac{x_s}{\lambda_f}\left[h_c T + h_m (A - A_s) L_{sv}\right]}{1 + \frac{h_c x_s}{\lambda_f}} \qquad (6)$$

With T [K] being the temperature of the surrounding humid air. The analytical integration of Eq. (4) has been carried out in the literature and it has been found that the result in the form of Eq. (6) is obtained, after the negligible term describing the variation of frost properties in the entire frost zone has been dropped.

As in Eq. (1) to Eq. (6), frost growth is controlled by the heat and mass transfer balance (reflected by the coupled terms for frost thickness and surface temperature), with the moisture difference between the moist air and the frost surface acting as a frost growth driver. Therefore, Eq. (3) and eq. (6) must be solved iteratively in addition to the expression for the absolute humidity at the frost surface. In order to conclude the set of model equations, the heat transfer coefficient h_c is defined using the Nusselt analogy, while the Lewis analogy was used for the mass transfer coefficient hm.

The icing model is implemented in such a way that frost growth is derived from the local flow properties taking into account the spatial and temporal distribution of the relevant humid air flow variables: velocity U, temperature T and absolute humidity A. The entry of frost on a cold wall is controlled by the nucleation theory. After this initial phase, however, the frost surface moves in the direction normal to the wall, and the newly formed layer between the cold wall and the frost surface is treated as porosity: There the humid air flow is blocked and the swell/sink term is introduced into the transport equations for temperature and absolute humidity.

For each cell in the numerical network, the frost zone is quantified by the ratio of the locally calculated frost thickness x_s and the height of the cell Δx. Thus the defined quantity has a value between zero (the cell is frost-free) and one (the cell is filled with frost). Consequently, according to Darcy's definition of pressure drop for flows through porous media, the blockage of the humid air flow will be relatively small when the frost starts to fill the cell and grow exponentially when the cell is fully frozen. This is reflected in the results when considering the total pressure drop: It grows slowly, as the frost thickness above the slats is relatively small, and shows a sudden jump, as the majority of the cells along the slats become almost full of ice (this behavior is reduced when the mesh is refined).
With the explained frost model, various parametric studies with simulations on the symmetric model were initially carried out. Simulations with the complete heat exchanger assembly followed. Several total heat exchanger simulations were calculated with the Vienna Scientific Cluster VSC 3. It consists of 2020 nodes with liquid-immersion cooling using the Intel Xeon

IvyBridge-EP E5-2650v2 processor with 2.60 GHz (8 cores, 20 MB cache). Each calculation was performed in parallel with 64 cores. The symmetrical simulations were calculated in parallel with an Intel i7-6800K HEXcore processor with 3.4 GHz and 32 GByte memory. Typical calculation times for the complete heat exchanger simulations on the VSC were three days, depending on the number of cell layers. The symmetrical calculations required calculation times between several hours and one day.

Fig. 19 shows the development over time during icing for the reference case: The fin and pipe temperature was set at a value of 263 K, the boundary conditions on the air supply side are a relative humidity of 90%, a temperature of 275 K and a block profile flow speed with the amount of 2 m / s. Frost is visualized by an iso surface of the constant αf which is set to a value of 0.5. During icing, more and more volume is filled with frost (which is indicated by the accumulated frost). As a result, the pressure also rises (in the illustration, the frost is colored according to the local pressure value), which ultimately leads to a sharp drop in pressure across the heat exchanger. As more and more volume is occupied by frost, the flow velocity increases so that the mass flow can remain constant. This mass flow must of course be provided by the fan. Because the fans normally operate in operating curves (instead of providing a constant mass flow), which have a non-linear dependency between pressure and mass flow, the flow velocities will eventually decrease in severe frost conditions.

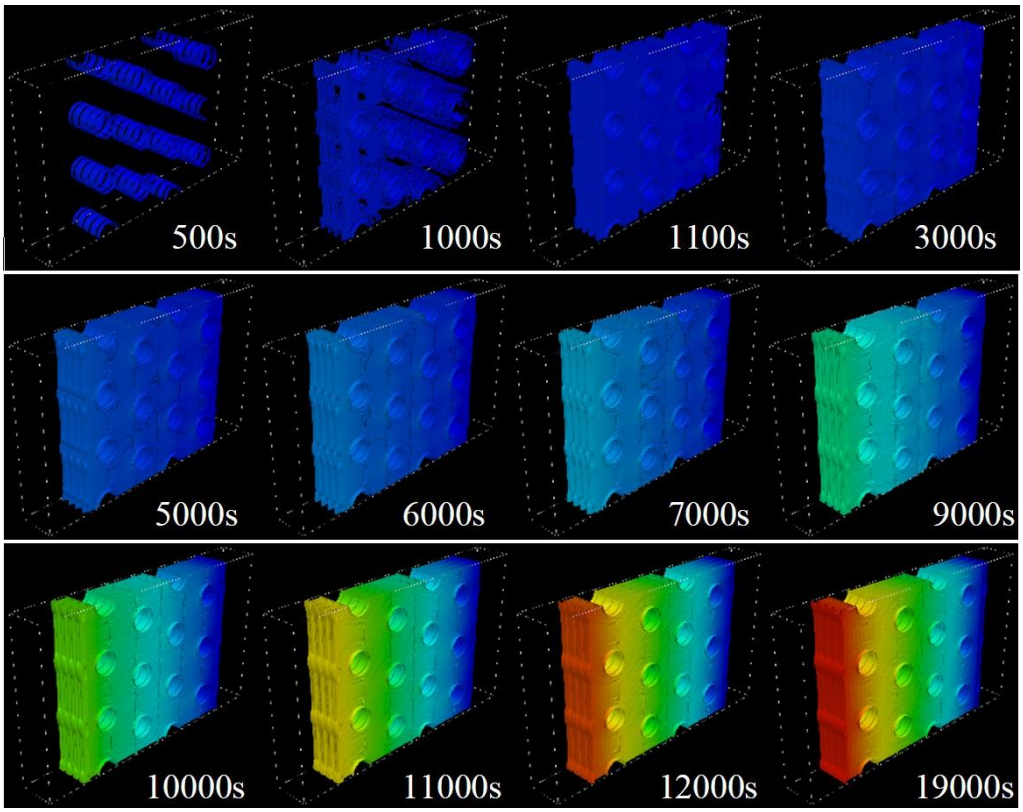

Figure 19: Accumulated frost mass, coloured according to the static pressure (colour range 5 to 2000Pa) for different times during the subsequent icing of the heat exchanger. The following boundary conditions are defined on the air supply side: Temperature 275K, relative humidity 90%, speed 2m/s. The tube and fins are fixed at 263K. Frost is visualized by an isosurface of the constant αf, which is set to a value of 0.5. The flow direction is from left to right.

The change in fin and tube temperature has a great influence on the speed of the icing process. This can be seen in Fig. 20. Here the frost accumulation for fin and tube temperatures of 259 K to 269 K is shown. The images were extracted for two different frost periods in the first and second row. It is easy to see that icing is already a much slower process when the fin and tube temperatures are increased by 2 K from the reference case (263 K) to 265 K.

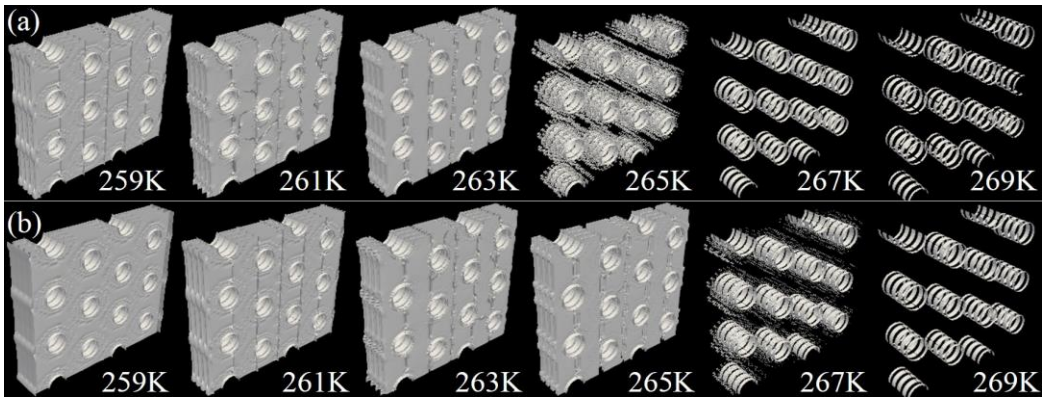

Figure 20: Accumulated frost mass for different fin and tube temperatures from 259 K (left) to 269 K (right). The following boundary conditions are defined on the air supply side: Temperature 275 K, relative humidity 90%, speed 2m/s. (a) Comparison to time 3000 s, (b) Comparison to time 5000 s.

The change in flow velocity also has an influence on the frost behaviour. This is illustrated in Fig. 21 by showing the frost coloured by the velocity for speeds of 0.5 m/s to 3 m/s for temperature boundary conditions similar to the reference case.

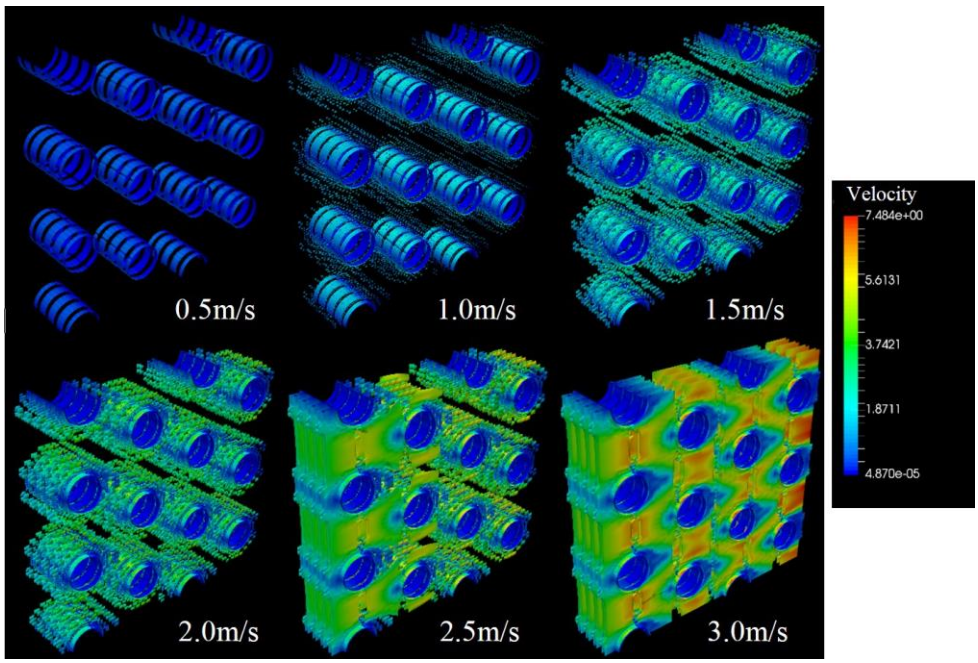

Figure 21: Accumulated frost mass for various air supply speeds from 0.5 m/s to 3 m/s. The following boundary conditions are defined on the air supply side: Temperature 275 K, relative humidity 90 %. The pipe and fin temperatures are fixed at 263 K. The frost zone is colour-coded by the velocity size. The time for all 6 figures is 1800 s.

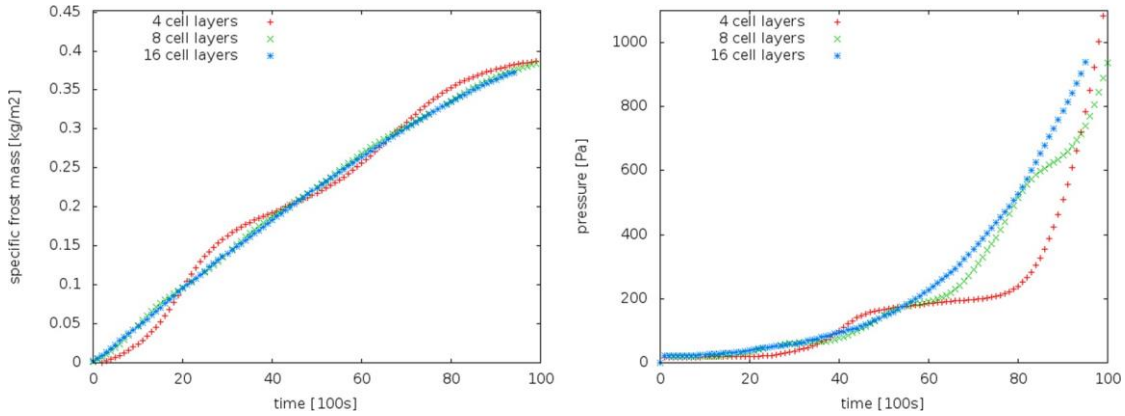

Figure 22: Accumulated frost mass (left) and corresponding pressure loss (right) for different numbers of cell layers between the fins for tube and fin temperature of 263 K, air supply side temperature of 275 K, air supply side relative humidity of 90% and an air supply side speed of 2 m/s.

To test the dependence of the results on the computational network, several cell layers were introduced between the lamellae. Fig. 22 compares the accumulated frost mass (left) and the static pressure (right) for these simulations using the boundary conditions of the reference case. It is shown that four cell layers are not sufficient to record a smooth icing and pressure curve. The observed oscillations may be related to the fact that each of the layers is subsequently filled with frost. The more cell layers there are, the more this process continues. With 16 cell layers no vibrations can be observed. Most symmetrical simulations were performed with 8 cell layers, so that (stepwise) oscillations still present in the following results can be attributed to this parameter and a smooth curve can be extracted with a curve that is coupled to the higher pressure values for a certain time.

Fig. 23 compares the accumulated frost mass and the associated pressure loss when - starting from the reference case - the temperature of pipes and fins is varied from 259 K to 279 K. A rapid increase in pressure drop is only present at low temperatures from 259 K to 265 K. At tube and fin temperatures of 259 K and 261 K a complete blockage of the heat exchanger can be achieved in about one to two hours real time. The gradient observed in the icing curve is linked to the fin and tube temperatures. Of course, frost is not observed at temperatures above 273 K. In this figure calculations for two different numbers of cell layers are compared. If 16 cell layers are used, the results are smooth and no stepwise behaviour (as with eight cell layers) can be observed. However, in this case the calculation times are doubled.

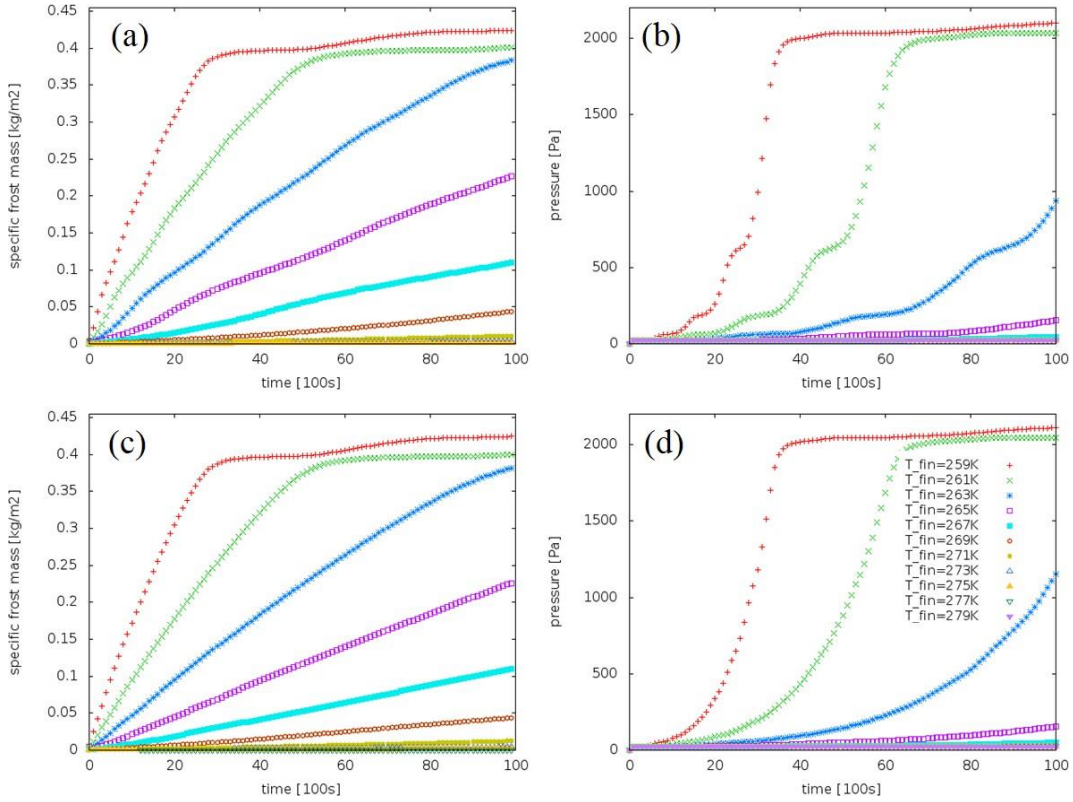

Figure 23: Accumulated frost mass (left) and corresponding pressure drop (right) for different fin and tube temperatures at a constant temperature of 275K, a constant relative humidity of 90% and a velocity of 2m/s on the air supply side; a,b: Results from simulations with 8 cell layers between fins; c,d: calculations with 16 cell layers between the fins.

The relationship between frost mass and pressure loss and the temperature on the air supply side is shown in Fig. 26. The temperature at pipes and fins has been set at 263 K and the relative humidity on the supply air side is 90% for all calculations. Increasing the temperature on the air supply side increases the amount of water available for the formation of frost on the fin and tubes, so that clogging of the heat exchanger is achieved much faster at higher temperatures on the air supply side.

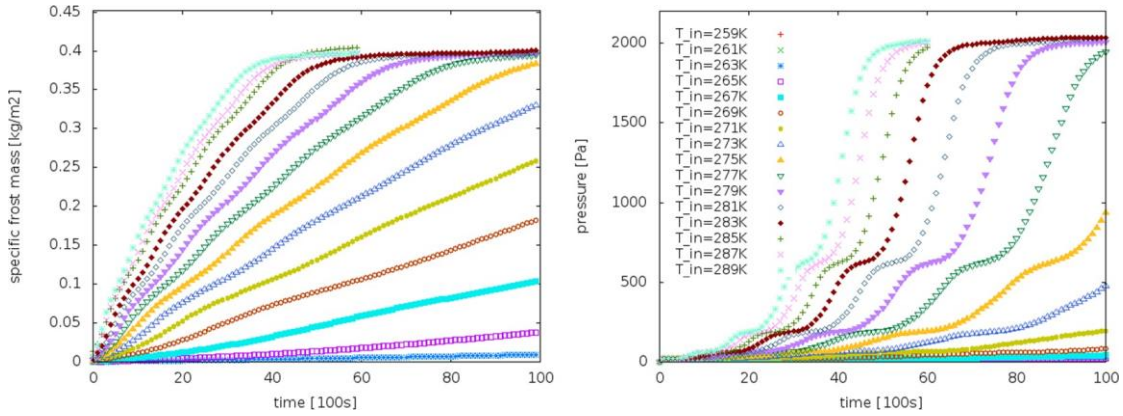

Figure 24: Accumulated frost mass (left) and corresponding pressure drop (right) for different temperatures on the air supply side at a constant relative humidity of 90% on the air supply side and a constant fin and tube temperature of 263 K. The velocity of the air supply side is fixed at 2 m/s.

Fig. 25 shows the relationship between frost mass and pressure loss when the relative

humidity on the air supply side changes from 10% to 100% at a constant temperature on the air supply side of 275 K - thus changing the absolute humidity (water content) there. The temperature on fins and tubes was kept constant at a value of 263 K as set in the reference case. A similar behaviour to the variation of the temperature on the air supply side (see Fig. 24) can be observed. However, the frost times at 100% humidity at 275 K shift by a factor of about two compared to a calculation at 90% humidity at 289 K according to the specified absolute water content.

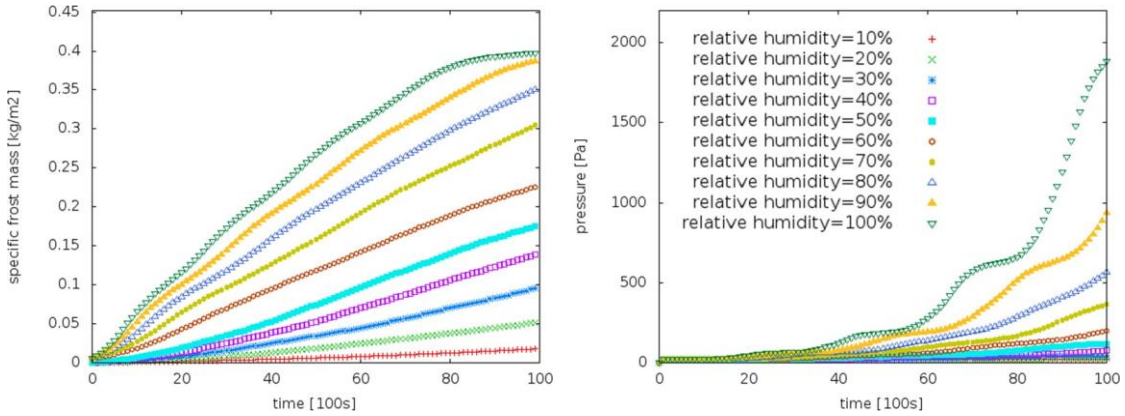

Figure 25: Accumulated frost mass (left) and corresponding pressure drop (right) for different relative humidities on the air supply side and constant fin and tube temperature of 263 K and a constant air supply side temperature of 275 K. The air supply side velocity is fixed at 2 m/s.

The frost mass and the associated pressure loss of the symmetrical model also depend on the mass flow through the heat exchanger. Simulations for different velocities on the air supply side in the range of 0.5 m/s to 3 m/s were performed. All other boundary conditions correspond to the reference case. A non-linear behaviour can be observed for both frost mass and pressure.

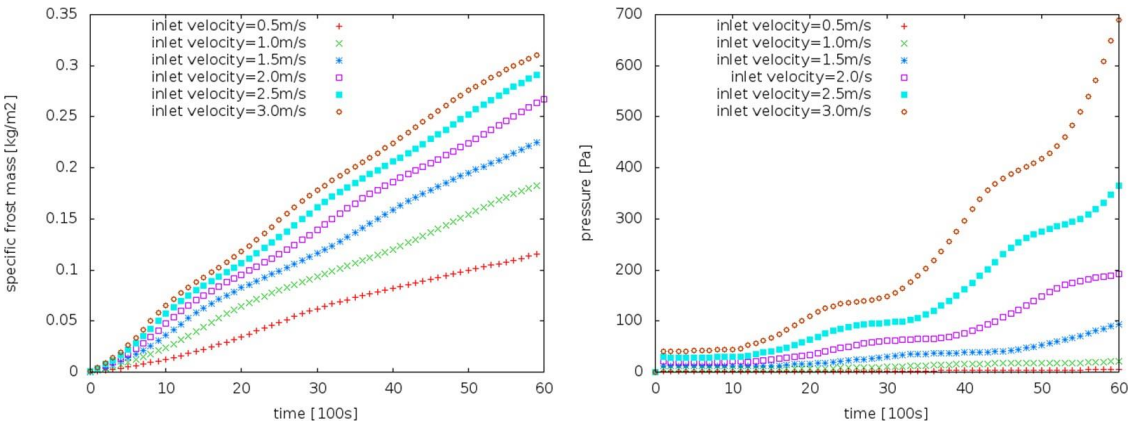

Figure 26: Accumulated frost mass (left) and corresponding pressure drop (right) for different velocities on the air supply side and a constant relative humidity of 90%, constant fin and tube temperature of 263 K and constant air supply temperature of 275 K.

The growth of the frost layer between the fins can be further analysed by plotting the frost volume fraction αf along lines perpendicular to the flow (see Fig. 27). The frost accumulations

start with small values of αf in fig. 27a and lead to an almost complete frost coverage in fig. 27c. Two curves are shown for each of the time steps. Lines drawn directly in front of the tubes (orange) show less frost coverage than lines in front of the gaps between the tubes (blue), where there is more cold heat exchanger area.

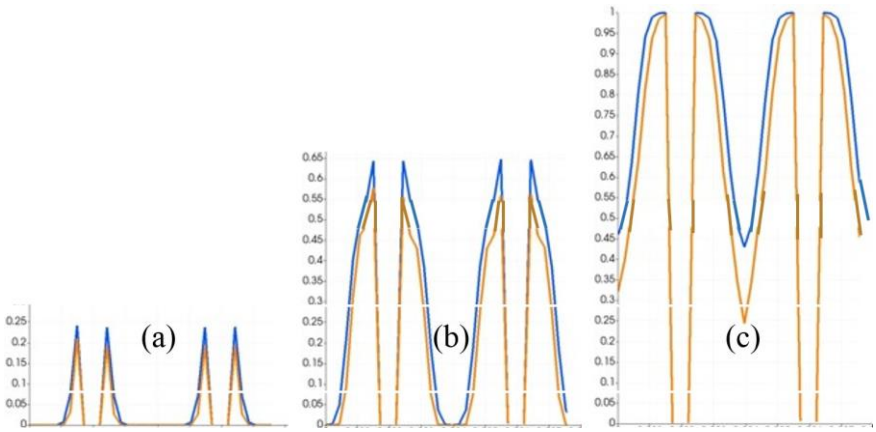

Figure 27: Accumulation of frost over time around the fins, which have two layers of lamellae. The y-axis shows the frost volume fraction αf.

The simulations with the overall heat exchanger models followed a two-stage approach. In the first step a Laplace calculation was performed to solve the heat conduction equation for the distribution (diffusion) of the tube temperatures on the fin surfaces. Then the temperatures at fins and tubes were determined and the Navier-Stokes solver was started with the above presented icing code (and used for the symmetric simulations). For the simulations, temperature and relative humidity on the exhaust side were set to 275 K and 90 % according to the experiments. The velocity was set to 2 m/s.

Below the icing for the simulations with temperature distribution configuration A on the tubes is shown, which corresponds to the test setup with an evaporating refrigerant. Clearly visible are frost-free areas, which refer to tubes that contain almost completely gaseous refrigerant at elevated temperatures slightly below 273 K. However, the heat exchanger is to a large extent completely covered with frost. This is not the case if a temperature profile is used on the tubes according to configuration B. In this case, a linear temperature distribution between 263 K and 273 K on the tubes (and thus on the fins) allows complete heat exchanger coverage only at selected points. This can also be seen in Fig. 28, where the frost mass is coloured according to static pressure for longer frost periods. Since different pulse boundary conditions exist, the pressure for these cases is shifted over a range of about 31 Pa for configuration A compared to 182 Pa for configuration B. The frost accumulation is much more homogeneous for configuration A than the linear temperature distribution of configuration B, which has an almost complete blockage in the upper part, resulting in high local pressure values. This part is enlarged in Fig. 29. Here the accumulated frost mass is coloured according to the temperature (Fig. 29 left) and velocity (Fig. 29 right). The local

blockage there leads to low flow velocities. The frost mass on one disk of the heat exchanger is shown in Fig. 10 left to further illustrate the strong influence of the linear temperature boundary condition of configuration B.

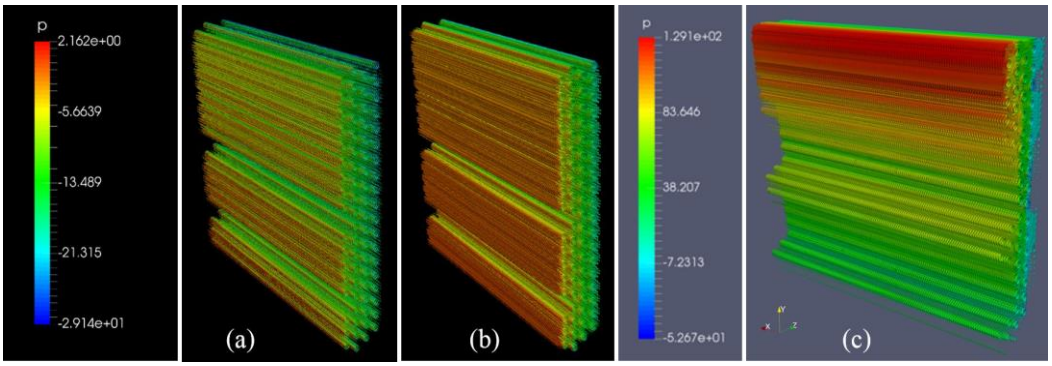

Figure 28: Frost mass coloured with the static pressure during subsequent icing of the heat exchanger for configuration A (a, b) and configuration B (c)

The influence of frost formation on the local flow velocities is also shown several times on a vertical section plane for a fin temperature distribution according to configuration B in Fig. 30. The flow becomes more and more uneven as frost accumulates around the pipes (see the magnifying inserts Fig. 30a* to Fig. 30d*). These velocity inhomogeneities can also be observed all the way upstream to the exhaust side. This behaviour can also be seen for the fin and temperature setting configuration A, where high velocities can be observed in the lower part of the exhaust side.

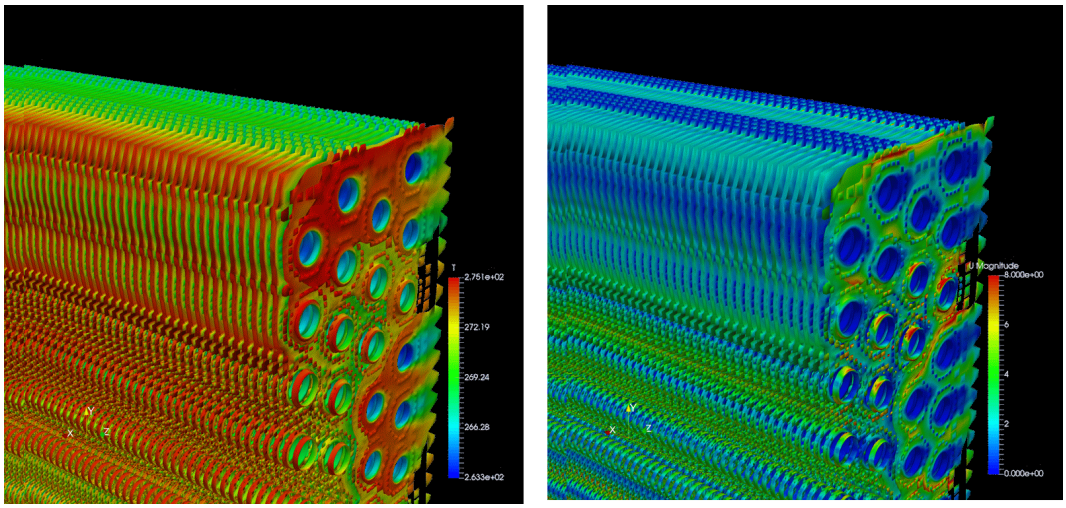

Figure 29: (left) Accumulated frost mass, colored with the temperature for configuration B; (right) Accumulated frost mass, colored with the amount of velocity for configuration B.

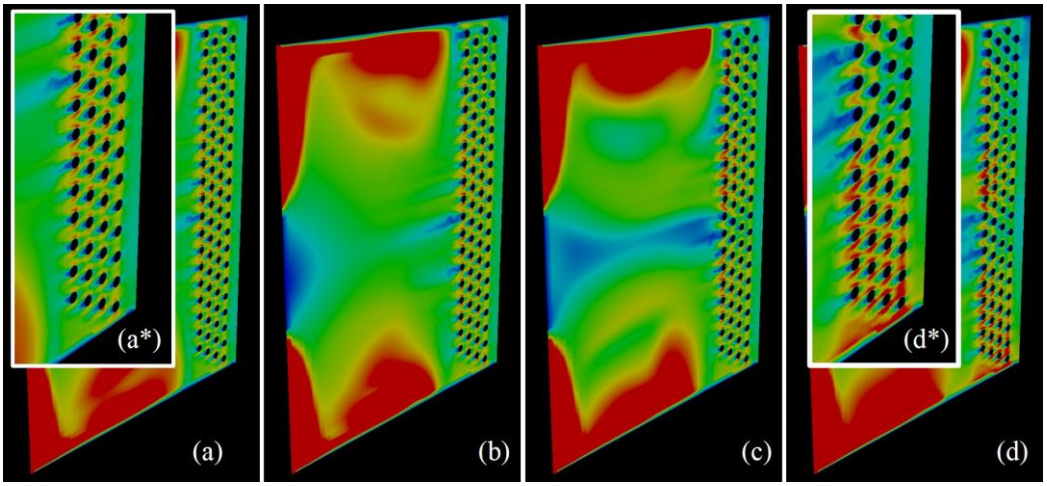

Figure 30: Amount of velocity (colour range 0.6 m/s) for a vertical section through the heat exchanger for the temperature profile configuration B for different times during the subsequent icing of the heat exchanger For figures (a) and (d) an enlarged view is included as inserts (a*) and (d*).

The calculations on the overall heat exchanger model were performed with the different fin and tube temperature configurations A and B and different impulse boundary conditions on the air supply side. Figure 31 shows that the frost mass accumulation at the same mass flow for configuration B is much slower compared to configuration A. The introduction of a swirl boundary condition on the air supply side has no influence on the frost curve, since the flow velocities at the location of the heat exchanger are comparable and small local differences do not play a significant role in the icing of the fins. A change in the mass flow on the supply air side can be observed according to the symmetrical parameter studies.

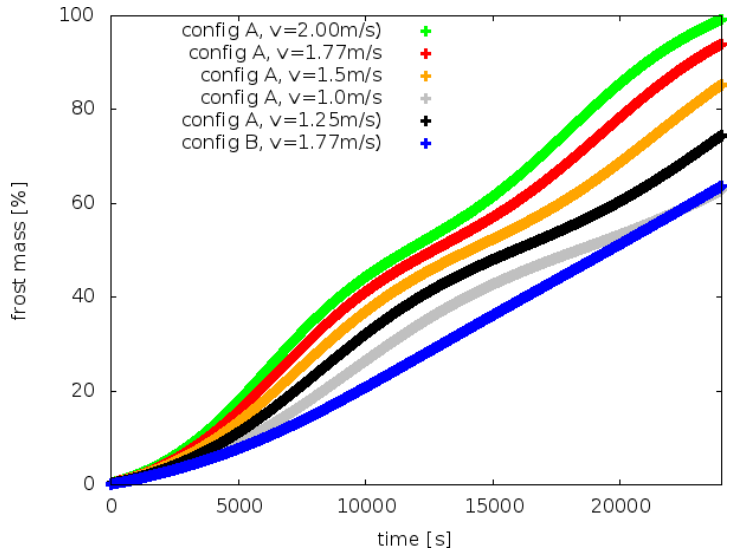

Figure 31: Comparison of the accumulated frost mass for the overall heat exchanger model for different tube/fin temperature and velocity boundary conditions.

Furthermore, the results of the symmetrical simulations for the different tube and fin temperatures can be used to calculate the frost mass and pressure loss for different tube and fin configurations. The frost mass can be calculated by adding the specific frost mass at a certain temperature and multiplying it by the range in which this temperature is observed.

The pressure is given by the average value over the different areas of the heat exchanger. Fig. 32 summarizes the results for fin and tube temperature configurations (configuration A and B), compared with a constant tube and fin temperature of 263 K, which gives the largest frost mass. The reconstruction is based on the results and is shown for 8 and 16 cell layers between the fins.

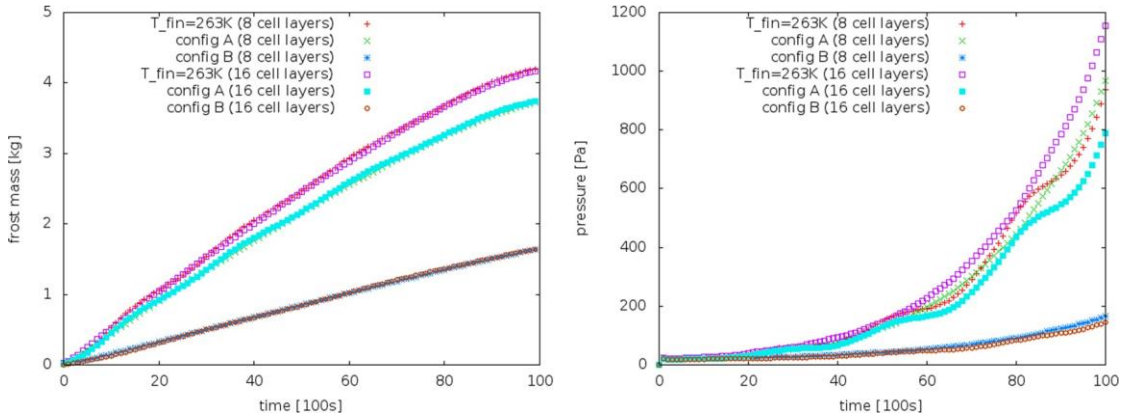

Figure 32: Accumulated frost mass over time (a) and corresponding pressure loss (b) for the reconstruction of a total heat exchanger based on the results of the symmetrical model. The results of the pipe and fin temperature configurations A and B and a constant of 263 K are compared. In this figure the results for two different cell layers between the fins are shown.

In this work package the frost growth on a heat exchanger in the SilentAirHP heat pump assembly was analysed with numerical approaches and compared with experimental results. Frost mass and frost layer thickness are available by using scale and image acquisition techniques. Using the experimental boundary conditions for an evaporating refrigerant, numerical simulations were performed on the entire heat exchanger assembly. Frost mass, increasing air flow velocities and pressure increase during subsequent freezing and blocking of the heat exchanger were additionally calculated for operation with a non-evaporating refrigerant, which ensures a linear temperature distribution along the refrigerant tubes.

A small symmetrical section of the heat exchanger was numerically analyzed by performing parametric studies for different fin and tube temperatures and changing temperature and relative humidity on the air supply side of the heat exchanger. In addition, simulations with different mass flows through the heat exchanger were performed.

Experimental measurements are available by recording the mass of the accumulated frost. After about 3 hours, 2 kg of frost mass has accumulated in the experiment, with the gradient of accumulation changing after about 85 minutes. This two-step frost growth is not observed in the numerical approach and reconstruction, where a more homogeneous increase is observed, but the gradient also decreases with time, as observed in the experiment. The reconstruction of the frost growth from the data of the symmetric simulations overestimates the experimental weight measurements by about 30 %, if focusing on the first growth gradient. However, it should be noted that even small temperature changes to higher values

lead to a rapid decrease of frost mass in the simulations.

Furthermore, the cumulative frost layer observed in the experiment can be compared with the numerical data. Sharp structures are observed in the initial frost state and are smoothed more and more during subsequent frost formation of the area between the fins.

The ability to predict the heat exchanger performance including icing without multi-core overall simulation models is crucial for the introduction of these icing models into the development chain of heat pump heat exchangers, because if the geometry of the heat exchanger (e.g. distance, depth and curvature of the fins) changes, only the symmetric simulations for a given set of boundary conditions have to be performed.

3.2 Experimental Method Development

Construction of the acoustic measuring dome

The design of the acoustic measurement dome (Fig. 33a) was altered during the detailed planning (Fig. 33b) in order to be able to react more flexibly to different heat pump geometries. The new concept includes a maximum of six movable stands, which can be connected to each other at their topmost point in a star arrangement. The distance to the center is variable. The microphones are mounted on height-adjustable horizontal brackets. The arms can also rotate around the centre of the stand. This design allows any point in the room to be reached. Fig. 33c shows the acoustic measurement grid / dome during initial tests on a heat pump.

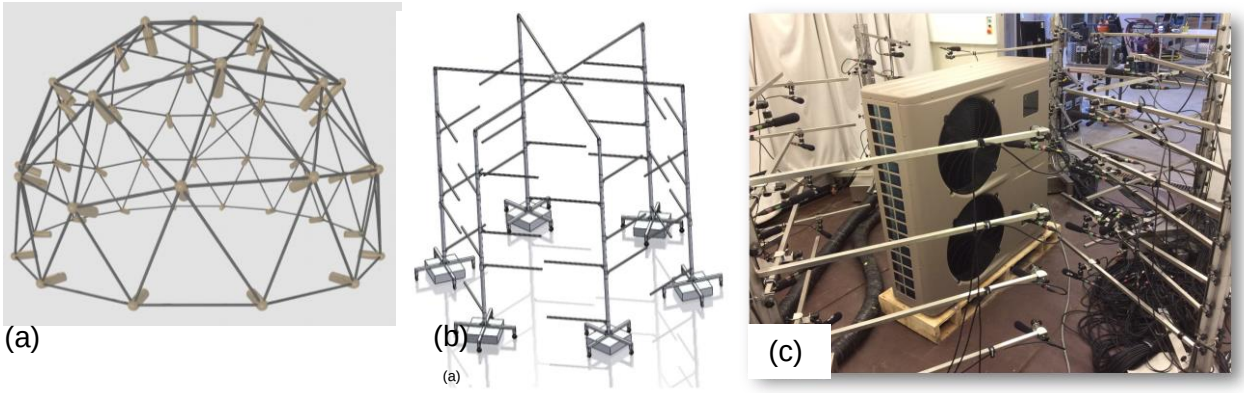

Figure 33: Acoustic measurement grid / dome. (a) Concept according to application, (b) improved concept, (c) first measurements with the built up acoustic measuring grid / dome on an industrial heat pump prototype.

Within the scope of this task, the data acquisition system was also designed, implemented and successfully tested. A multi-channel data recording system was used, which allows the simultaneous recording of 64 microphones. On the software side, a scriptable recording environment was selected and integrated with Reaper. Both the calibration of the microphones and the actual measurement can be remotely controlled from the climatic chambers via tablets.

Structure of the active noise cancelling module

Active Noise Cancelling (ANC) is an effective method of reducing the acoustic emissions of e.g. air-to-water heat pumps and changing their character. The method has well-known applications in modern headphones as well as in the automotive and aircraft industries. Due to the availability of fast signal processors, the method known since 1930 can now be successfully implemented.

An unwanted sound source is recorded with a microphone and analyzed in real time by a processor. In the simplest case, a single phase-inverted signal is generated and output via a speaker. This mixes with the original signal. Destructive interferences lead to a significant reduction of the original signal. In the real application these interferences are not perfect and a partial cancellation can be achieved, which also depends on the position of the sound receiver. For the applicability of this method in the field of heat pumps, installation, adaptation and optimal coupling to the structure play a major role. Initially, a rectangular duct (see Fig. 34 left) equipped with a fan, microphone and loudspeaker was used. Then the method was applied to a 300mm pipe (see figure 9 right). The achievable sound reduction of the right-hand corner channel is about 7 dB (see Fig. 35 left). The noise reduction is mainly achieved by reducing the primary frequency contributions (see Fig. 35 right). [14] [15]

Figure 34: (left) ANC rectangular duct in a 16 channel microphone semicircle to determine the spatially resolved sound reduction; (right) 300 mm circular version

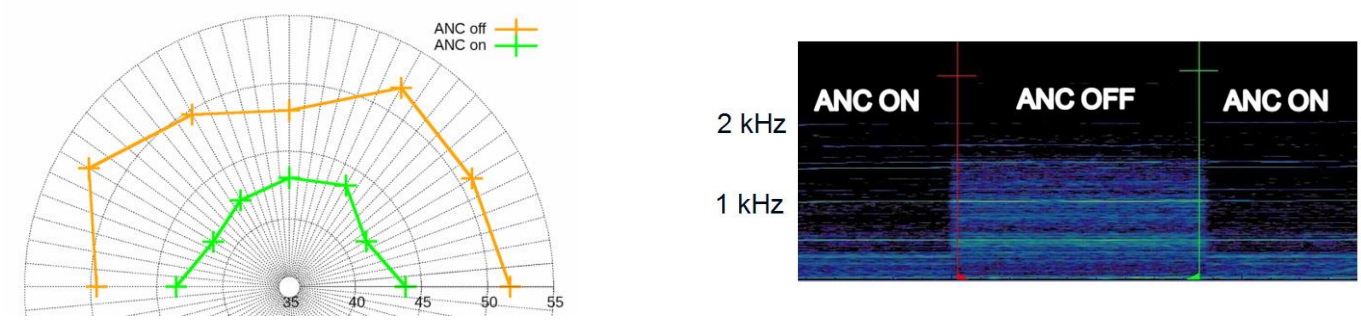

Figure 35: (left) Sound reduction potential of the rectangular channel. The radius represents the measured sound level; (right) Activating the counter sound (ANC on) leads to the suppression of certain frequencies. Tonal components are nevertheless retained in comparison to the original signal (ANC off).

Figure 36 shows a setup with five-fold symmetry: the 400 mm diameter pipe is divided into five equal areas to achieve an optimal one-dimensional sound character for active noise cancelling. Final analysis Fig. 37 shows the resulting frequency spectra in the individual pipe sectors, each with the ANC system deactivated and activated. It was shown that it is possible to split a sound source into five channels and reduce the sound events with only one reference microphone using ANC. The best conditions for ANC are given with small sound sources, a high volume of the source, soft damping material, low flow velocity and low flow turbulence. In summary, it can be stated that one-dimensional sound fields can be well combated with "anti-noise", the more three-dimensional the arrangement of the sound fields becomes, the more difficult counter-noise measures become. Counter-noise as a measure does not seem to be suitable for an application in the area of the fan blow-out at present.

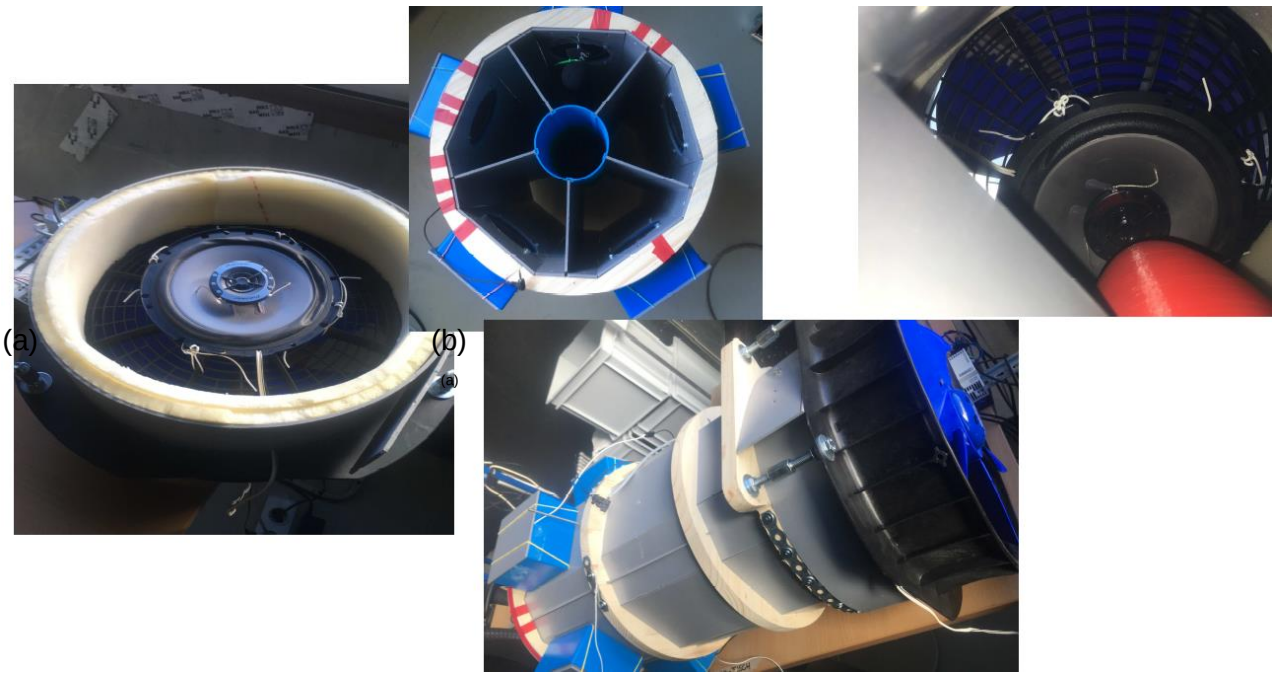

Figure 36: Division of a pipe with 400 mm diameter into five equal symmetrical parts to reduce the three-dimensionality of the sound field.

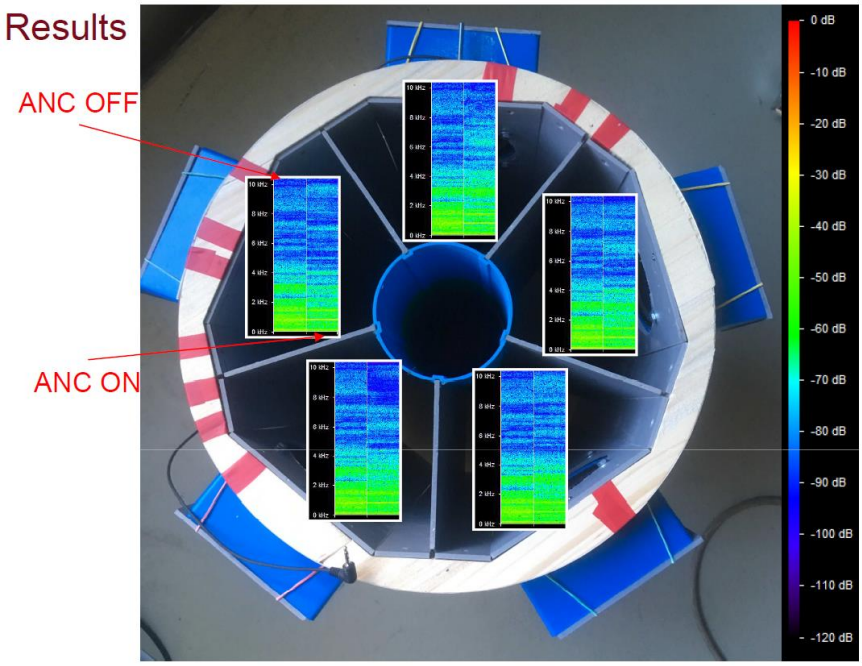

Figure 37: Resulting frequency spectra in the subdivided tube geometry each with ANC system deactivated and activated.

Structure of the measuring channel

In the course of the project it has been shown that it is useful to characterize some components by means of a half-space measurement. [16] [17]

Measurements were carried out both without flow (see Fig. 38 left and 39) and in suction and pressure flow (see Fig. 38 right).

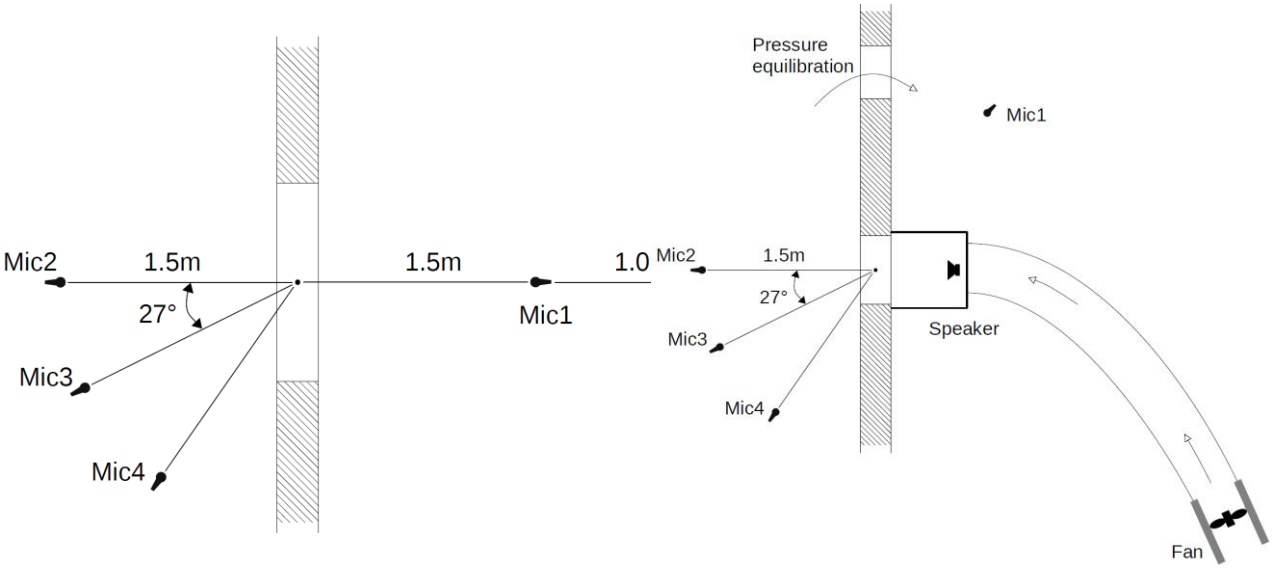

Figure 38: (left) Schematics of the measurement setup for measuring the transmission behaviour of heat exchanger and sound insulation materials without flow. (right) Setup for measurements in a sucking or pressing flow field.

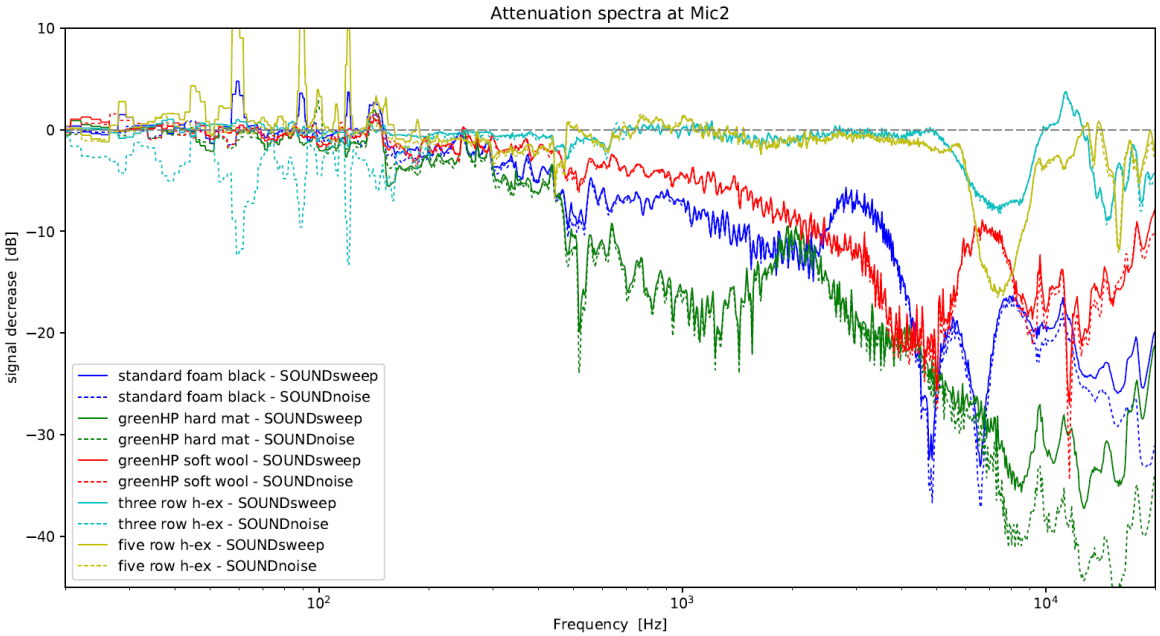

Figure 39: Spectral analysis of the data of microphone 2 displayed as a difference to the respective signal without heat exchanger or insulating material

Figure 40: Test setup for measurements of the transmission properties of heat exchanger and insulating materials in sucking and pressing flow (schematic diagram see Figure 38 right).

Connection of the pressure measuring sensors

Originally, it was intended to measure the sound pressure on the inner sides of the flowed-through area. During the initial work in the project and after discussions in the community, great importance is also attached to measuring the vibrations of the devices. The sound

velocity at the surfaces is related to the sound pressure and is measured by vibration sensors. For this reason, vibration sensors were used instead of wall pressure sensors, thus making structure-dependent sound velocity accessible. A simultaneous measurement of vibration (sound velocity), sound pressure (using microphones) and flow velocity (using CTA hot-wire anemometer) was realized and evaluated. The correlation of these three quantities provides meaningful information about the interrelationships of the sound production and propagation mechanisms involved. [16] [17]

This method was successfully tested with an indoor heat pump and two different heat pumps in the climatic chamber (see Figure 41 - 44). With the developed system it is possible to evaluate structural changes to the heat pump (combined statement of temporal mean values, investigation of signal contributions using cross-correlation, analysis of transient events). In addition, the basis for (remote) Machine Health Monitoring has been laid (flow and acoustic examination of the outdoor unit, fingerprinting of operating states, detection/monitoring of transient events).

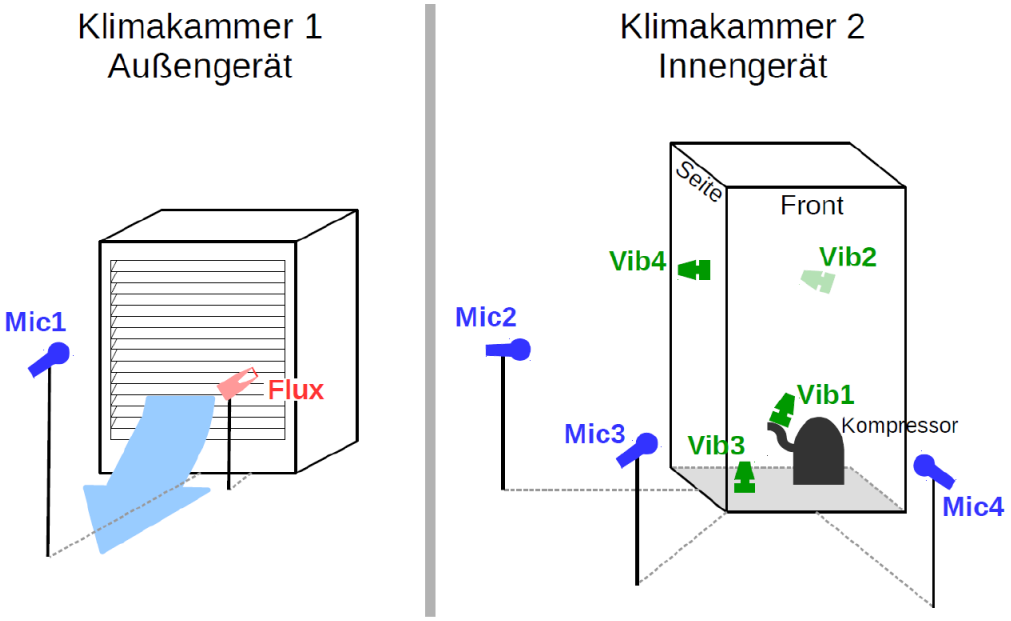

Figure 41: Positioning of sensors for the outdoor unit and indoor unit in the double climate chamber of the AIT. The sensors for flow, sound and vibration, measured simultaneously, are shown.

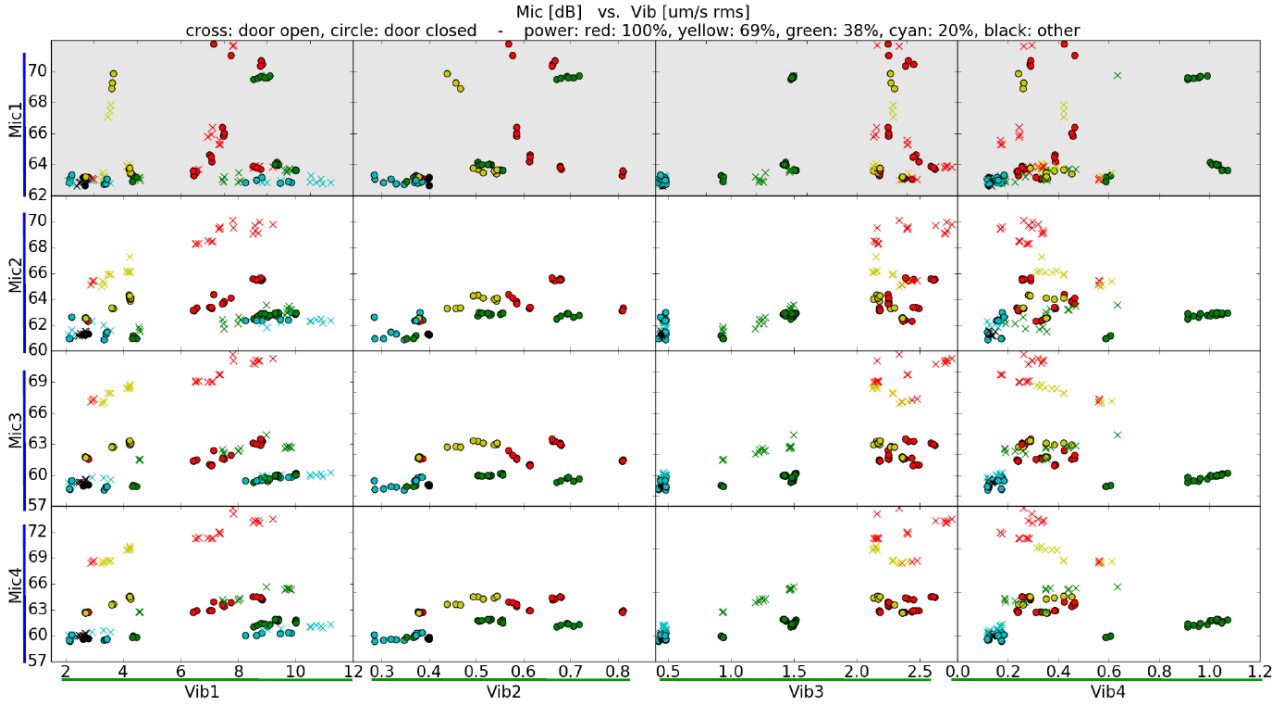

Figure 42: Correlation of time averages of microphone and vibration signals for different heat pump settings.

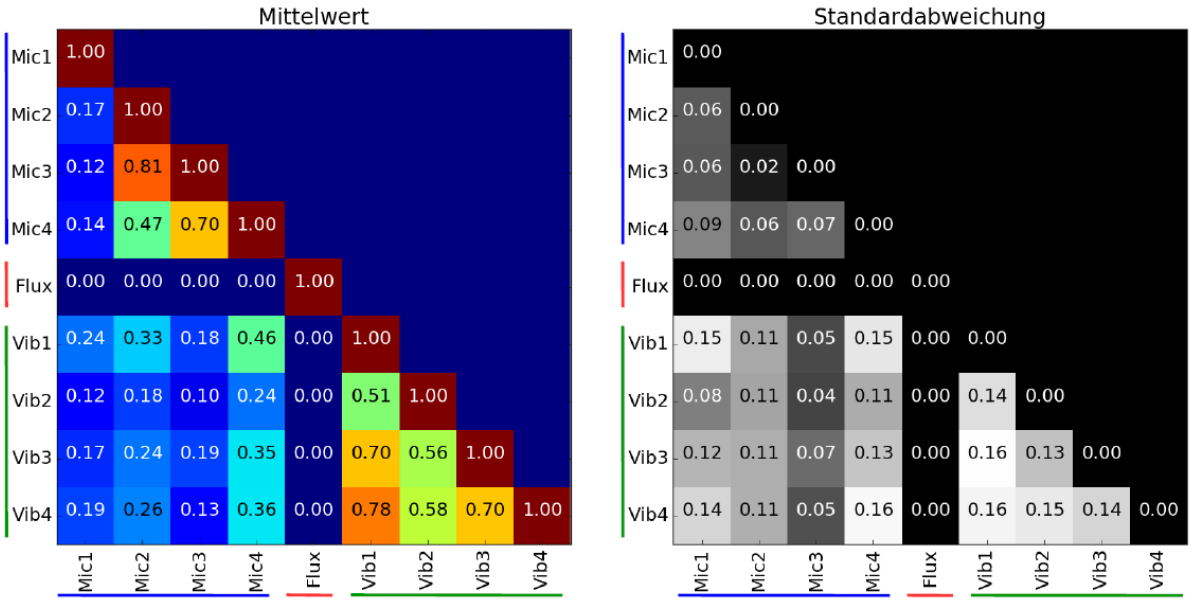

Figure 43: Cross-correlation of time series for a closed heat pump front and 38% of capacity.

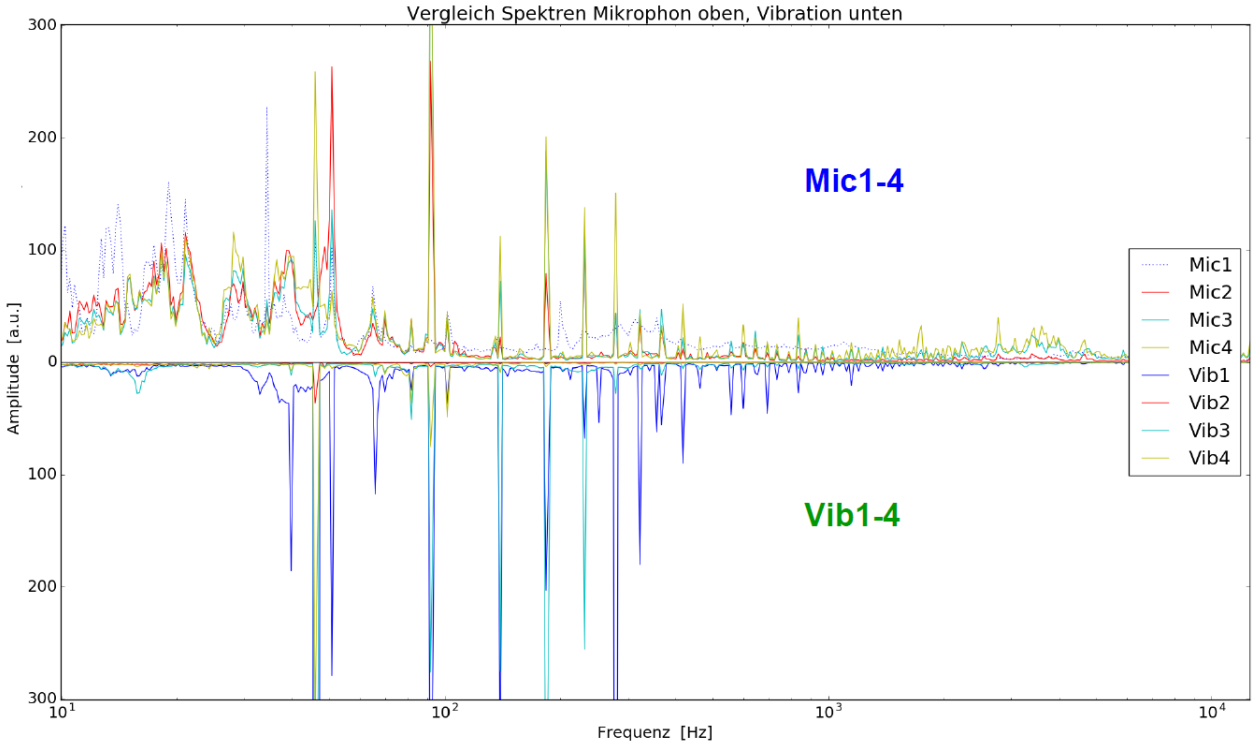

Figure 44: Comparison of microphone and vibration signals. There are clear similarities that illustrate a correlation of vibration and acoustics at selected frequencies.

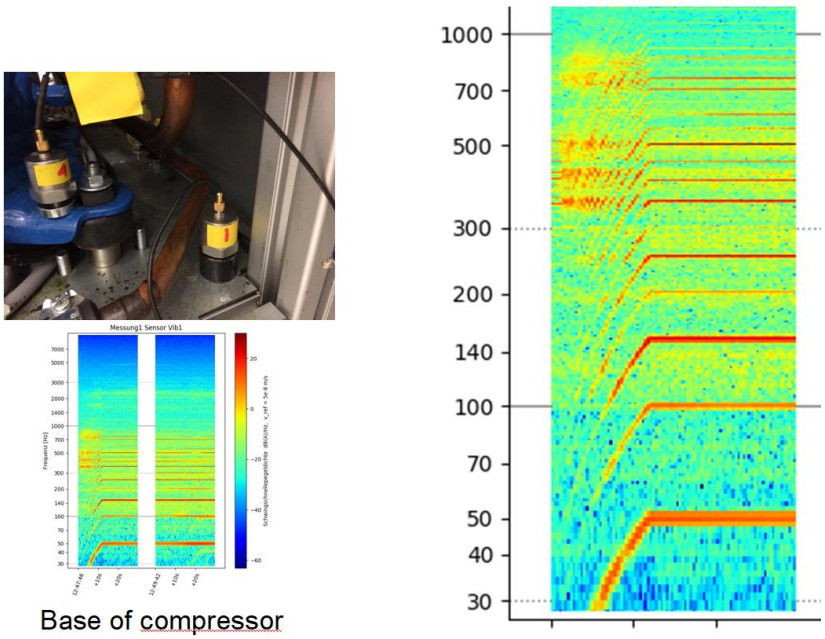

Figure 45: Compressor start-up in the time frequency course of a vibration sensor mounted on the base of the compressor. The temporal change of the frequency behaviour during the start-up is clearly visible. The x-axis shows the time, the y-axis the different frequencies.

3.3 Test setup of the air-water heat pump

Development of the experimental air-water heat pump

The SilentAirHP consists of two parts that are installed one above the other (Figure 46). The upper part consists mainly of the fan and evaporator, while the lower part contains the

remaining components. The fact that the two parts can be separated from each other means that the SilentAirHP can be operated both as a compact unit and as a split unit.

Figure 46: CAD drawings of the SilentAirHP.

A system sketch is shown in Figure 47.

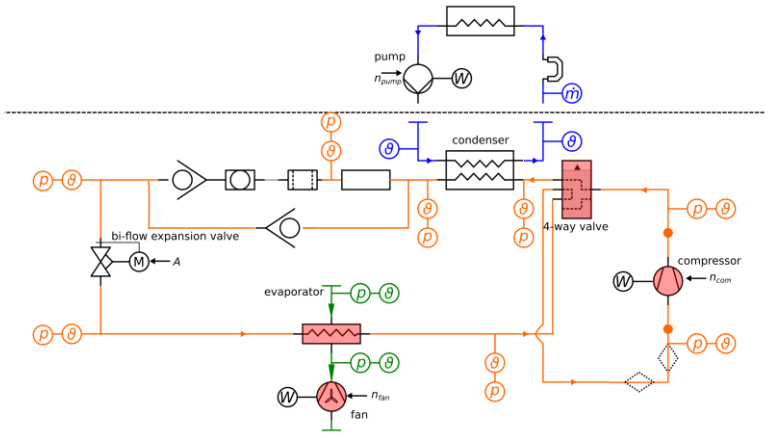

Figure 47: System sketch and measurement scheme of the SilentAirHP. Everything below the dotted line is built into the actual SilentAirHP. The heat extraction and the associated sensors above the dotted line belong to the AIT climate chamber. The sound-critical components are coloured red.

Design of the air-water heat pump

The experimental air/water heat pump was set up (see Figure 48) and successfully tested. Work was carried out to adapt the SilentAirHP to some further noise reduction measures.

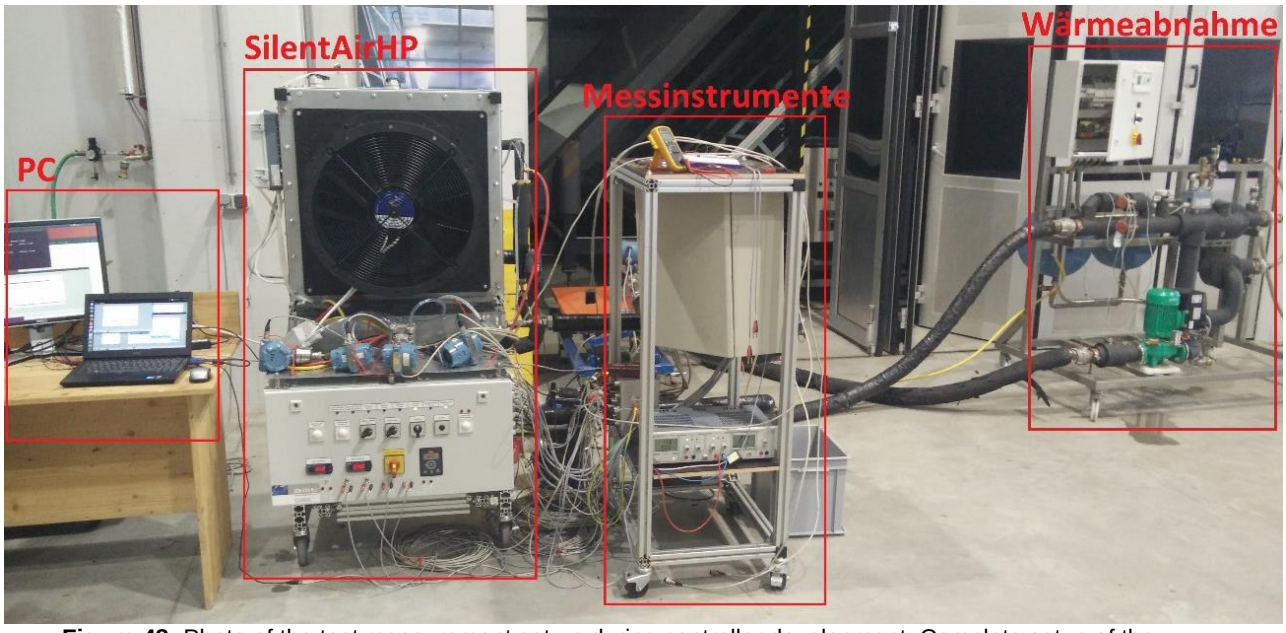

Figure 48: Photo of the test measurement set up during controller development. Complete setup of the SilentAirHP incl. PC, measuring instruments and heat dissipation

Development of noise reduction models

Different noise reduction modules/measures were created at the same time as the CAD planning [16] to ensure compatibility at a later date. As an example, Fig. 49 shows a retrofittable noise reduction measure with a splitter attenuator.

The following modules were designed in total:

- Airborne sound insulation of the compressor
- Insulation of the compressor against structure-borne noise
- Encapsulation of the compressor
- Sound absorption in a straight air duct
- Sound absorption in the deflection air duct
- Splitter silencer in straight air duct
- Splitter silencer in the recirculation air duct
- Diffusor for fan
- Fan blade optimization of the fan

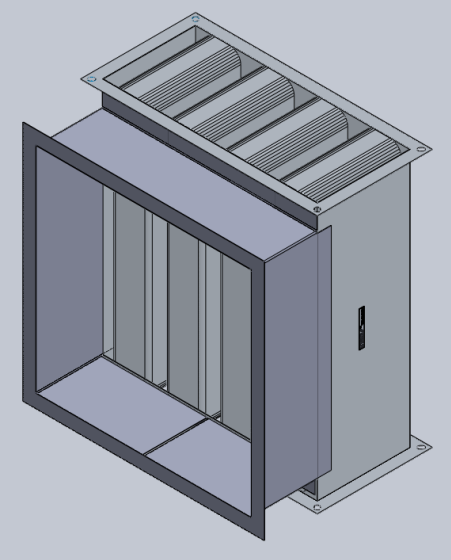

Figure 49: Combination silencer for retrofitting an air heat pump. The influence of the additional pressure loss is investigated both experimentally and with simulations.

Construction of noise reduction models

The noise reduction modules have been assembled and are ready for use. [16]

Optimization of the control for noise emissions

The original control of the SilentAirHP was optimized for sound emissions and adaptations regarding sound target values were implemented. This is also discussed above in the section "Development of control strategies".

3.4 Measurements

Investigation of the effects of noise reduction measures and component changes

The test phase was successfully completed. The most important results are summarized in Table 3. A diploma thesis is available for further study. [18]

Table 3: Evaluation catalogue based on the "Guide to the acoustics of air-to-water heat pumps" of the "Heat Pump Austria Association". [19] Results refer to the respective component of SilentAirHP under review.

Action		Effect Mechanism	Influence on the Sound Power Level
Constructional measures on the A/W-WP			
1	Encapsulation of the compressor	particularly effective when installed outdoors	Uncapsulated compressor not available
2	Structure-borne noise insulation of the compressor		Has not been examined
2a	Airborne sound insulation of the compressor	Attachment of an acoustic compressor hood	Reduction: <1 dB (A)
3	Structure-borne noise insulation of the fan	Less structure-borne noise transmission to the housing and channels	Has not been examined

4	Improvement of the flow near the fan	Diffusor	Reduction: 2 dB (A)
4	Sound absorbing duct insulation	Insulation material	Reduction: <4 dB (A) at maximum fan speed
6	Square duct deflections with additional lining	Use the deflection as a reflection silencer. Pay attention to the large channel width and prefer radiation upwards	Reduction: 2 dB (A)
7a	Absorption silencer	Deflection splitter silencer	Reduction: 2.5 dB (A)[1]
7b	Absorption silencer	Deflection	Reduction: 2.5 dB (A)[2]
8	Avoidance of channel resonances	Matching the length and cross section of the channels	Has not been examined
9	Baffle plates in bends	Less turbulence and less pressure loss	Has not been examined
Component-specific measures			
10	Low noise compressor	Noise reduction at the source	The compressor was not replaced
11	Low-noise fan type	Reduction of fan noise	Reduction: 8 dB (A)[3]
12	Clearing of the fan blades	Less structure-borne noise radiation through the wings	See 11
13	Optimization of the operating point of the fan	Reduction of fan noise through better flow conditions	See 4
14	Optimization of the evaporator	Reduction of pressure loss through the evaporator	Depending on the fan characteristic (eg 5 dB (A) if the pressure loss is halved)
15	Anti-ice coatings	Delay in ice build-up, change in defrost behavior of the heat exchanger	No change in sound power[4]
Control measures			
16	Optimization of the fan speed	With various circuits or with pre-resistors, a simple speed reduction is possible if required	Depending on the fan characteristic (eg: 5 dB (A) when reduced by 100 rpm)
17	Control optimization	Fewer on / off switching operations and shorter operating times at night, partial load operation during the night	With A2W35 and night reduction (12h): 10 dB (A), day 4.5 dB (A) more.[5]
18	Abtaustrategien	Changed ice formation behavior	"Defrosting noise level" < "operational level"
Active measures			
19	Active Noise Cancelling (ANC)	Active generation of counter sound	1-dimensional sound fields combated well with counter-sound (~ 7dBA reduction), 3-dimensional fields in the wake of the fan hardly influenceable

[1] FC050@594rpm,6.67V 60.25 dBA // Ref FC050@594rpm,6.67V 62.55 dBA
[2] FC050@594rpm,6.67V 60.15 dBA // Ref FC050@594rpm,6.67V 62.55 dBA
[3] ZN050@537rpm,4.79V 54.58 dBA // FC050@594rpm,6.67V 62.55 dBA // Data for the same volume flow
[4] 10% extension of the icing period
[5] With A2W35, partial load all day with 69 dB(A) or night: 58.8 dB(A) and day 73.5 dB(A)

Figure 50 shows the measurement setup. In addition to recording the thermodynamic variables of the climate chamber and the SilentAirHP, the microphone signals of the acoustic dome, the synchronous microphone and vibration signals and the transient weight signal were recorded. The measurements were performed for the different noise reduction measures. Figure 51 shows the results of a test measurement.

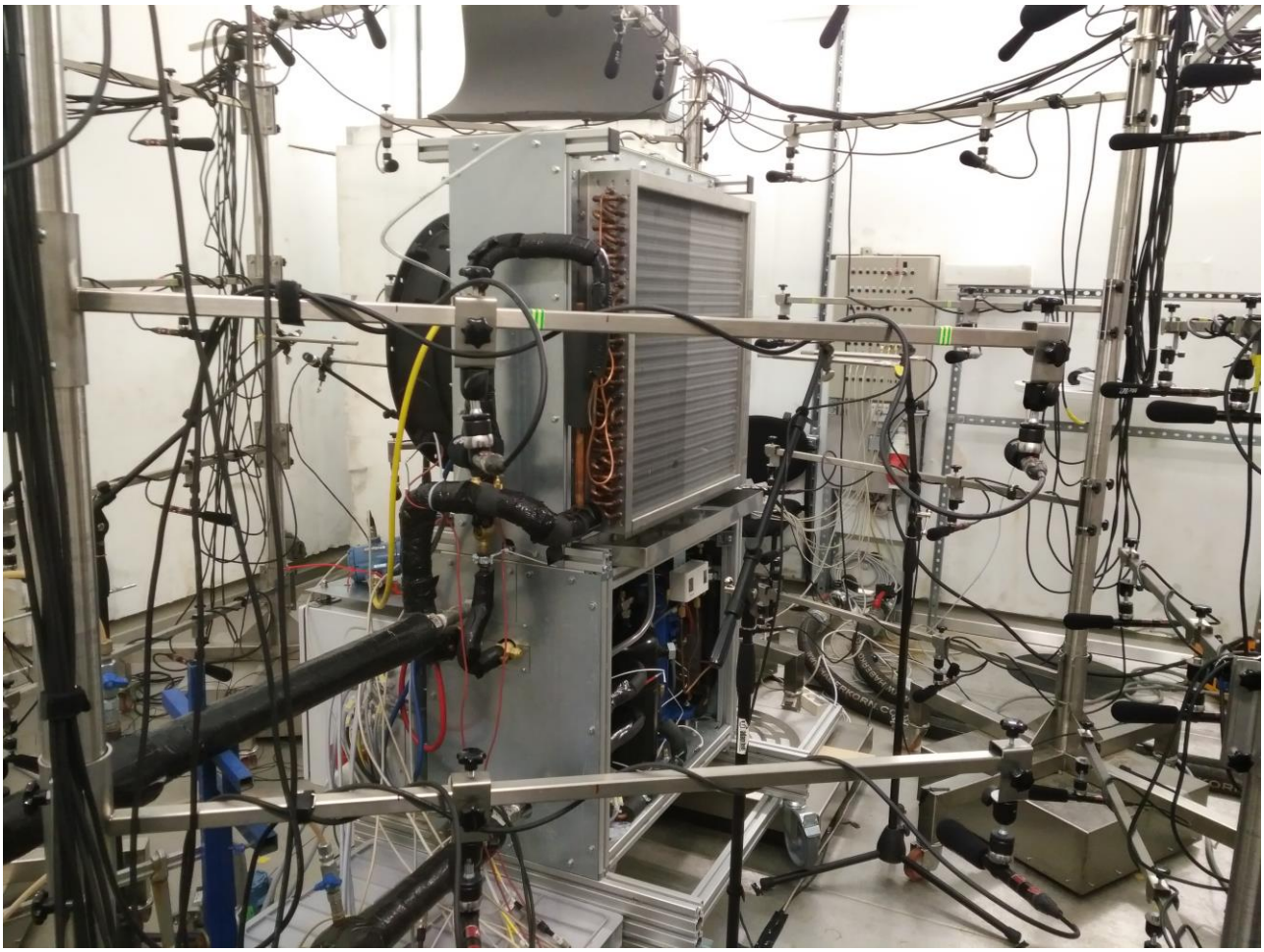

Figure 50: Measurement setup of the SilentAirHP in the climate chamber with 64 channel microphone dome, transient weight determination and synchronous measurement of acoustics and four vibration signals.

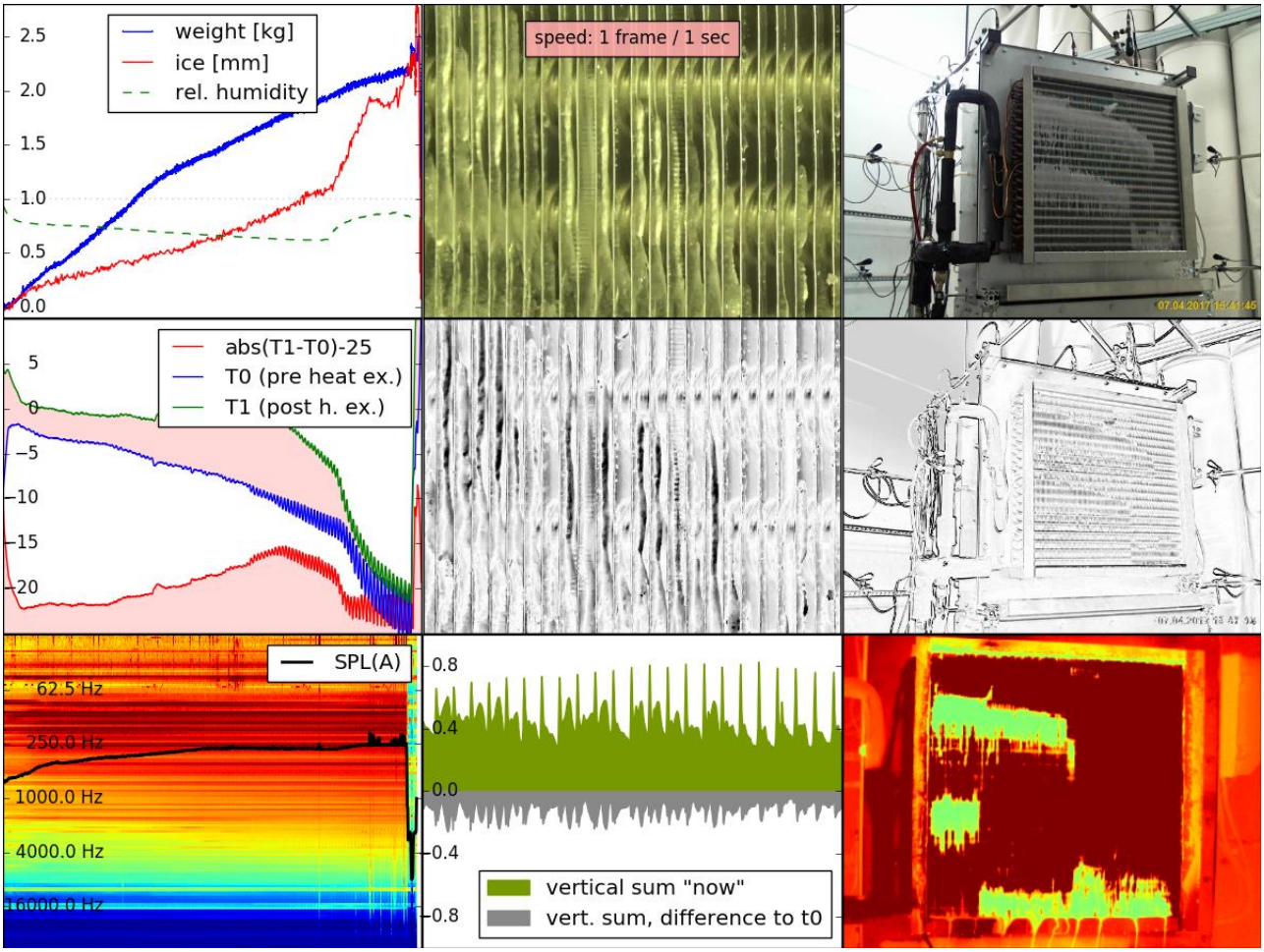

Figure 51: Overview of the temporal behaviour of a typical measurement of SilentAirHP with icing. From left to right: first row: weight and ice thickness, detailed view of fin, large view of SilentAirHP heat exchanger; second row: temperature in the outward and return flow of the refrigeration circuit, difference image of the fin detailed view, difference image of the overview image to illustrate the ice build-up; third row: temporal development of a representative microphone signal, brightness analysis of the ice at the fins to determine the ice thickness, thermographic image of the heat exchanger.

Within the framework of the measurements, background measurements were first carried out. This shows the influence of the necessary climate chamber technology.

Table 4: Background measurement with different settings of the climatic chamber technology. The fictitious sound power level of the switched-off heat pump at a temperature of 2°C and a relative humidity of 84% was calculated.

setting	water pump	humidity control	temperature control	heat pump	compressor	fan	SPL (dB(A))
1	off	off	off	off	off	off	35,7
2	off	off	off	on	off	off	50,9
5	off	off	on	off	off	off	53,7
4	off	on	on	off	off	off	53,6
3	on	on	on	off	off	off	53,7

Furthermore, the influence of the climatic chamber technology required for conditioning the climatic chamber on the measurement of the sound power level in a speed-dependent fan measurement was determined.

Table 5: A-weighted sound power level as a function of the control voltage of the fan; investigation of the influence of climate chamber technology.

ZN050, fan setting (volts)	SPL dB(A), 000 = water pump off, control of humidity and temperature off	SPL dB(A), 000 = water pump on, humidity and temperature control on
0	50,9	
1,79	50,7	56,1
2,68	50,8	56,1
3,57	51,4	56,4
4,46	53,3	57,0
5,36	56,8	58,9
6,20	60,6	61,6
7,14	64,5	65,0
8,04	67,8	68,1
8,93	70,6	70,7

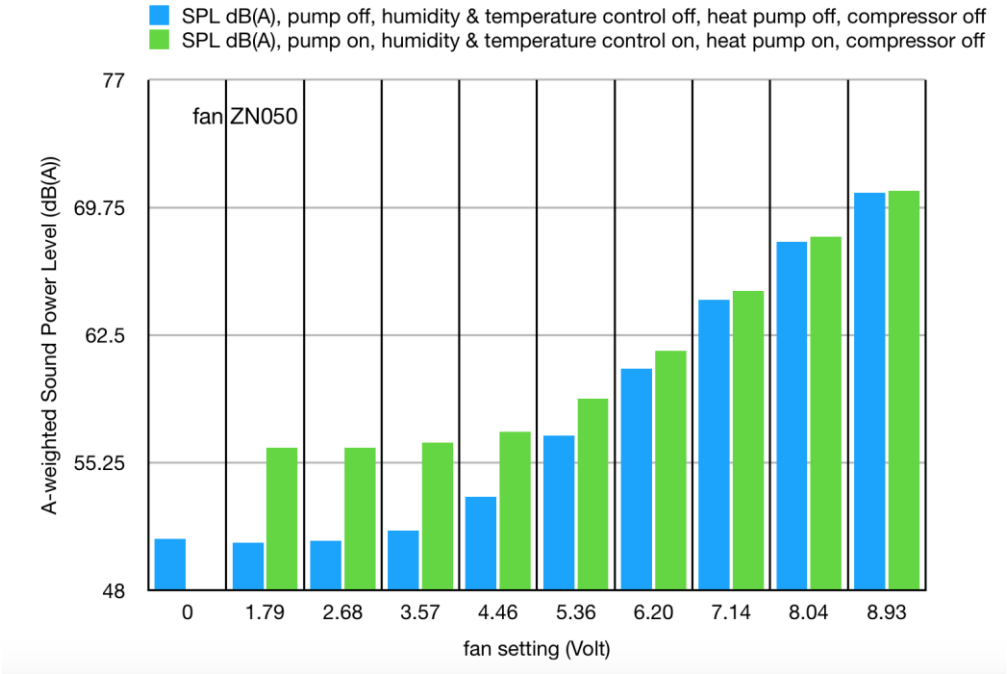

Figure 52: A-weighted sound power level as a function of the control voltage of the fan when investigating the influence of the climatic chamber technology. The two fans ZN050 and FC050 have different speed as a function of the control voltage. 10V control voltage corresponds to 1120 rpm for ZN050 and 890 rpm for FC050 fan.

Afterwards, fan speed dependent acoustic emissions were measured:

Table 6: A-weighted sound power level as a function of the control voltage of the fan

Fan-setting (volts)	SPL dB(A), ZN050	SPL dB(A), FC050, Baffle silencer	SPL dB(A), FC050	SPL dB(A), FC050, redirection
2,68	50,8		50,4	50,1
3,57	51,4			50,6
4,46	53,3	51,9	53,3	52,1
5,36	56,8	54,5	56,7	54,7
6,20	60,6	58,5	60,6	58,3
7,14	64,5	62,0	64,5	62,0
8,04	67,8	66,1	67,8	65,0
8,93	70,6	68,8	70,5	67,6
9,82		71,7	73,0	70,4

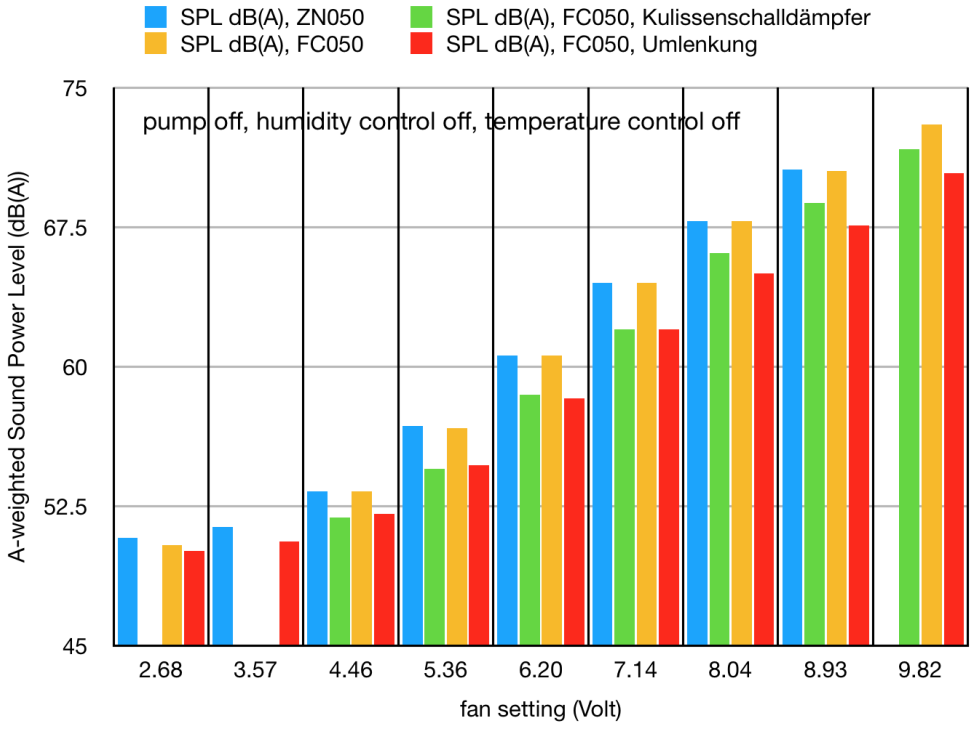

Figure 53: A-weighted sound power level as a function of the fan control voltage for different structural sound insulation measures and 2 different fans.

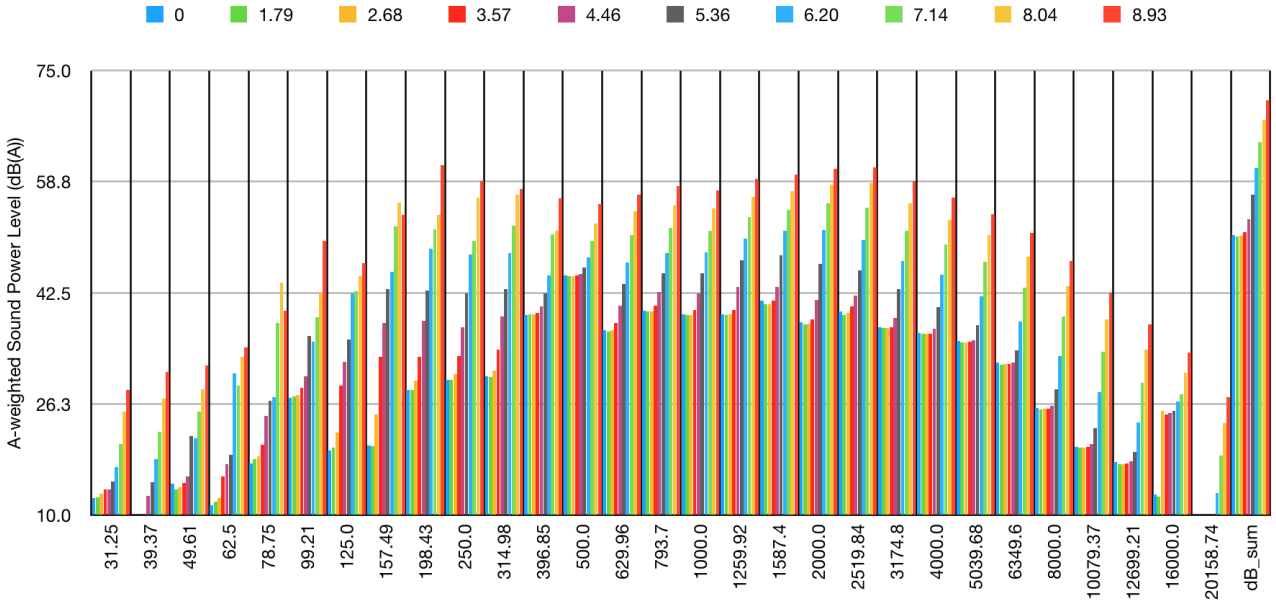

Figure 54: Spectral representation of the A-weighted sound power level as a function of the fan control voltage ZN050

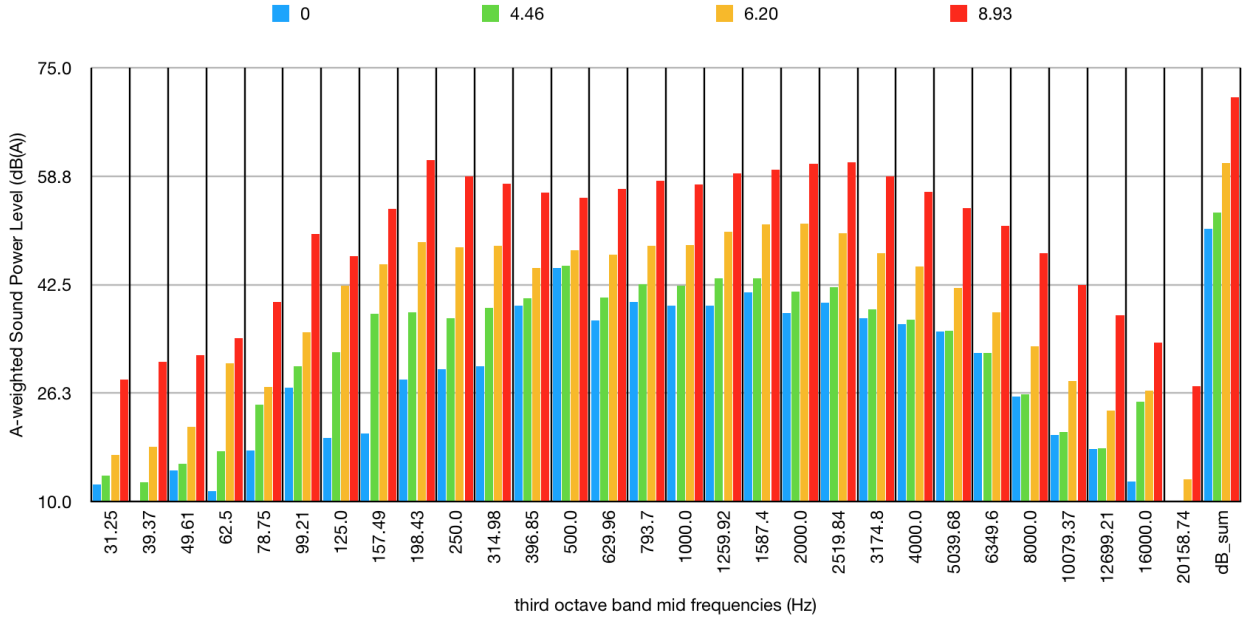

Figure 55: Detailed spectral representation of the A-weighted sound power level as a function of the fan control voltage ZN050

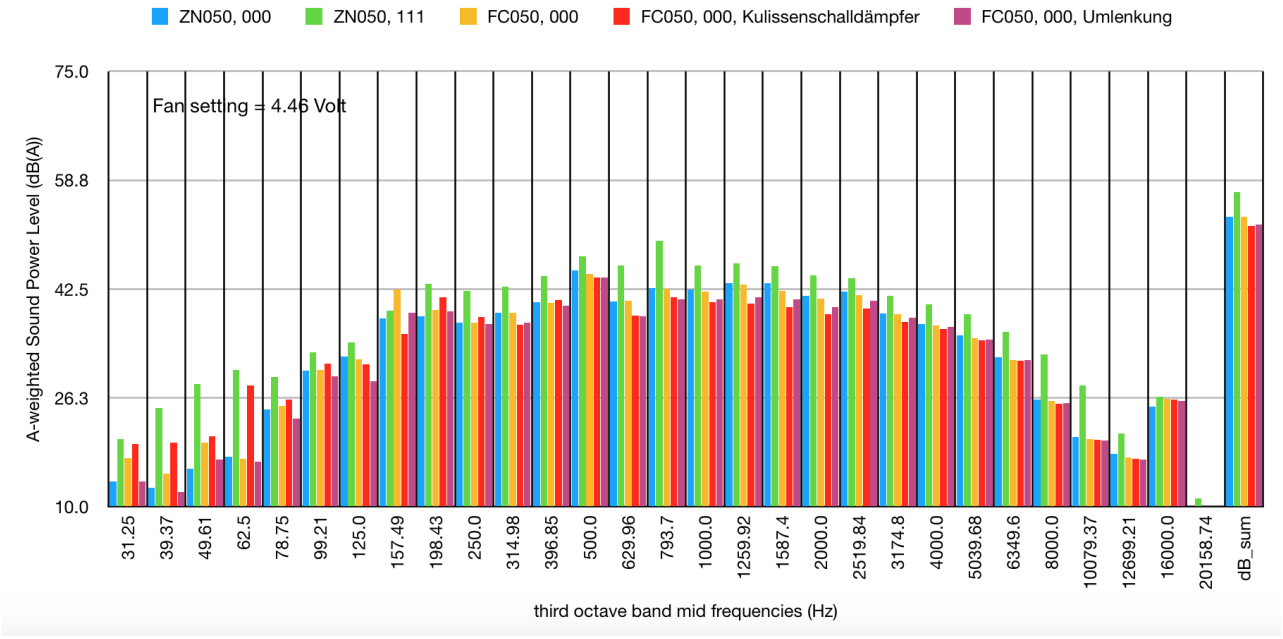

Figure 56: Spectral representation of the A-weighted sound power level for a fan control voltage of 6.20 Volt for 2 different fans and different sound insulation measures

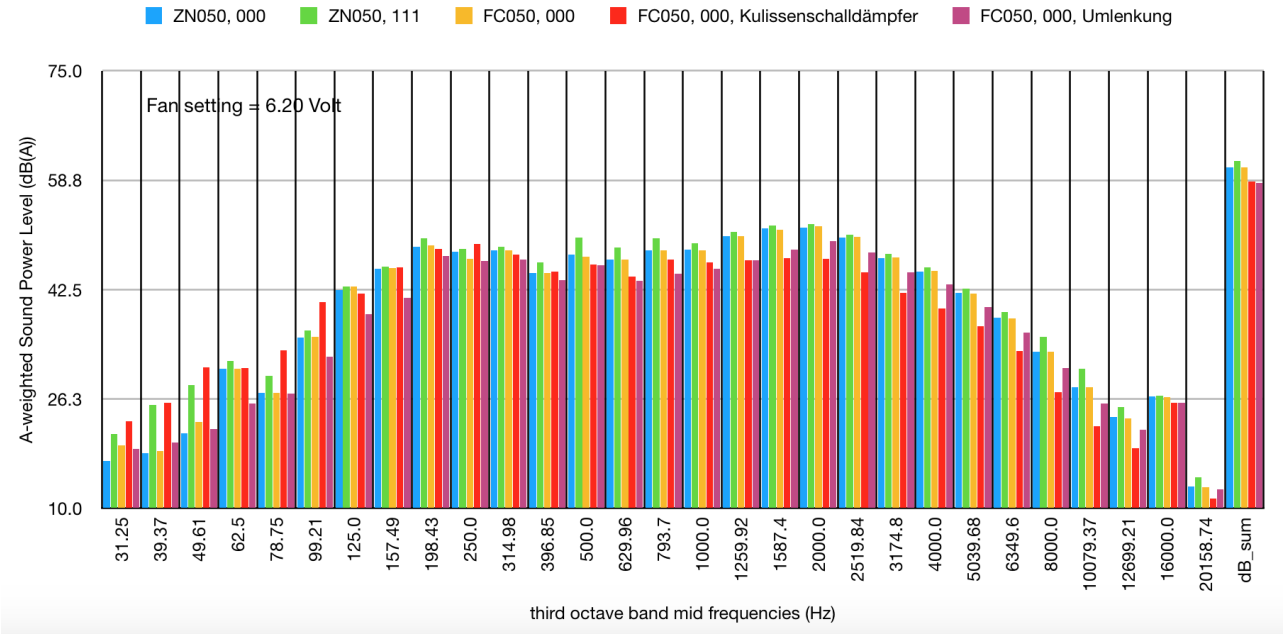

Figure 57: Spectral representation of the A-weighted sound power level for a fan control voltage of 6.20 Volt for 2 different fans and different sound insulation measures

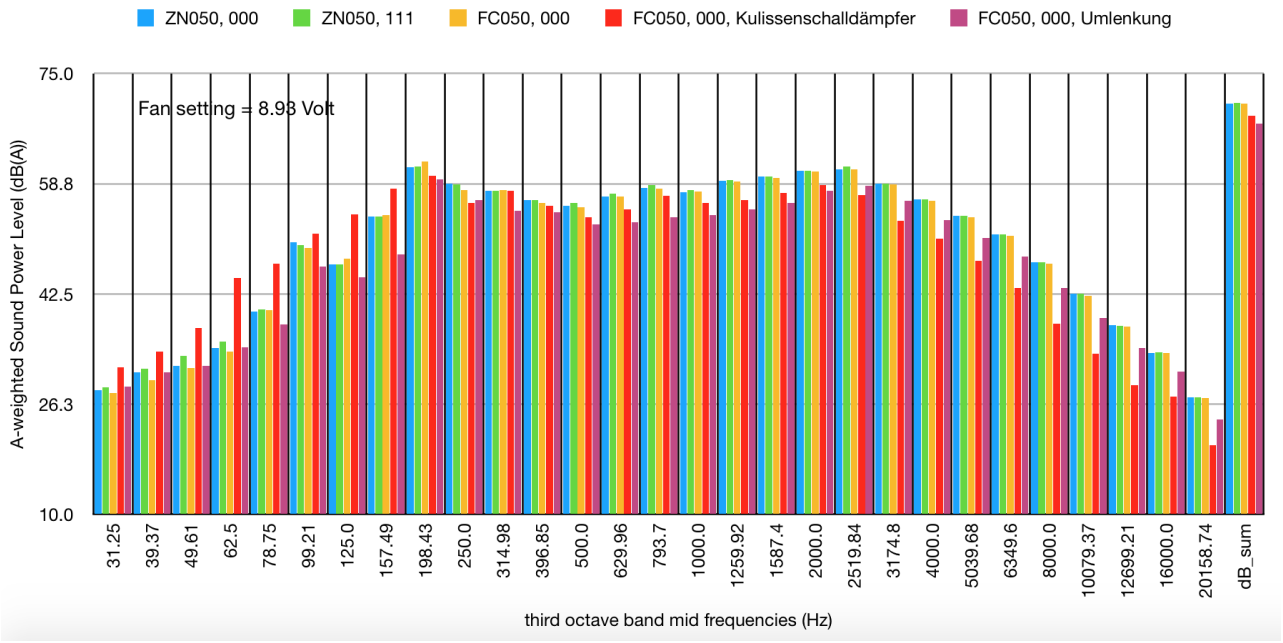

Figure 58: Spectral representation of the A-weighted sound power level for a fan control voltage of 6.20 Volt for 2 different fans and different sound insulation measures

The directional dependency of the sound emissions is shown as an example for a fan control voltage of 6.20 Volt with switched off climatic chamber technology for the fan ZN050 without and with deflection. The microphones 05, 13, 21, 29, 37 and 45 are arranged around the heat pump. Microphone 64 hangs above the heat pump.

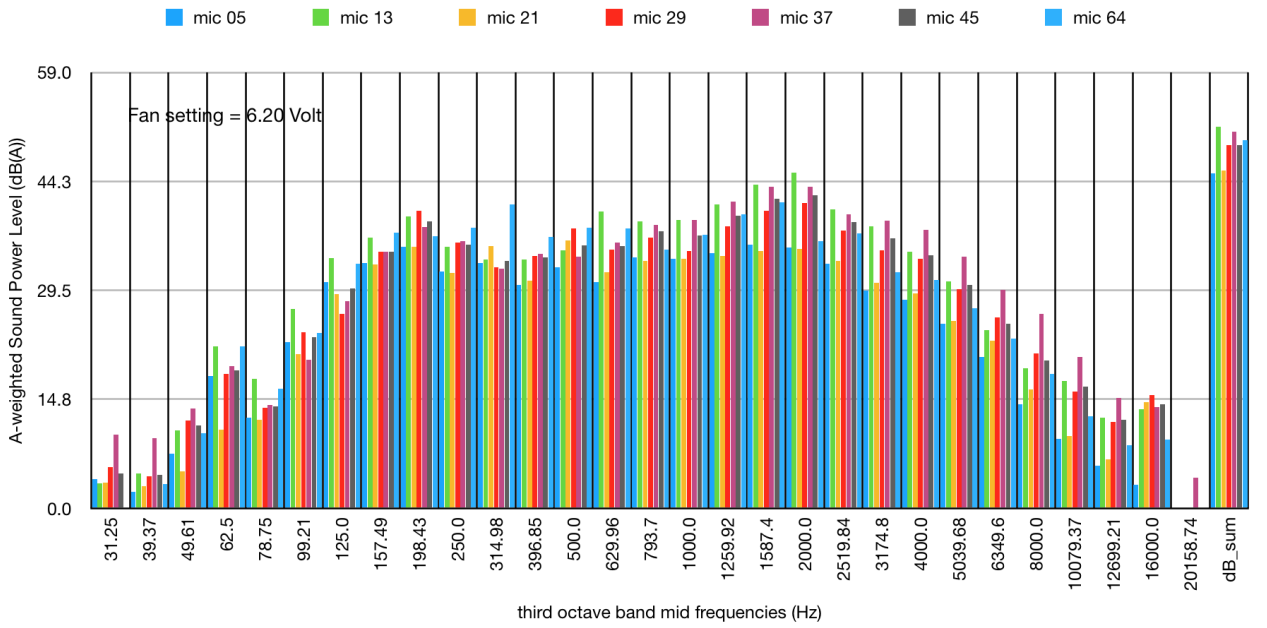

Figure 59: Spectral representation of the A-weighted sound pressure level for a fan control voltage of 6.20 Volt for the fan ZN050 without constructional measures when the climatic chamber technology is switched off. The spectrums of different microphones are shown (see Figure 38).

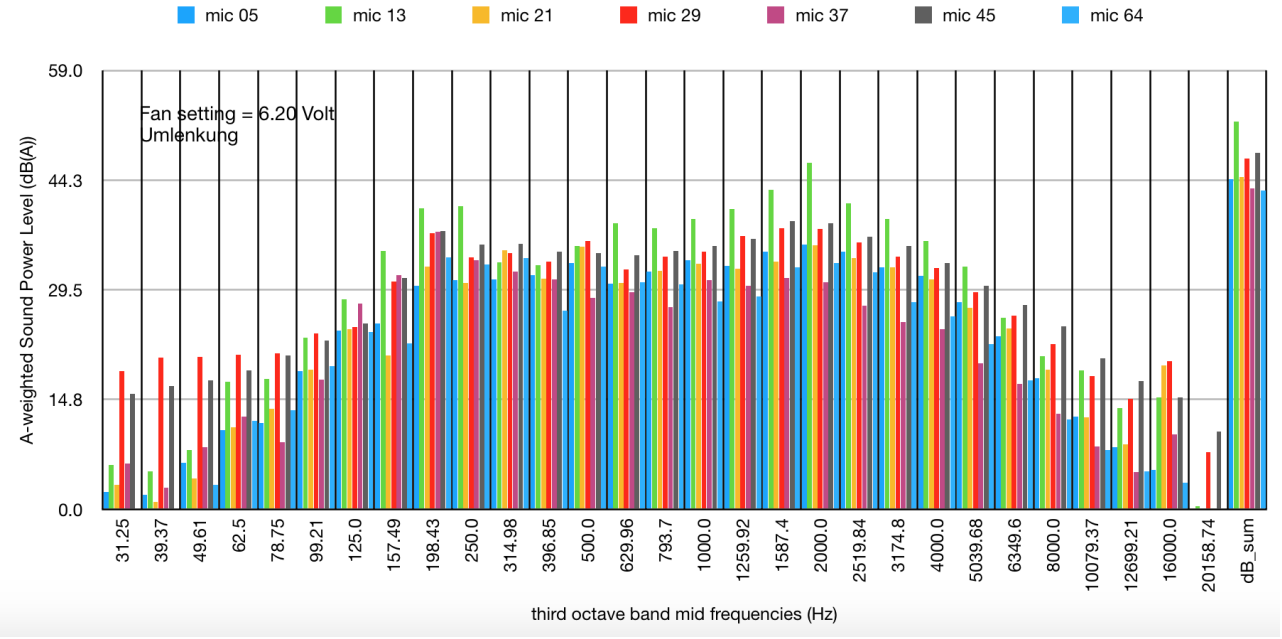

Figure 60: Spectral representation of the A-weighted sound pressure level for a fan control voltage of 6.20 Volt for the fan ZN050 with deflection when the climatic chamber technology is switched off. The spectrums of different microphones are shown (see Figure 63).

Measurements as a function of the compressor speed followed. Shown are both sound power levels and sound pressure levels at selected microphone positions.

Table 7 and Figure 61: A-weighted sound power level as a function of compressor speed

Fan FC050, fan setting 2.68 Volt, climate chamber: water pump, humidity and air temperature control on	
compressor speed (Hz)	**SPL dB(A), 100**
0	52,4
30	53,6
40	55,2
50	56,3
60	59,4
70	61,3
80	63,4
90	63,7
94	69,0
100	70,1
110	72,1
120	73,5

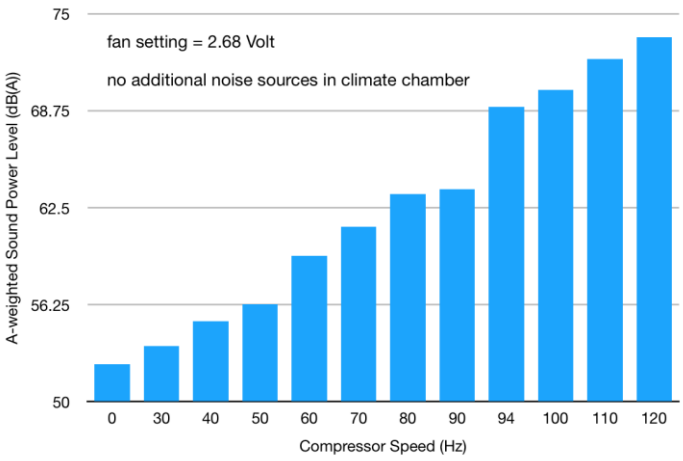

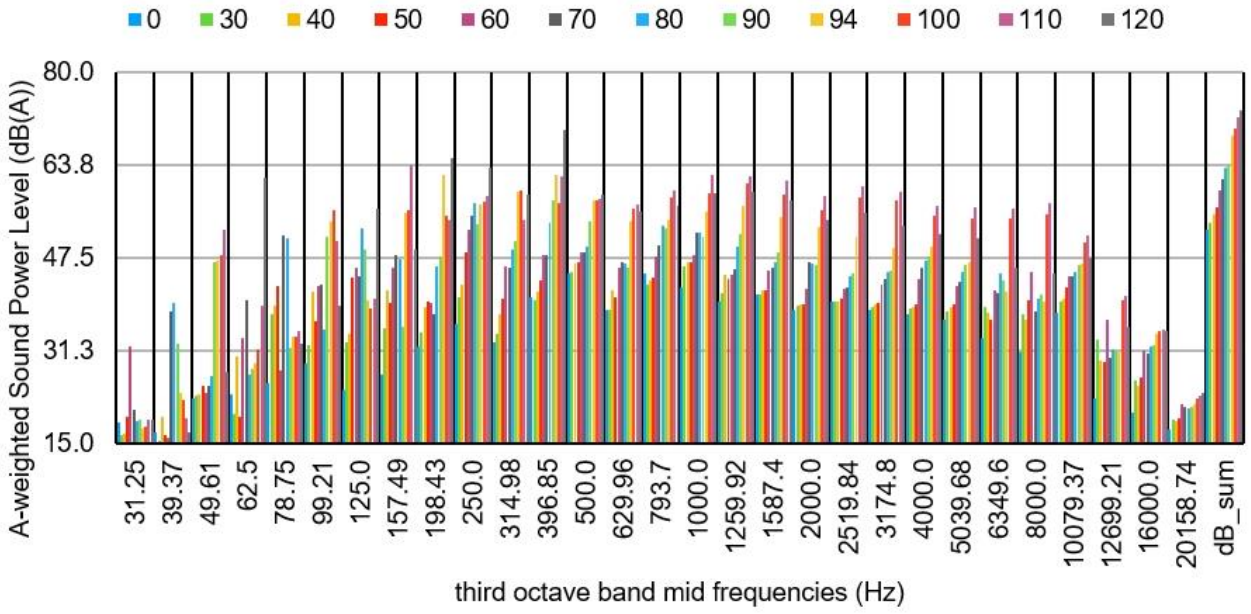

Figure 62: Spectral representation of the A-weighted sound power level as a function of compressor speed

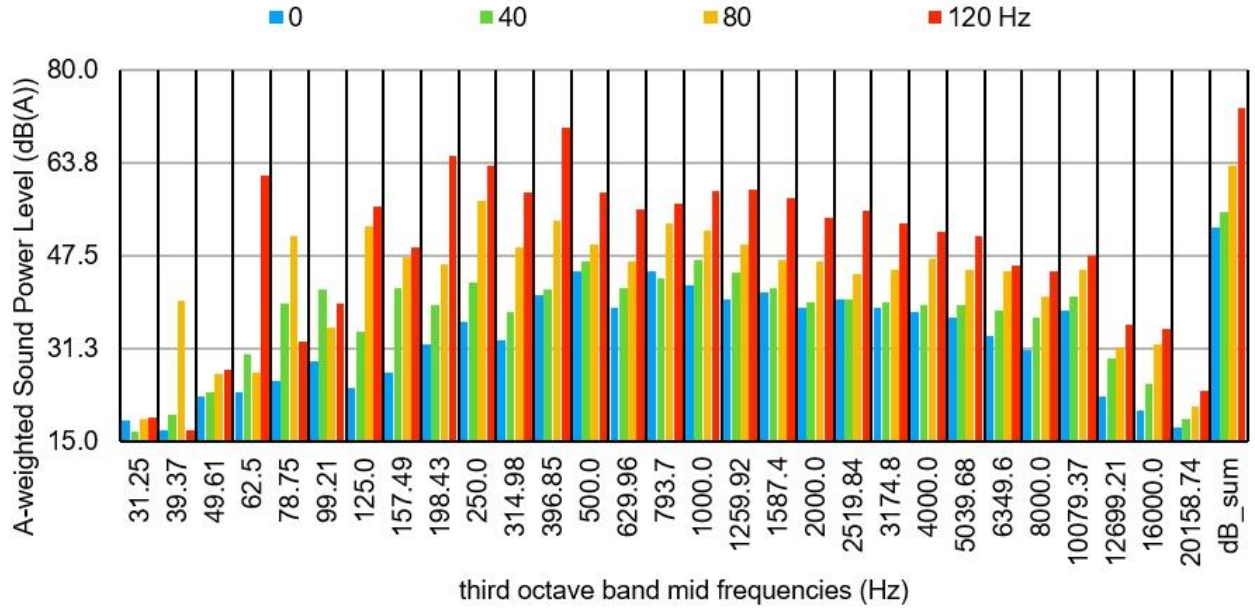

Figure 63: Detailed spectral representation of the A-weighted sound power level as a function of compressor speed

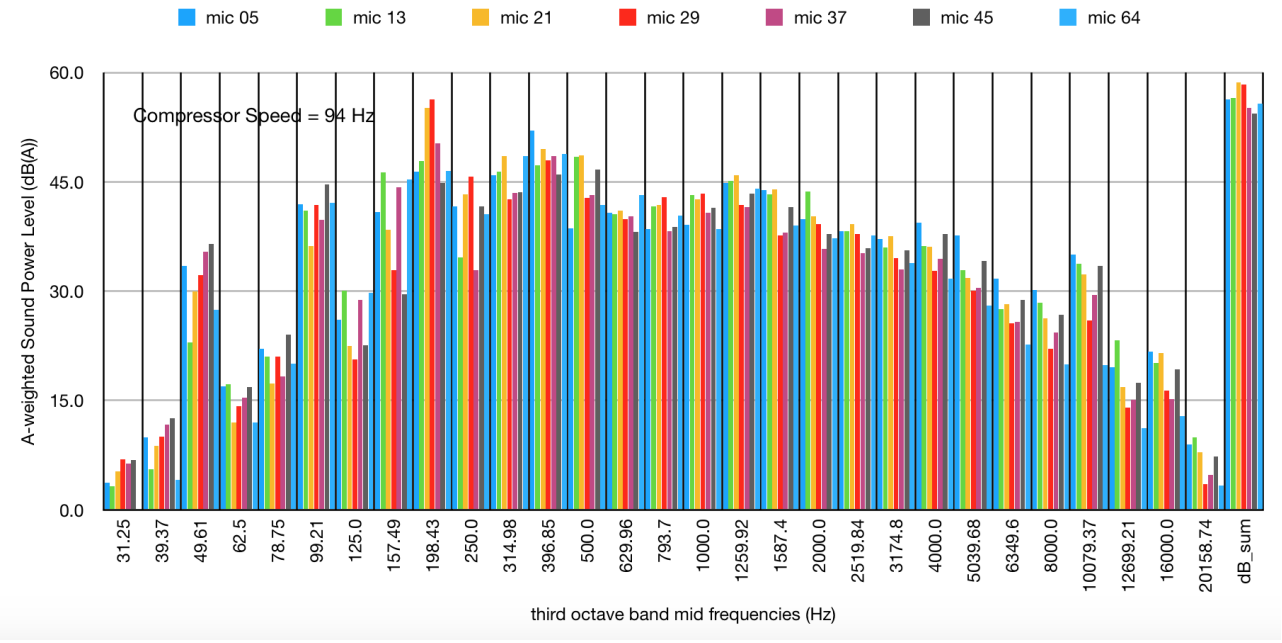

Figure 64: Spectral display of the A-weighted sound pressure level for a compressor speed of 94 Hz. The spectra of different microphones are shown (see Figure 38).

All further measurements were carried out with the heat pump in operation, using different heat exchangers: a convectional vertical tube-fin heat exchanger, an inclined aluminium microchannel heat exchanger and the coated convectional vertical tube-fin heat exchanger. Table 8 summarises the results. An example of the time histories is given in Appendix 7.1.

Table 8: Summary of the results

Measurement	L_w.min dB(A)	L_w,max dB(A)	Fantype	Constructive Measures	Climate chamber	Note
Nov. 17-16	65	68	ZN050	Diffuser	A2W35	P_fan ca. 50W
Nov. 17-17	66	69	FN050	-	A2W35	P_fan ca. 65W
Nov. 17-18	66	69	FC050	-	A2W35	P_fan ca. 85W
Nov. 17-19	66	66,5	FC050	Deflection baffle silencer	A2W35	P_fan ca. 85W
Nov. 17-20	66	67	FC050	Deflection	A2W35	P_fan ca. 85W
Nov. 18-01	68	71	ZN050	-	A10W35	Testrun 12.11. / 15:13
Nov. 18-02	67,5	70	ZN050	-	A10W35	Testrun 12.11. / 15:42
Nov. 18-03	69,5	70,5	ZN050	-	A8W35	12.11. / 15:56
Nov. 18-04	62,5	63	ZN050	-	A10W35	Testrun 12.11. / 15:59
Nov. 18-05	67,8	70	ZN050	-	A2W35	13.11. / 11:27
Nov. 18-06	67,5	71	ZN050	-	A2W35	13.11. / 13:16
Nov. 18-07	68	71.5	ZN050	Diffuser	A2W35	13.11. / 15:08

Nov. 18-08	61 (48,5)	61,5 (50)	ZN050	Diffuser Comp = 94, fan = 594	A2W35	14.11. / 12:41
Nov. 18-09	65* (53)	68* (56)	ZN050	Diffuser Foam on Compressor Comp = 64, fan = 594	A2W35	14.11./ 14:41
Nov. 18-10	64* (52)	65* (53)	ZN050	Microchannel-HEX Diffuser Comp = 47, fan = 594	A2W35	14.11. / 16:54
Nov. 18-11	64* (52)	66.5* (54.5)	ZN050	Diffuser But Sponge removed Comp = 94, fan = 445.5	A2W35	15.11. / 07:24
Nov. 18-12	64* (52)	67* (55)	ZN050	Comp = 94, fan = 400	A2W35	15.11. / 08:33
Nov. 18-13	64,5* (52,5)	65.5* (53,5)	ZN050	Comp = 70.5, fan = 594	A2W35	15.11. / 09:42
Nov. 18-14	66* (54)	70* (58)	ZN050	Diffuser	A2W35	16.11. / 14:36
Nov. 18-15	65* (53)	70* (58)	ZN050	Diffuser, Comp = 94	A2W35	19.11. / 13:02
Nov. 18-16	65* (53)	79* (57)	ZN050	Diffuser, Comp = 94	A12W35	20.11. / 09:21
Nov. 18-17	65.5* (53,5)	70* (56)	ZN050	Diffuser, Comp = 94	A10W35	21.11. / 15:07
Nov. 18-18	66 (53)	67 (55)	ZN050	Diffuser, Comp = 94, fan = 594 Wheels removed, spring added	A12W35	22.11. / 11:01
Nov. 18-19	66,5	69	ZN050	Diffuser, Comp = 94, fan = 594 Spring removed, dampers added	A12W35	22.11. / 14:26
Nov. 18-20	35,5		ZN050	Background (1,0,0) **	20°C	23.11. / 07:23
Nov. 18-21	35		ZN050	Background (0,0,0) **	20°C	23.11. / 07:25
Nov. 18-22	56,5		ZN050	Background (1,0,1) **	20°C	23.11. / 07:28
Nov. 18-23	57		ZN050	Background (1,1,1) **	20°C	23.11. / 07:35
Nov. 18-24	36	38	ZN050	Background (0,0,0) **	20°C	23.11. / 07:37
Mar. 19-01	67	72.5	ZN050	-	A2W35	
Mar. 19-02	67	71	ZN050	-	A2W35	
Mar. 19-03	67	70,5	ZN050	Diffuser (no grid on fan, grid only on diffuser)	A2W35	
Mar. 19-05	69	70	FC050	-	A2W35	unstable

Mar. 19-06	67,5	71.5	FC050	-	A2W35	
Mar. 19-07			FC050	Cover above compressor		Compressor scan
Mar. 19-08			FC050	Cover above compressor		Fan scan
Mar. 19-09	64	67,5	FC050	Cover above compressor	A7W35	
Mar. 19-10	64	67.5	FC050	Cover above compressor	A4.5W35	
Mar. 19-11	65	69	FC050	Cover above compressor	A0W35	

** SPL calculated from Mic 64 position*

*** Setting (x,y,z): x = water pump, y = humidifier, z = air flow of the climate chamber*

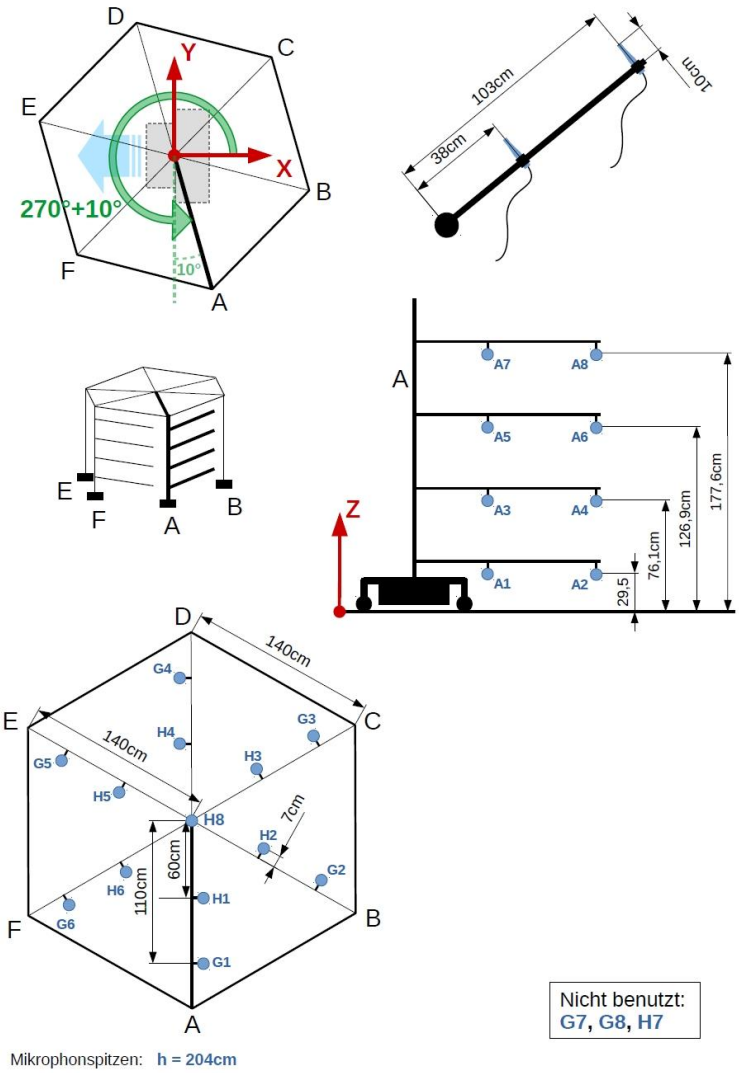

Figure 65: Representation of the construction of the acoustic dome. The microphone positions for the representation of the directional dependency are drawn in.

Investigation of the effects of icing

Figure 66 shows the positioning of a high-resolution camera in front of the SilentAirHP heat exchanger. The frost behaviour is shown as an example in Figure 67 and the defrost behaviour in Figure 68. An image analysis allows the extraction of a "highlight event" curve,

which is shown in Fig. 69 together with the transient weight signal. This allows a characterization of the icing behavior. The asymmetrical icing due to the asymmetrical temperature distribution of the fins, which is imposed by the tubes, is finally shown in Figure 70. The effect of icing on the sound power level is also shown in Table 8 as the difference between minimum and maximum. It is approximately 2 - 4 dB(A).

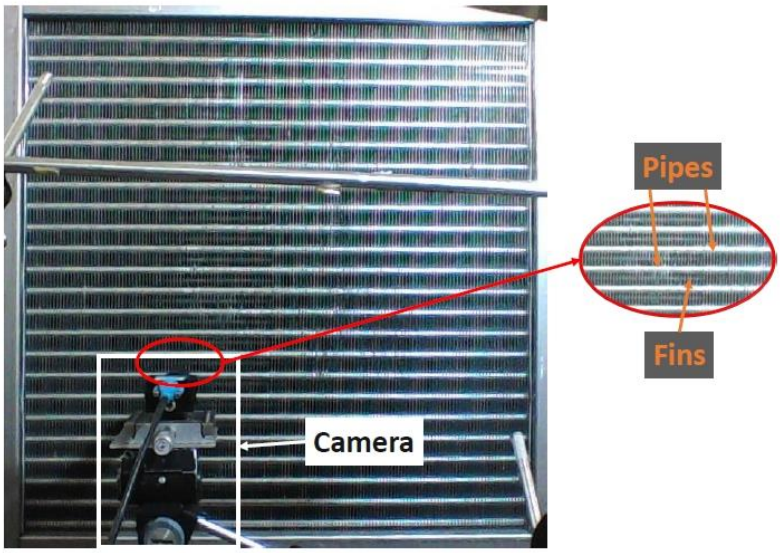

Figure 66: Surface of the SilentAirHP heat exchanger and the macro camera to visualize the frost accumulation on the heat exchanger fins.

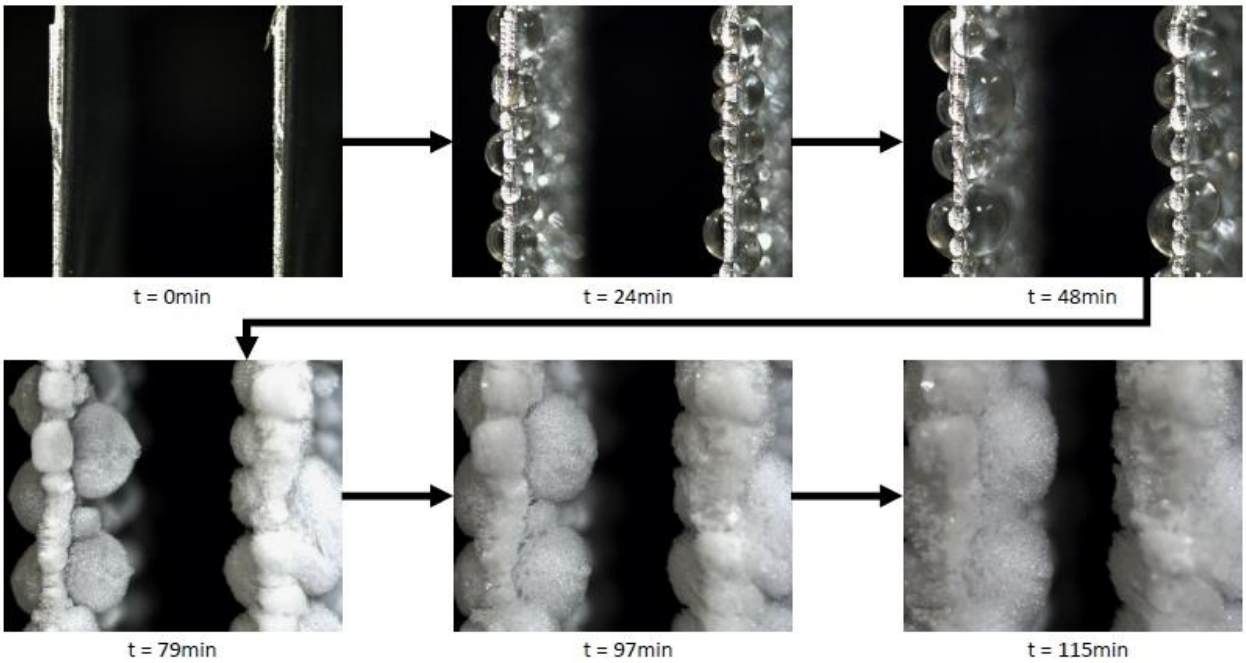

Figure 67: Frost accumulation on two fins of the SilentAirHP heat exchanger

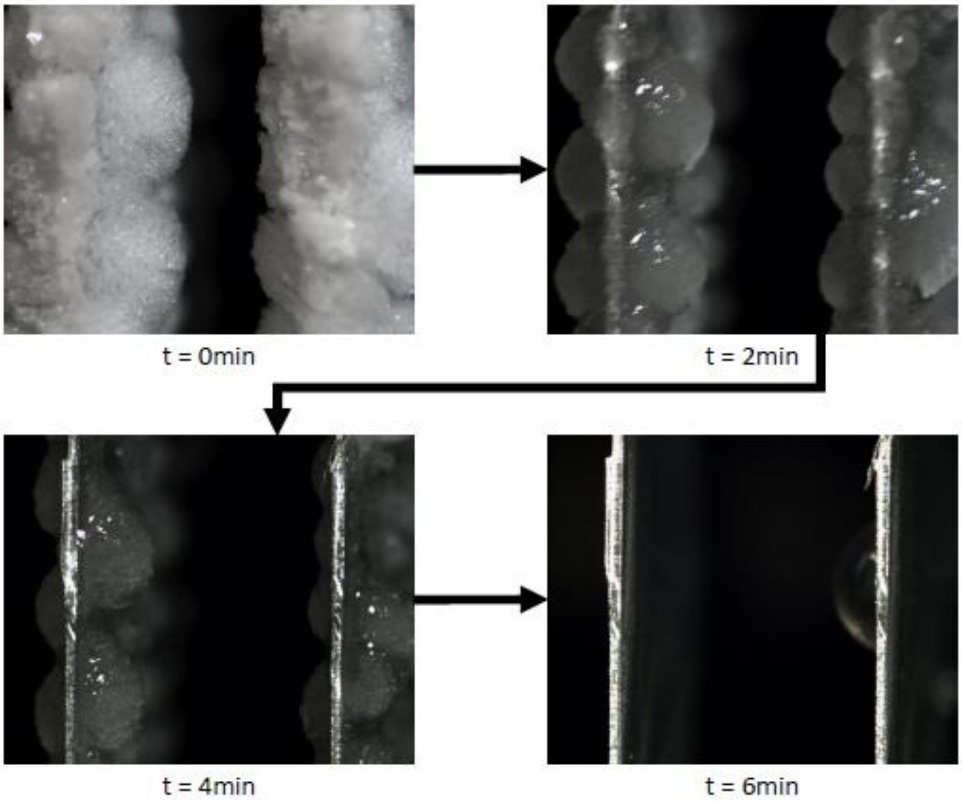

Figure 68: Defrosting behaviour of the SilentAirHP heat exchanger

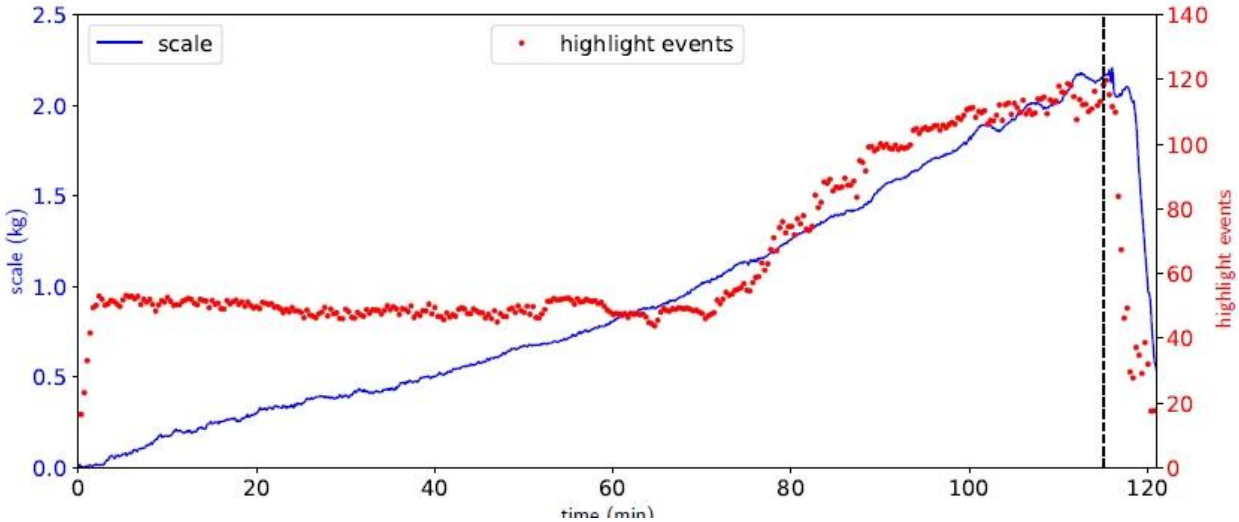

Figure 69: Weight measurement and number of highlight events based on SilentAirHP image analysis during freeze and defrost operation. The time during which defrosting is initiated is indicated by a dotted line.

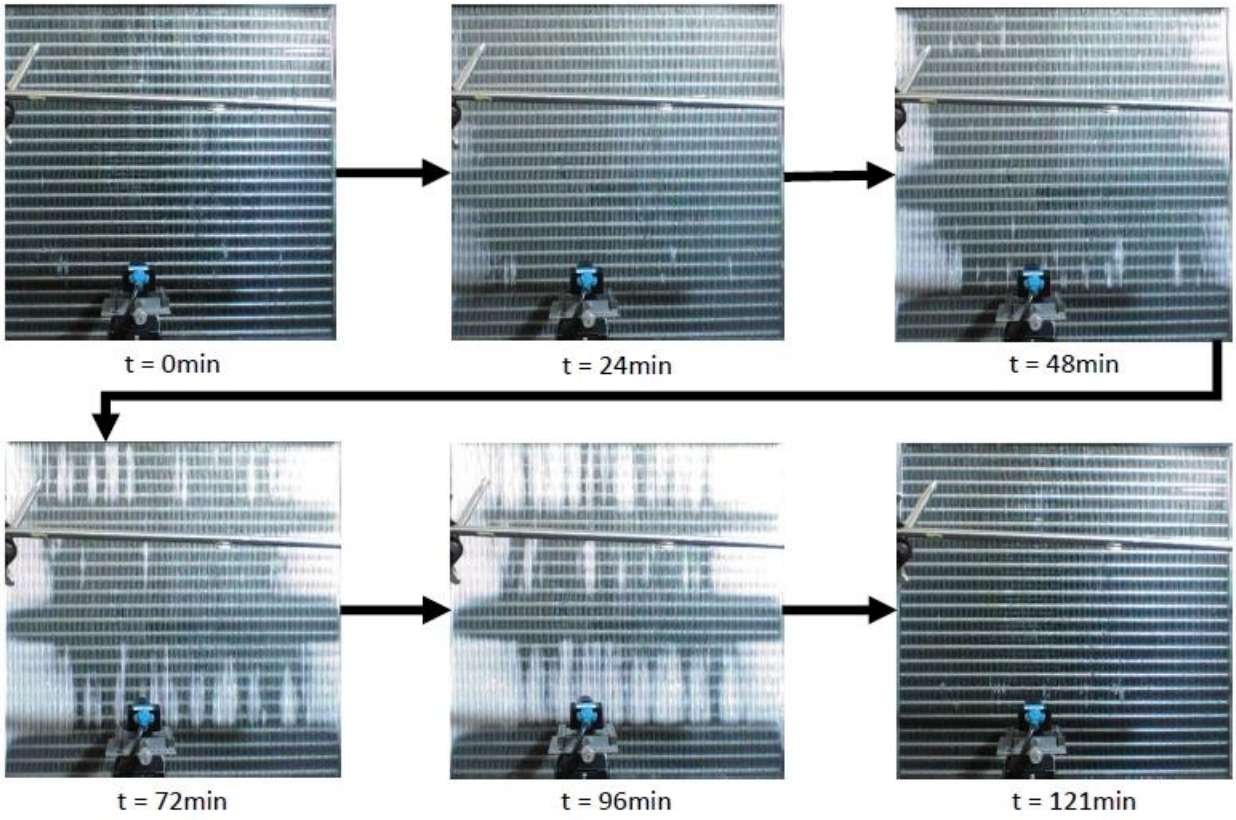

Figure 70: Uneven frost formation on the heat exchanger surface of the SilentAirHP.

Investigation of sound-critical areas

Simultaneous measurements of flow turbulence, wall pressure fluctuations and emitted sound power were performed. As described above, this method of an internally installed heat pump and two different heat pumps was successfully tested in the climatic chamber (see also Fig. 68 - 70). Vibration measurements were also carried out on the SilentAirHP.

Psychoacoustics

The aim of the investigation was to psychoacoustically evaluate noise from heat pumps in different directions and using different, potentially noise-reducing, measures.

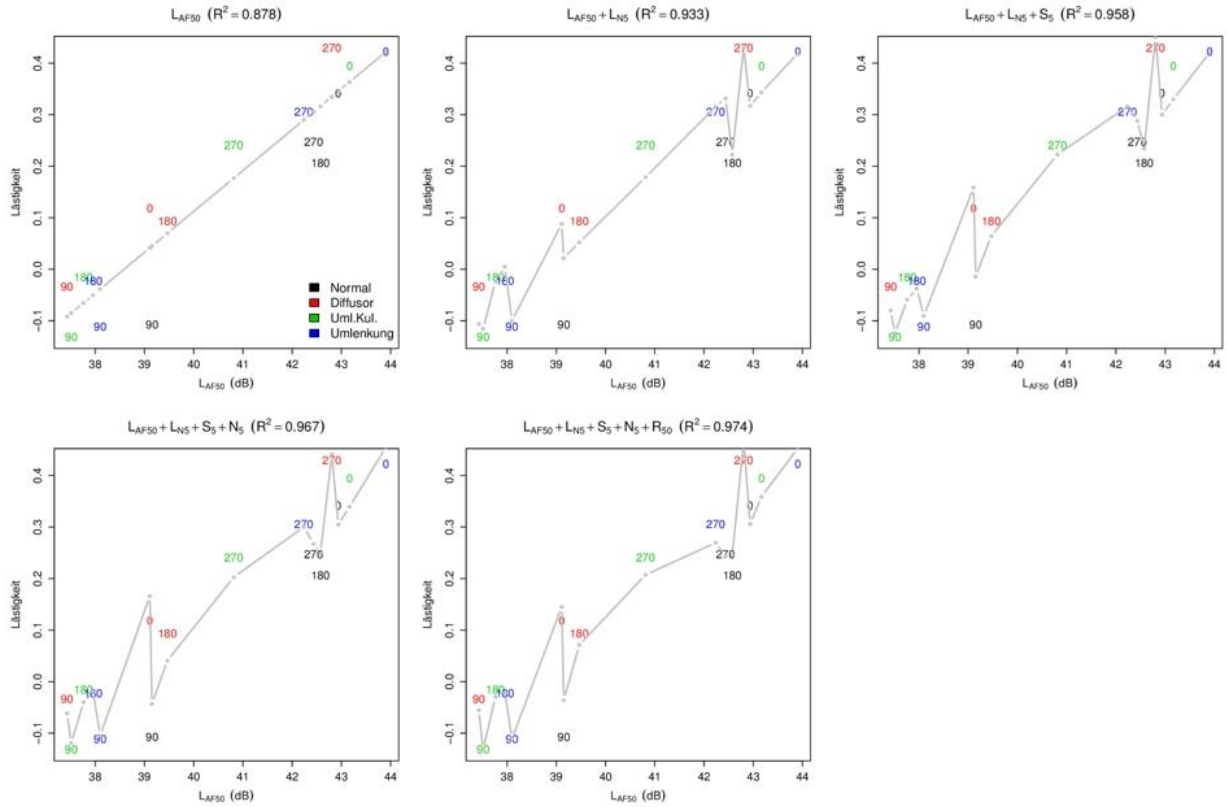

Figure 71: Annoyance as a function of the L_{AF50} and the gradual model selection including model fit (grey line)

From these measurements, the correlation between annoyance judgements for the heat pumps and the L_{AF50}[6] was clear.
The line shows the estimation based on the prediction of the linear model shown in the title. Furthermore, the proportion of the explained variance is also shown (R2). Here we can see that the L_{AF50} tends to explain the judgments and how the successively added parameters capture the existing variance better and better. The increase of the explained variance by the last two parameters is less than 2% (95.8% to 97.4%).

The following main points have emerged from the investigations:

- The effect of the different measures on the different acoustic and psychoacoustic levels is highly directional. Differences can be observed especially in levels, loudness and sharpness
- This dependency between measure and direction also continues in perception, which is shown by a significant statistical interaction between position and state.
- There was also a significant overall effect of the measuring position for the annoyance judgements. Due to the significant interaction with the factor measure, these effects must be interpreted with caution.
- The differences in the annoyance judgments can be explained very well by A-level and volume level. The additional use of psychoacoustic sharpness and also

[6] Sound pressure level that is exceeded 50% of the time in dB (A)

roughness contribute to a better explanation.

Finally, it is important to mention that the acoustic data used for the psychoacoustic analyses were emission measurements. Above all, the directional dependency can change due to distance and also due to the way the heat pump is installed. In order to investigate the directional dependency more precisely even at greater distances, measurements in corresponding situations and further perception tests would be necessary.

4 Results and conclusions

The SilentAirHP project was able to provide a quantitative overview of a large number of noise reduction measures. Within the project a number of services for heat pump manufacturers were established:

- Time correlated vibration-acoustic flow velocity measurements for the detection of sound and vibration sources
- Sound source localization with microphone rings and thermal imaging cameras
- Transient, direction-, frequency- and location-dependent measurement of the sound pressure level and from this calculated transient sound power level of heat pumps under defined climatic conditions (in the climate chamber).
  Coupling of energetic and acoustic models within the framework of 1D simulation tools (SSELib)
- Transient characterization of heat pumps with thermal imaging camera, detail cameras (frost detection with edge and highlight event detection), weight determination and acoustic dome.
- 3D simulation calculations to determine the icing of heat pump evaporators

The results of the SilentAirHP are an essential contribution to the project "Acoustic Signatures of Heat Pumps" of the International Energy Agency (Annex 51) [20], which is coordinated by Austria. Furthermore, an app for iOS has been developed in recent years, which allows the visualization of the sound emissions of heat pumps using augmented reality. The relevant data is provided by a transient 5-channel measurement method derived from the analysis tool of the acoustic dome.

5 Outlook and recommendations

As far as possible, each system must be considered individually, since the sound emissions of a heat pump are the result of a complex interplay of different sound generation mechanisms (vibrating surfaces, sound radiating flows, engine noise) and sound propagation mechanisms. In the case of the SilentAirHP, for example, the compressor was the dominant sound source and adaptations at the fan only become effective at low compressor speed. However, many units do not position the compressor in the outdoor unit, so changes to the

fan are essential. In principle, of course, adaptations should always be made on the loudest component with priority. Location and consideration of the directional dependency of the acoustic emissions are essential aspects. In the last three years, Austrian manufacturers have also done a lot of work in the field of acoustics, so that sound laboratories are now also available on site. Load shifting and the implementation of "SilentModes" are now common procedures for modern heat pumps.

At AIT, a simplified form of transient 5-channel acoustic measurement derived from the acoustic dome methodology is now being carried out for the usual certification measurements, which will subsequently provide the database for the visualization mobile app (currently iOS). Further work will be carried out in the FFG project "RAARA" (Residential Area Augmented Reality Acoustics, FFG-No. 873588) starting October 2019. Thus, transient sound power levels in the main directions of the heat pump are available, which allow a simplified direction-dependent acoustic visualization.

6 Bibliography

[1] Ch. Reichl, J. Emhofer, Ch. Köfinger, T. Fleckl: “SilentAirHP - Advanced Methods for Analysis and Development of Noise Reduction Measures for Air-to-Water Heat Pump Systems”, 66. Jahrestagung der Österreichischen Physikalischen Gesellschaft, Universität Wien, 27.09.2016

[2] N. Schmiedbauer, J. Emhofer, Ch. Köfinger, P. Wimberger, T. Fleckl, M. Gröschl, Ch. Reichl: “Active Noise Cancelling for Heat Pump Applications”, 66. Jahrestagung der Österreichischen Physikalischen Gesellschaft, Universität Wien, 27.09.2016

[3] P. Wimberger, J. Emhofer, Ch. Köfinger, T. Fleckl, M. Gröschl, Ch. Reichl: “Space-, time- and frequency resolved recording and analysis of sound emissions and sound source localisation using a multichannel measuring system”, 66. Jahrestagung der Österreichischen Physikalischen Gesellschaft, Universität Wien, 27.09.2016

[4] P. Wimberger: "Sound source localisation and space-, time- and frequency resolved analysis of sound emissions using a multichannel measuring system"; Bachelorarbeit; Betreuung: M. Gröschl, Ch. Reichl, J. Emhofer; TU Wien, Institut für Angewandte Physik, 2016.

[5] N. Schmiedbauer: “Active Noise Cancelling im Anwendungsfeld der Luft-Wasser-Wärmepumpen“ (working title). Diploma Thesis (in finalisation), Supervision: Prof. Martin Gröschl, TU Wien, Christoph Reichl, AIT

[6] Dymola: https://www.3ds.com/de/

[7] Modelica: https://www.modelica.org

[8] TIL-Library: https://www.tlk-thermo.com/

[9] ThermoCylcle-Library: http://thermocycle.net/

[10] J. Emhofer, R. Zitzenbacher, Ch. Reichl: "Sound Source Extension Library for Modelica"; Vortrag: 12th International Modelica Conference, Prag, Tschechische Republik; 15.05.2017 - 17.05.2017; in: "Proceedings of the 12th International Modelica Conference", Modelica Association, (2017), ISBN: 978-91-7685-575-1; 8 S.

[11] D. Meisl: „Implementierung einer softwarebasierten Regelung einer Luft-Wasser-Wärmepumpe“, Diploma Thesis; Supervision: G. Grabmair (FH Oberösterreich), J. Emhofer (AIT), 2017; Final exam 20.09.2017

[12] Ch. Reichl: "Heat and Mass Transfer in Renewable Energy Systems"; Habilitation Thesis, Technische Unversität Wien, Faculty of Mechanical and Industrial Engineering, Institute of Fluid Mechanics and Heat Transfer, 2018.

[13] M. Popovac, J. Emhofer, E. Wasinger, P. Wimberger, R. Zitzenbacher, D. Meisl, F. Linhardt, N. Schmiedbauer, Ch. Reichl: "OpenFOAM implementation of algebraic frosting model and its applications on heat pump evaporators"; Talk: 13th IIR Gustav Lorentzen Conference 2018, Valencia, Spain; 18.06.2018 - 20.06.2018; in: "13th IIR Gustav Lorentzen Conference on Natural Refrigerants (GL2018). Proceedings", IIF/IIR, (2018), Paper-Nr. 1203, 9 S.

[14] N. Schmiedbauer: „Active Noise Cancelling im Anwendungsfeld der Luft-Wasser-Wärmepumpen“ (Arbeitstitel). Diplomarbeit (in Fertigstellung); Betreuung: M. Gröschl, TU Wien, Ch. Reichl, AIT

[15] N. Schmiedbauer, J. Emhofer, C. Köfinger, P. Wimberger, T. Fleckl, M. Gröschl, C. Reichl: "Aktive Störschallunterdrückung für Wärmepumpenanwendungen"; Talk: 43. Jahrestagung für Akustik, Kiel; 06.03.2017 - 09.03.2017; in: "Fortschritte der Akustik - DAGA 2017", Deutsche Gesellschaft für Akustik e.V. (DEGA), (2017).

[16] F. Linhardt: "Simultaneous measurements of sound, vibration, and flow, as well as determination of acoustic transfer functions in the context of air water heat pumps"; Diplomarbeit; Betreuung: M. Gröschl, Ch. Reichl; Technische Unversität Wien, Institut für Angewandte Physik, 2018; Abschlussprüfung: 19.03.2018.

[17] F. Linhardt, K. Alten, J. Emhofer, C. Köfinger, T. Fleckl, P. Wimberger, M. Gröschl, Ch. Reichl: "Charakterisierung der Schallabstrahlung von Luft-Wasser-Wärmepumpen mittels simultaner Hitzdrahtanemometrie, Vibrationsmessung und Schalldruckbestimmung"; Talk: 43. Jahrestagung für Akustik, Kiel; 06.03.2017 - 09.03.2017; in: "*Fortschritte der Akustik - DAGA 2017*", Deutsche Gesellschaft für Akustik e.V. (DEGA), (2017), S. 1238 - 1241.

[18] R. Zitzenbacher: *"Schallreduktionsmaßnahmen für Luft/Wasser-Wärmepumpen";* Diploma Thesis, Supervision: M. Steinbatz, J. Emhofer; FH Oberösterreich, 2017; Final exam: 20.09.2017.

[19] http://www.waermepumpe-austria.at/verein-waermepumpe-austria/leitfaden-zur-akustik-von-waermepumpen.html

[20] https://heatpumpingtechnologies.org/annex51/

Further reading (SilentAirHP)

Ch. Reichl, J. Emhofer, M. Popovac, G. Drexler-Schmid, P. Wimberger, F. Linhardt, K. Alten, T. Fleckl, Akustische Emissionen von Wärmepumpen, Chillventa, 15.10.2018, Nürnberg, Germany, invited talk

Ch. Reichl, J. Emhofer, M. Popovac, G. Drexler-Schmid, P. Wimberger, F. Linhardt, K. Alten, T. Fleckl, International research: acoustic signatures of heat pumps, 11de Warmtepomp Symposium, 10.10.2018, Communicatiehuis, Gent, Belgien, invited talk

P. Wimberger, J. Emhofer, Ch. Reichl, MicLocator - Determine multiple microphones’ positions using sound wave delayand trilateration, 68th Annual Meeting of the Austrian Physical Society, 11.09.2018, TU Graz, Austria

Ch. Reichl, J. Emhofer, M. Popovac, P. Wimberger, F. Linhardt, K. Alten, T. Fleckl: “*IEA HPT Annex 51: Acoustic Signatures of Heat Pumps Update - Acoustic Transmission Measurements and Sound Source Detection”*, 26th ERCOFTAC Alpe Danube Adria Pilot-Center Meeting, TU Graz, Austria, 24.10.2017

Ch. Reichl, J. Emhofer, T. Fleckl: „*HPT TCP Annex 51: Reduktion der Schallabstrahlung von Luft-Wasser-Wärmepumpen“*, European Heat Pump Summit, 22.-23.10.2017, Nürnberg, Deutschland.

Ch. Reichl, M. Popovac, E. Wasinger, D. Meisl, R. Zitzenbacher, F. Linhardt, P. Wimberger, N. Schmiedbauer, J. Emhofer, M. Gröschl: "*Experimental and numerical methods for the fluid dynamic and acoustic characterization of heat exchanger icing*"; Talk: 67. Jahrestagung der Österreichischen Physikalischen Gesellschaft (gemeinsam mit der Schweizerischen Physikalischen Gesellschaft), CERN und CICG, Genf, Switzerland; 21.-25.08.2017.

Ch. Reichl, J. Emhofer, F. Lörcher, A. Strehlow, M. Popovac, P. Wimberger, C. Köfinger, A. Zottl, T. Fleckl: "*Transient Acoustic Signatures of the GreenHP with special focus on icing and defrosting*"; Talk: 12th IEA Heat Pump Conference, Rotterdam, NL; 15.-18.05.2017; in: "*Proceedings of 12th IEA Heat Pump Conference*", (2017), ISBN: 978-90-9030412-0.

Ch. Reichl, M. Popovac, E. Wasinger, D. Meisl, R. Zitzenbacher, F. Linhardt, J. Emhofer: "*Icing of heat exchangers investigated by measurements and simulations on micro- and macroscale*"; Talk: 25th Ercoftac ADA Pilot Center Meeting und ERCOFTAC Spring Festival, Wien; 06.-07.04.2017.

Ch. Reichl, J. Emhofer, P. Wimberger, N. Schmiedbauer, F. Linhardt, E. Wasinger, C. Köfinger, T. Fleckl: "SilentAirHP - Analyse und Entwicklung von Schallreduktionsverfahren für Luft-Wasser-Wärmepumpen"; Talk: 43. Jahrestagung für Akustik, Kiel; 06.-09.03.2017; in: "Fortschritte der Akustik - DAGA 2017", Deutsche Gesellschaft für Akustik e.V. (DEGA), (2017), S. 1246 - 1249.

7 Appendix

7.1 Exemplary transient representation of the measurements

Uncoated vertical tube fin heat exchanger

Measurements November 2017

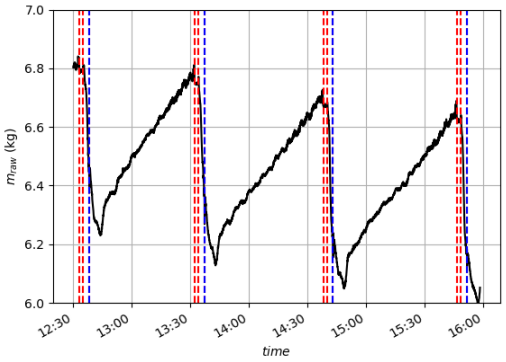

Nov17-16

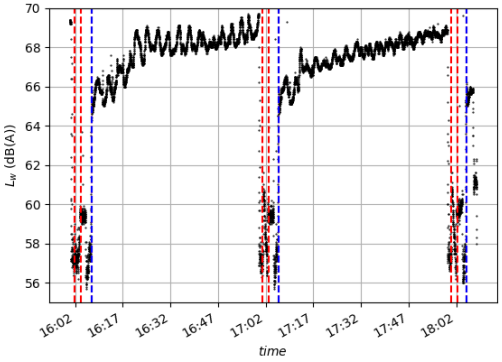

Nov17-17

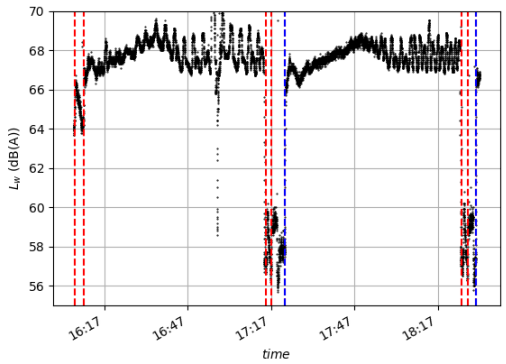

Nov17-18

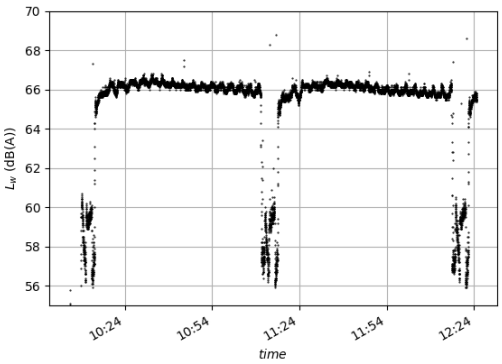

Nov17-19

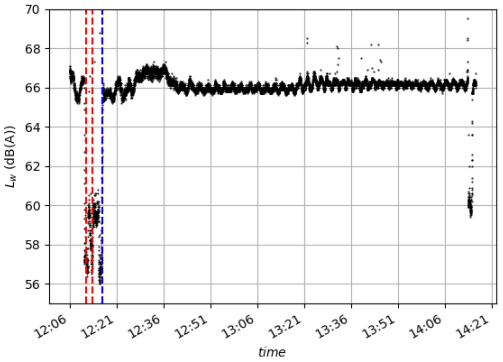

Nov17-20

Figure 7.1-1: Time history of A-weighted sound power levels for selected measurements

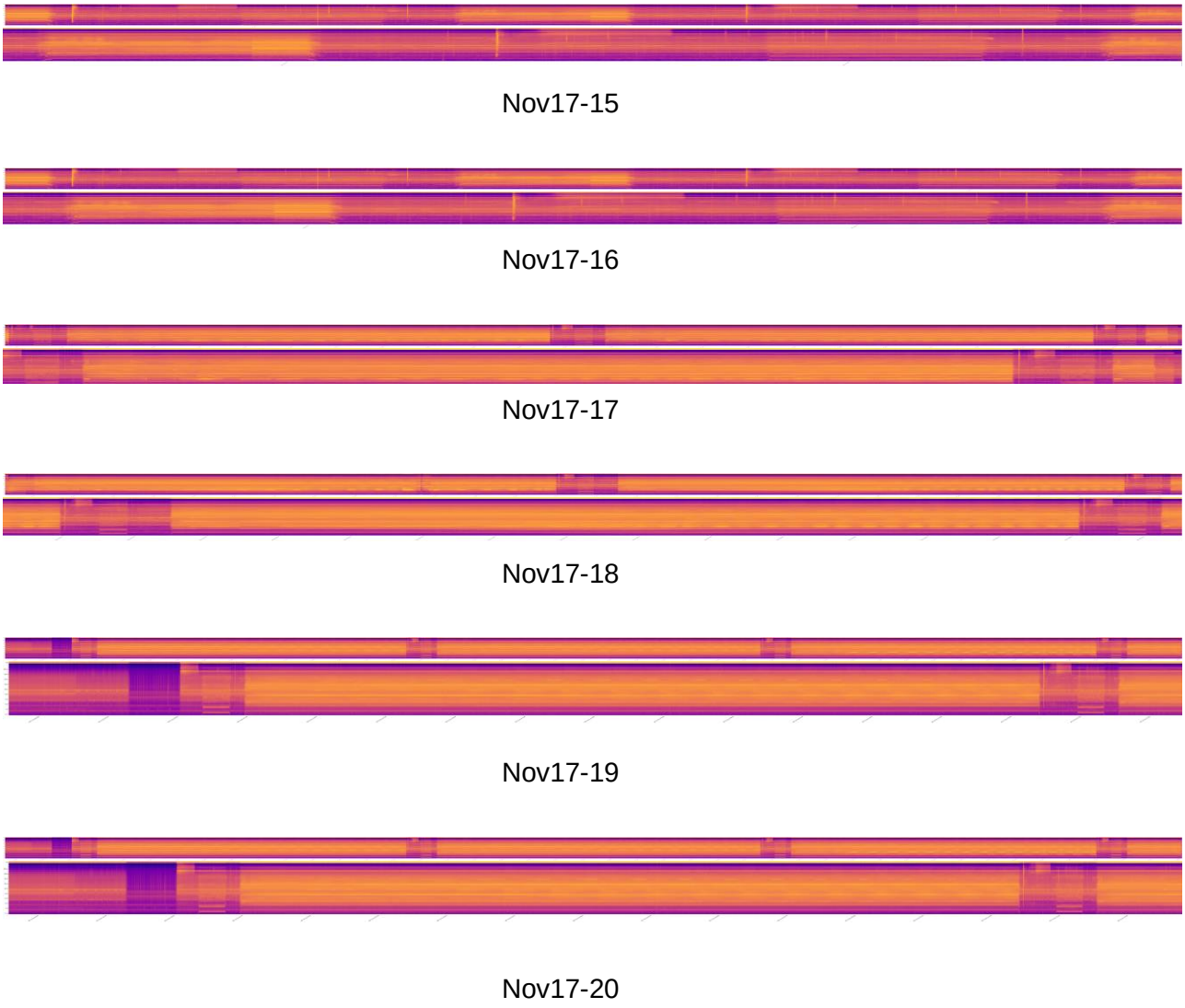

Figure 7.1-2: Time course of the frequency content of the A-weighted sound power level for selected measurements (waterfall diagrams) - in each case total and detailed period

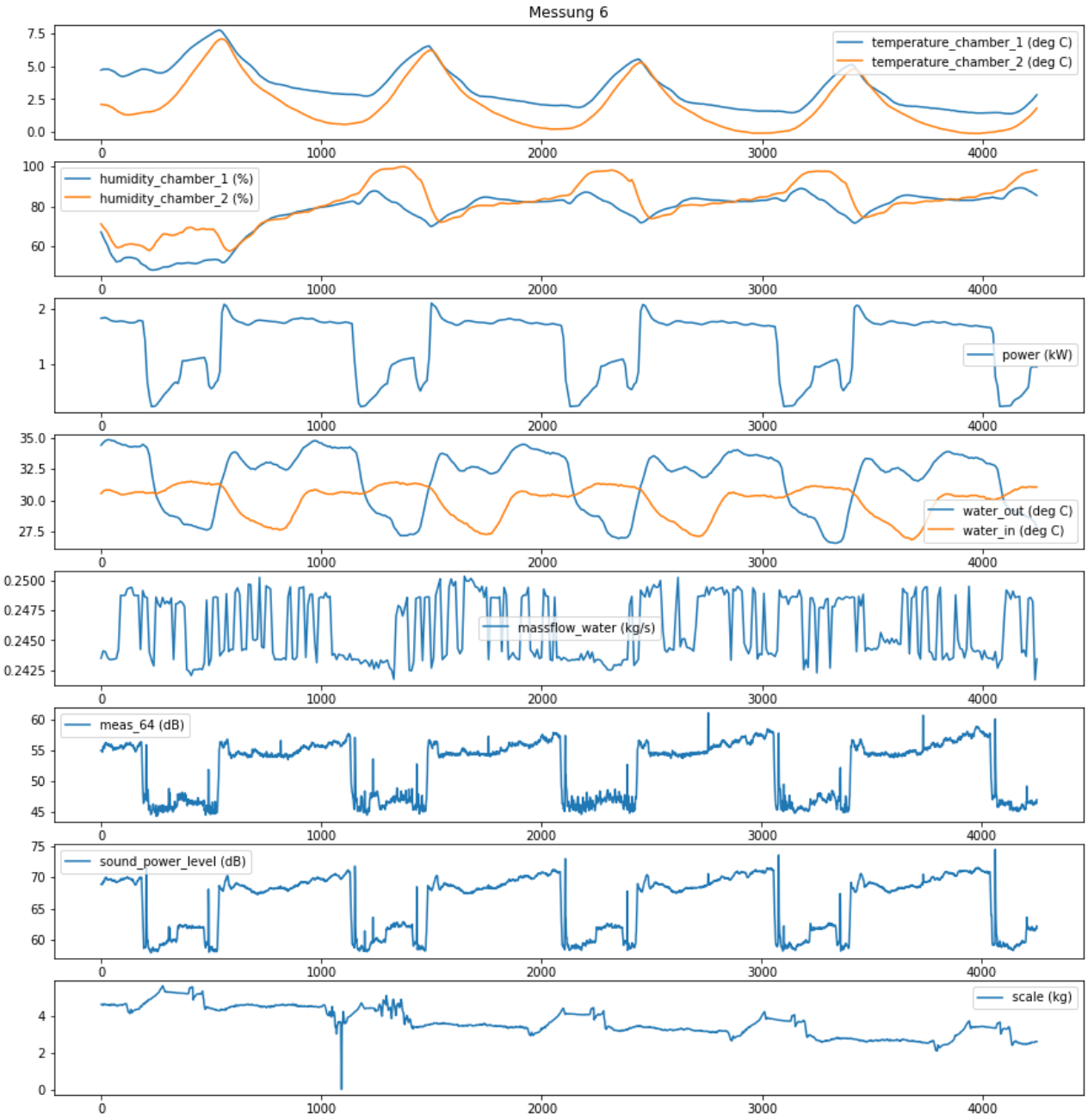

Figure 7.1-3: Time history of important climatic chamber data, weight and A-weighted sound power level for measurement Nov 18-06

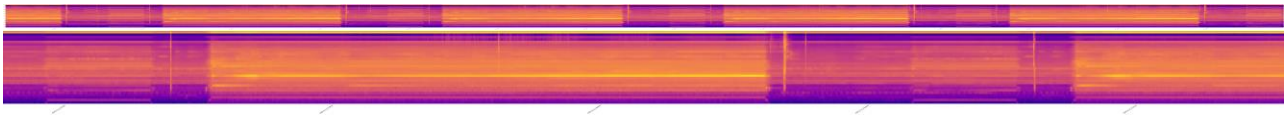

Figure 7.1-4: Time course of the frequency content of the A-weighted sound power level (waterfall diagrams) - in each case total and detailed period

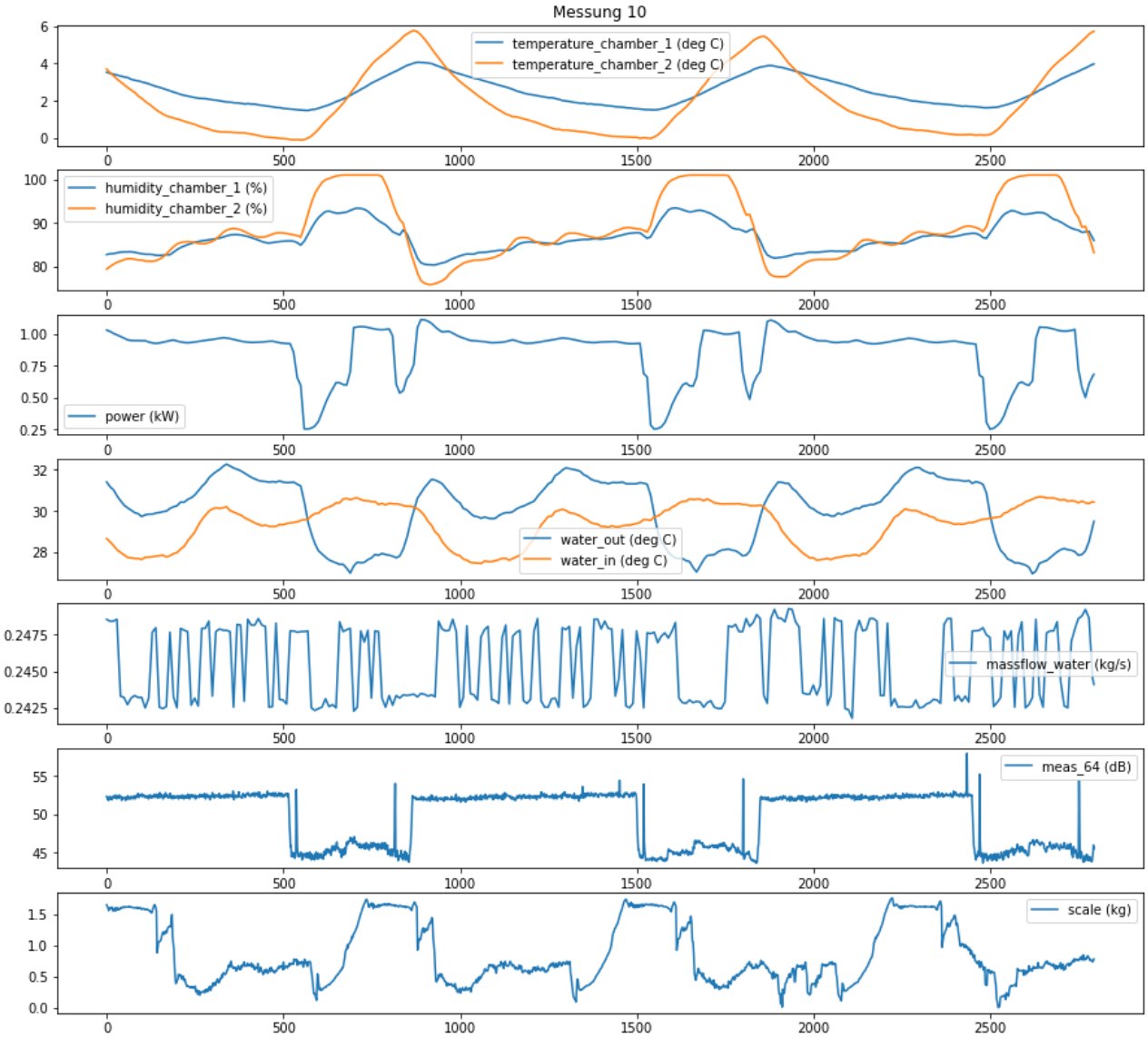

Figure 7.1-5: Time history of important climatic chamber data, weight and A-weighted sound power level for measurement Nov 18-10

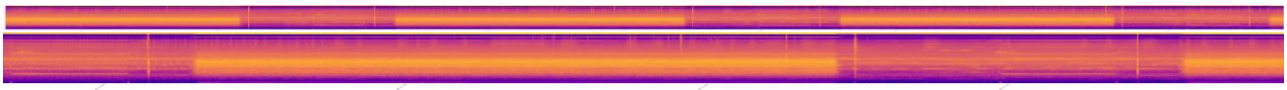

Figure 7.1-6: Time course of the frequency content of the A-weighted sound power level (waterfall diagrams) - in each case total and detailed period

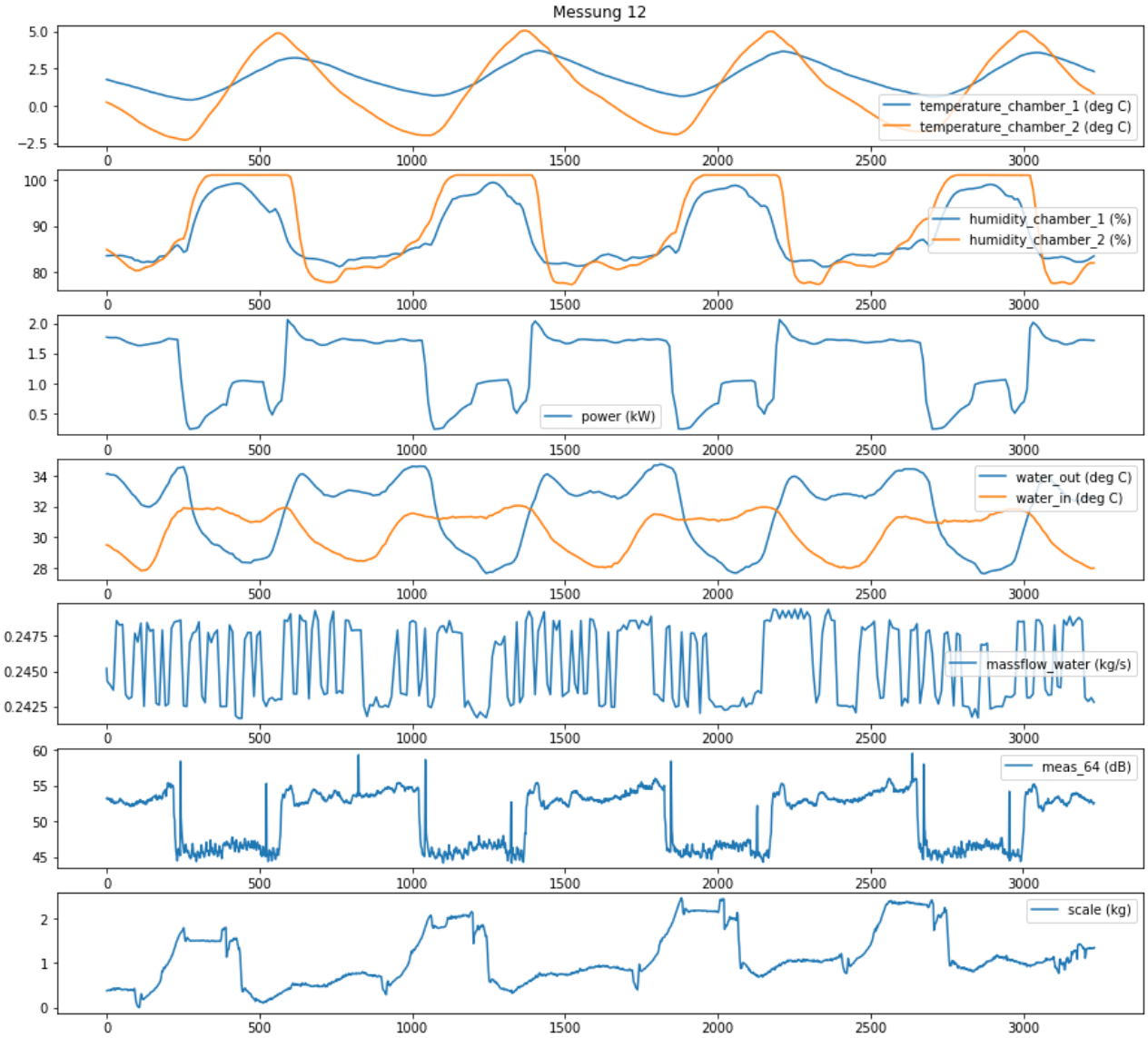

Figure 7.1-7: Time history of important climatic chamber data, weight and A-weighted sound power level for measurement Nov 18-12

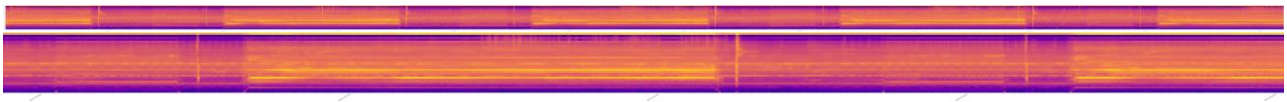

Figure 7.1-8: Time course of the frequency content of the A-weighted sound power level (waterfall diagrams) - in each case total and detailed period

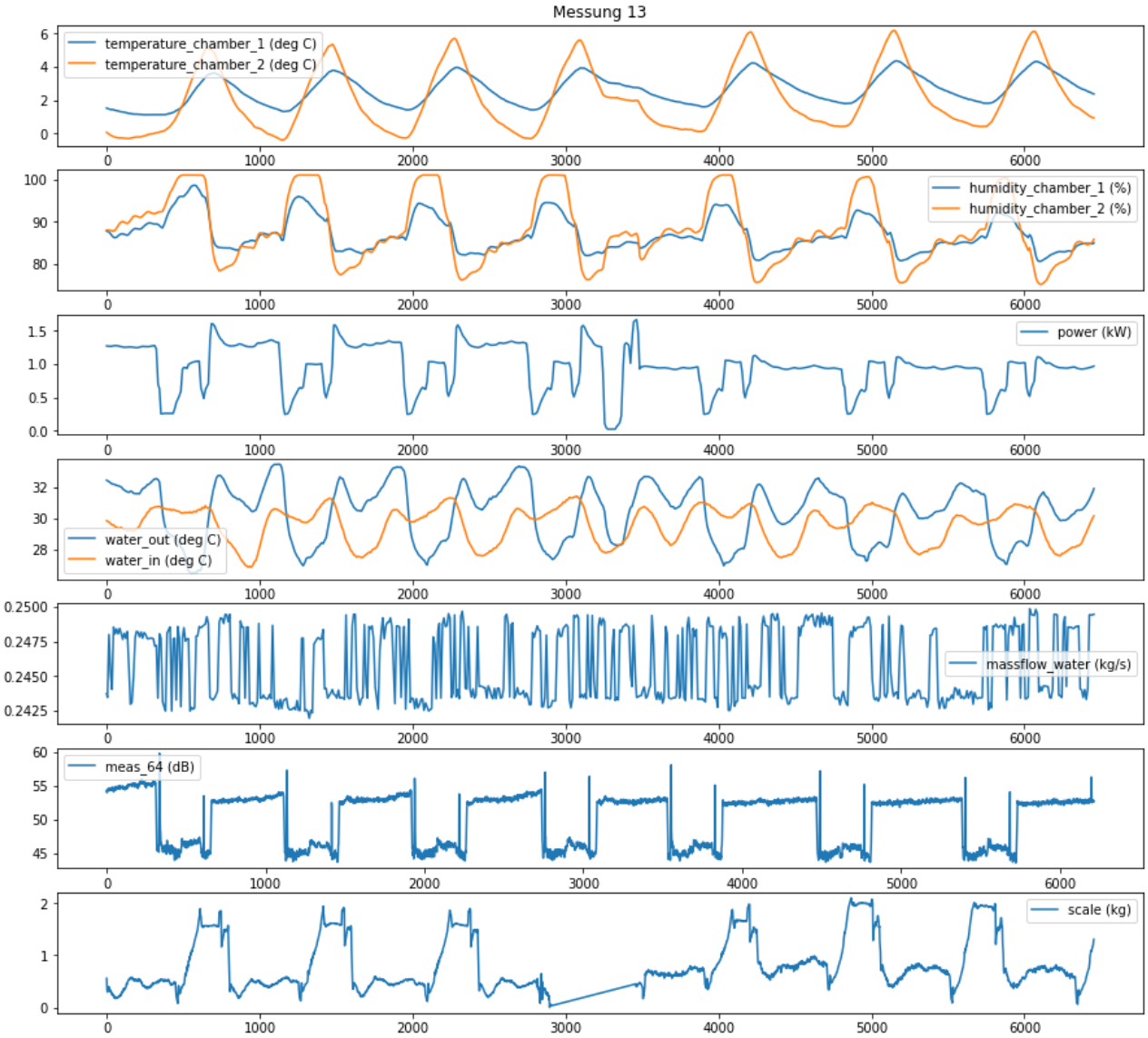

Figure 7.1-9: Time history of important climatic chamber data, weight and A-weighted sound power level for measurement Nov 18-13

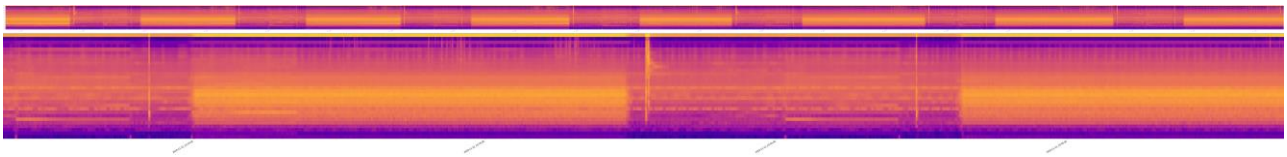

Figure 7.1-10: Time course of the frequency content of the A-weighted sound power level (waterfall diagrams) - in each case total and detailed period

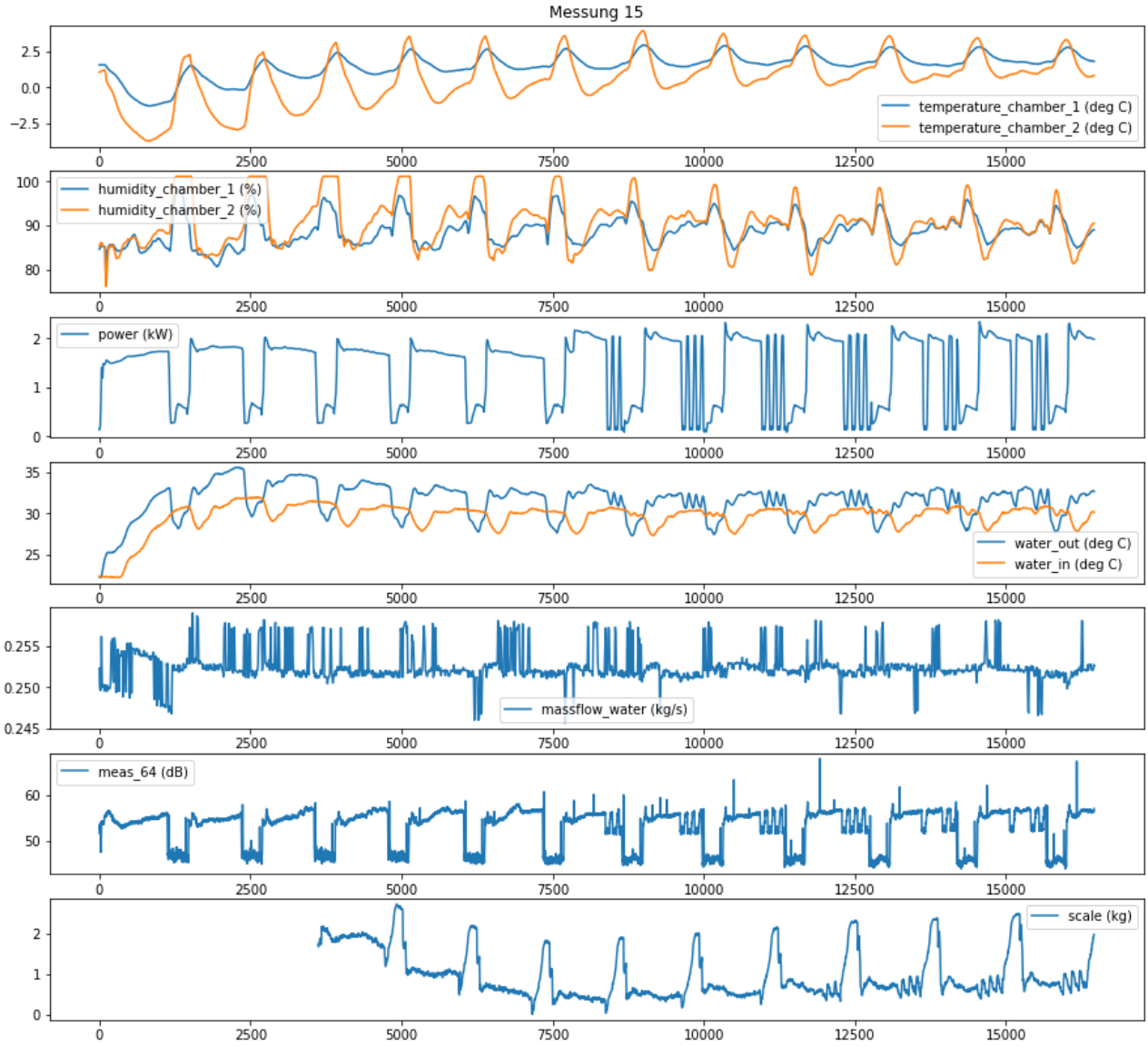

Figure 7.1-11: Time history of important climatic chamber data, weight and A-weighted sound power level for measurement Nov 18-15

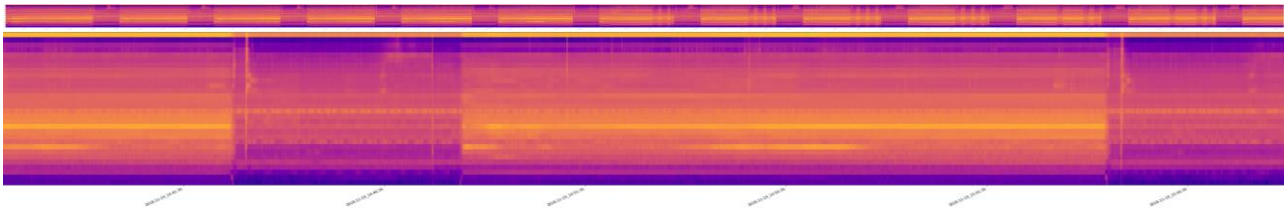

Figure 7.1-12: Time course of the frequency content of the A-weighted sound power level (waterfall diagrams) - in each case total and detailed period

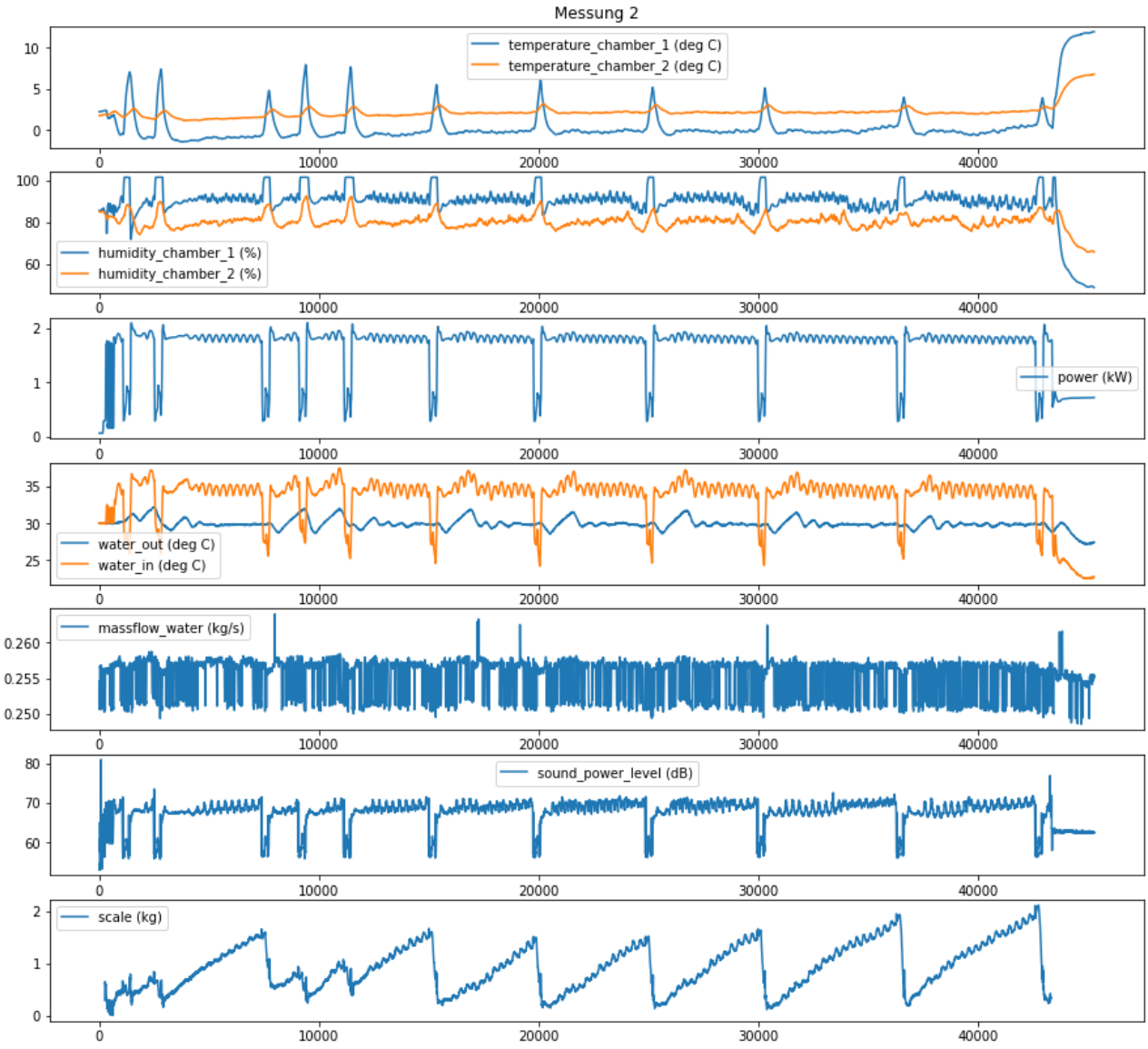

Figure 7.1-13: Time history of important climatic chamber data, weight and A-weighted sound power level for measurement Mar 19-02

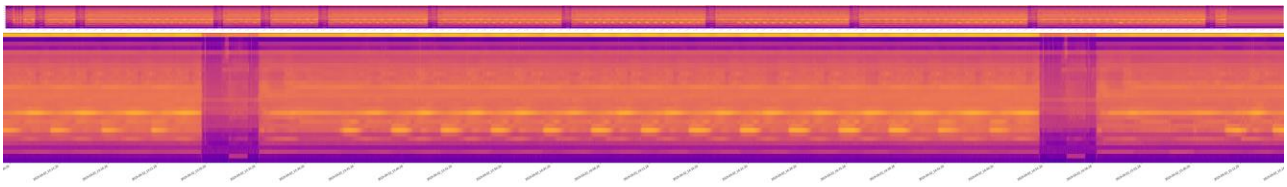

Figure 7.1-14: Time course of the frequency content of the A-weighted sound power level (waterfall diagrams) - in each case total and detailed period

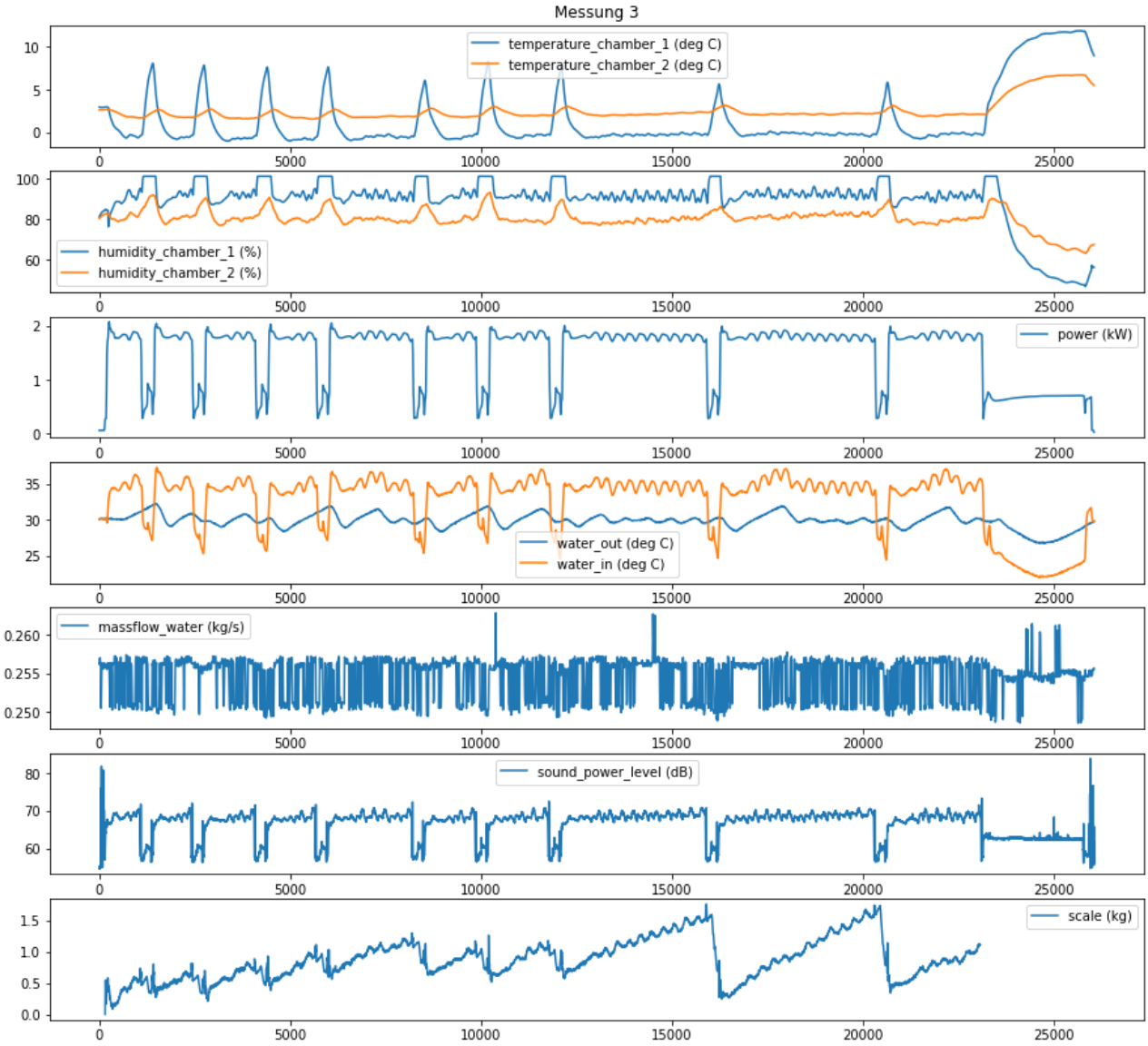

Figure 7.1-15: Time history of important climatic chamber data, weight and A-weighted sound power level for measurement Mar 19-03

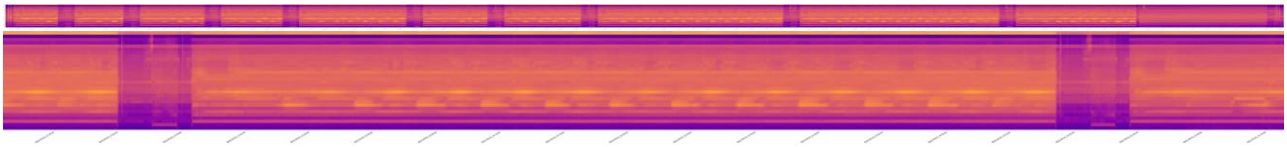

Figure 7.1-16: Time course of the frequency content of the A-weighted sound power level (waterfall diagrams) - in each case total and detailed period

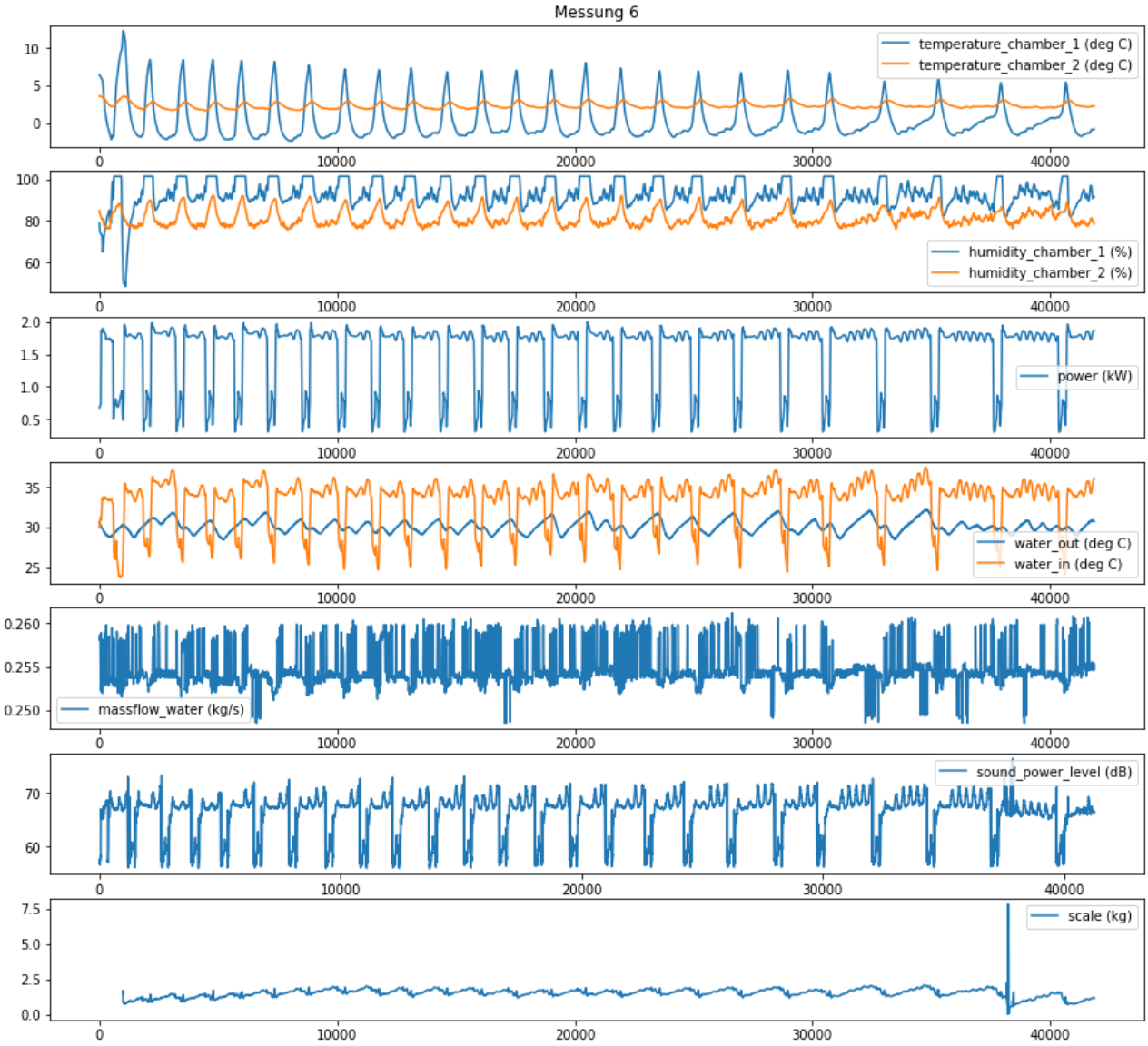

Figure 7.1-17: Time history of essential climatic chamber data, weight and A-weighted sound power level for measurement Mar 19-06

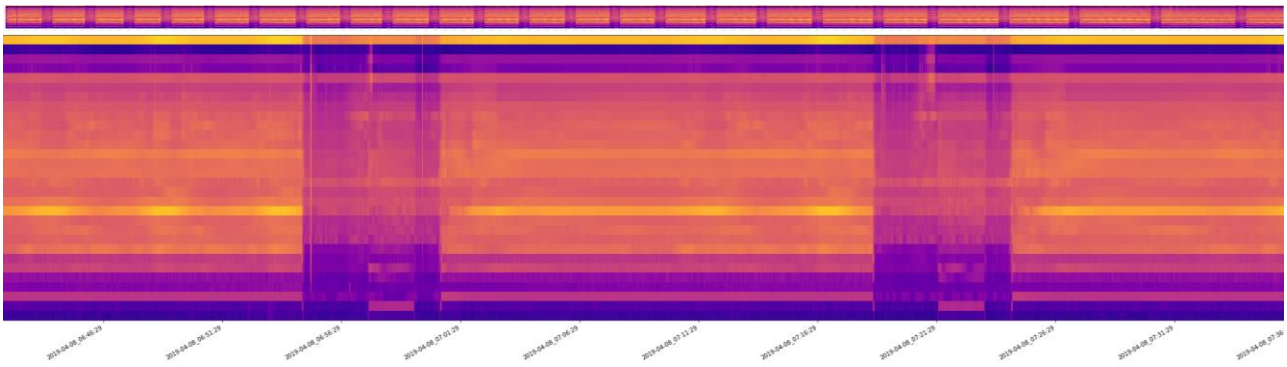

Figure 8.1-18: Time course of the frequency content of the A-weighted sound power level (waterfall diagrams) - in each case total and detailed period

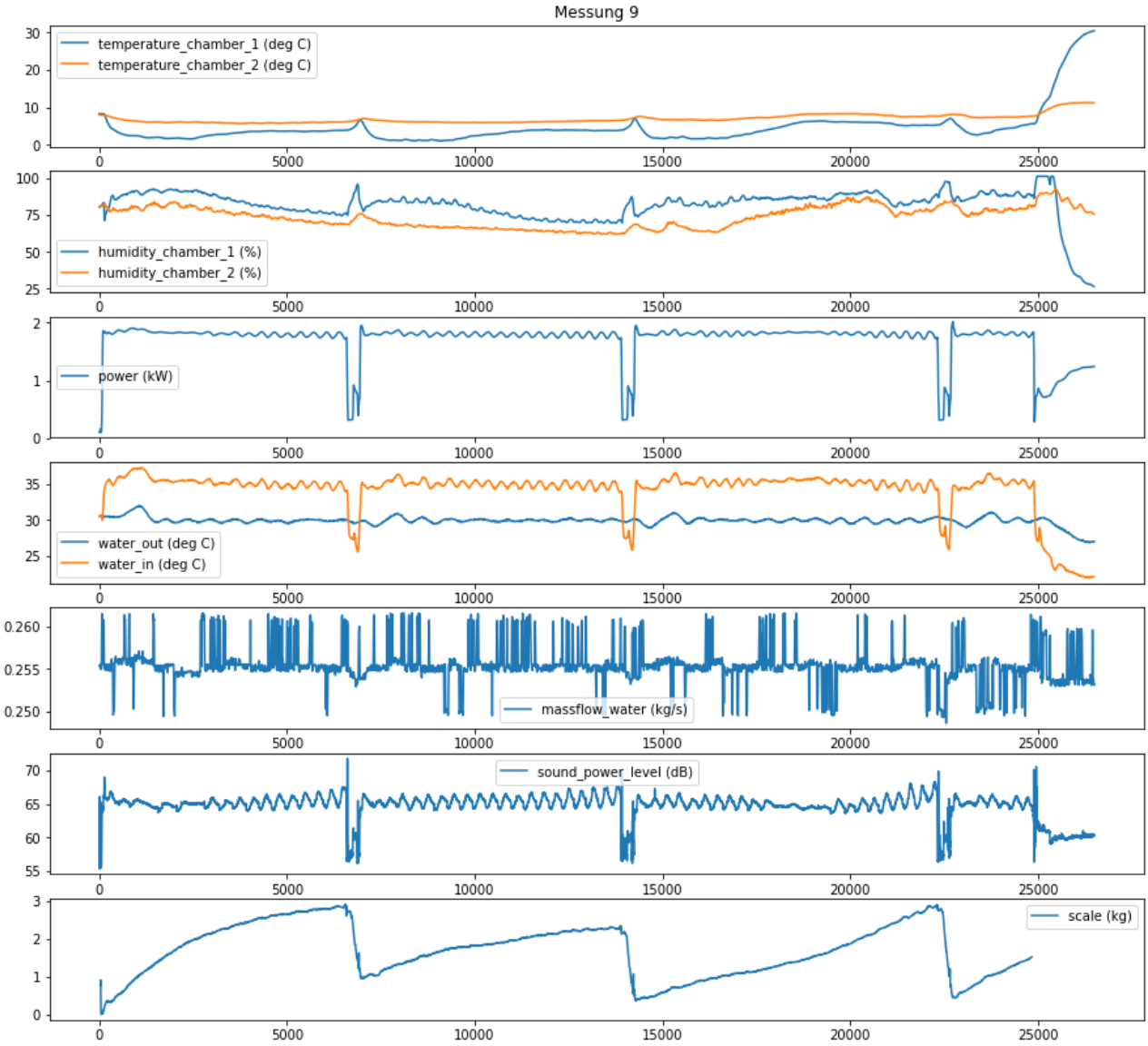

Figure 7.1-19: Time history of important climatic chamber data, weight and A-weighted sound power level for measurement Mar 19-09

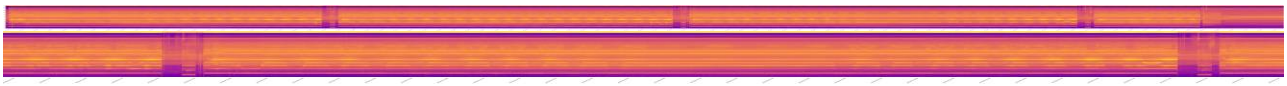

Figure 7.1-20: Time course of the frequency content of the A-weighted sound power level (waterfall diagrams) - in each case total and detailed period

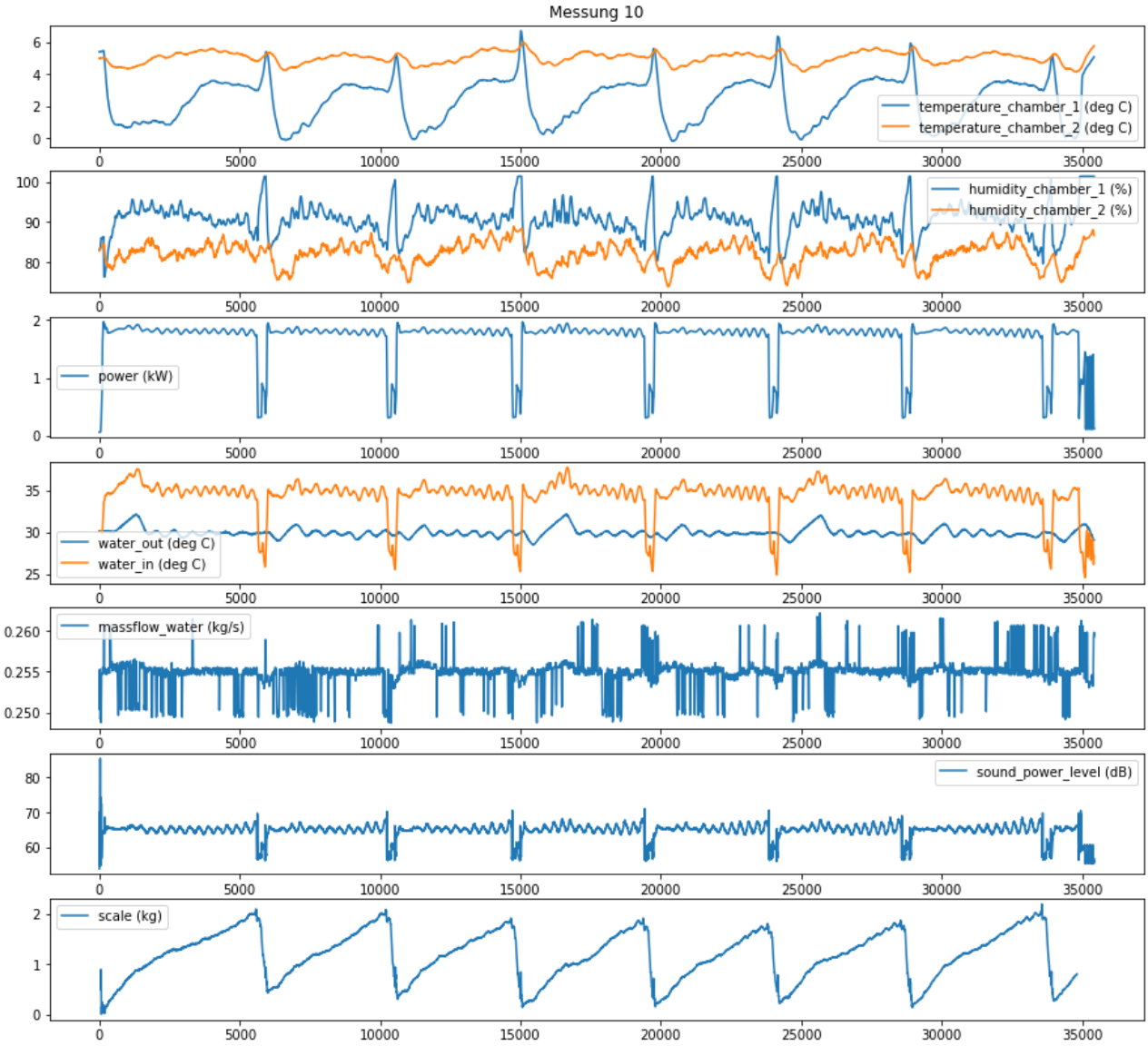

Figure 7.1-21: Time history of important climatic chamber data, weight and A-weighted sound power level for measurement Mar 19-10

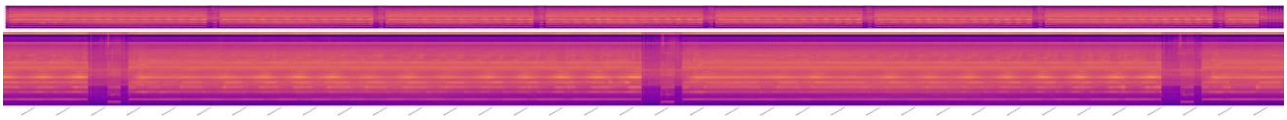

Figure 7.1-22: Time course of the frequency content of the A-weighted sound power level (waterfall diagrams) - in each case total and detailed period

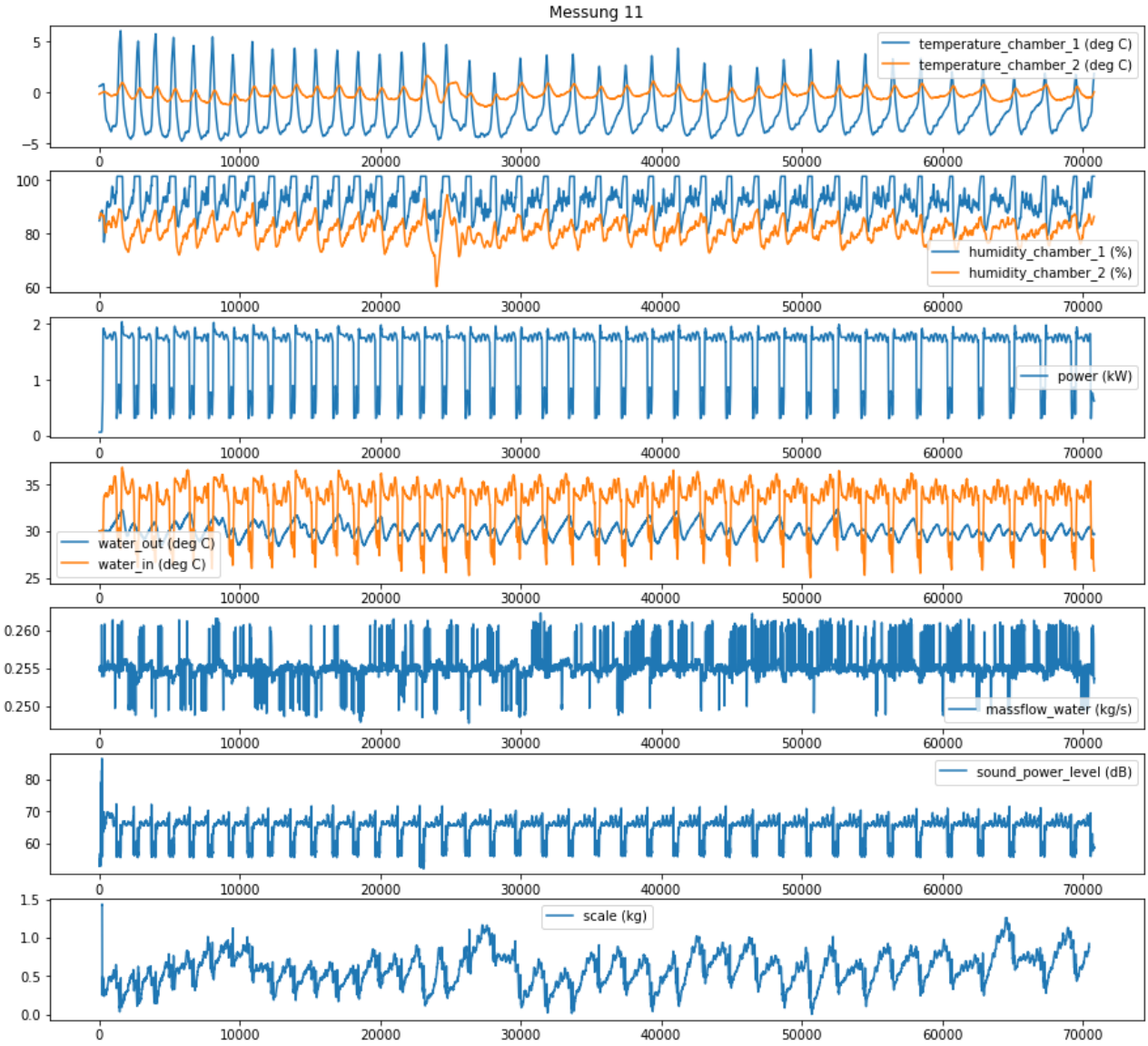

Figure 7.1-23: Time history of important climatic chamber data, weight and A-weighted sound power level for measurement Mar 19-11

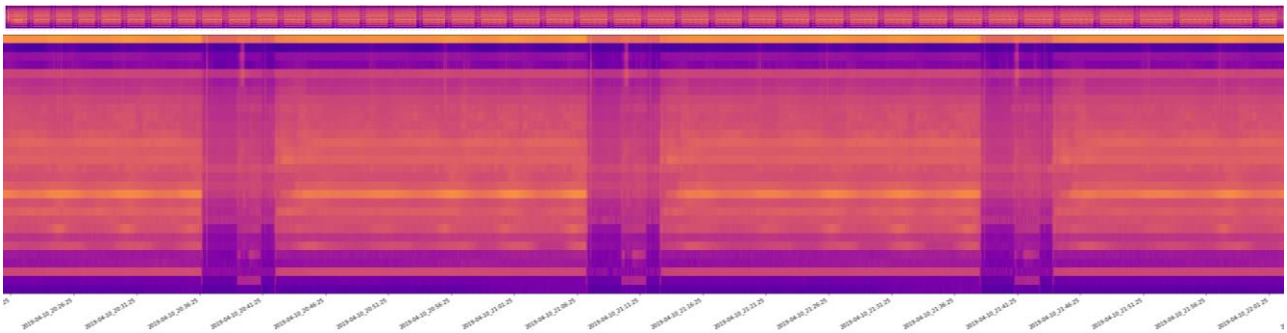

Figure 7.1-24: Time course of the frequency content of the A-weighted sound power level (waterfall diagrams) - in each case total and detailed period

7.2 Report on the perception tests in the SilentAirHP project Austrian Academy of Sciences, Institute for Sound Research, Christian Kaseß, 22 March 2019

7.2.1 Task definition

The A-weighted level is the most important variable for quantifying environmental noise. A large part of the guidelines and limit values refer to this frequency weighting, which is modeled on hearing. For the perception of environmental noise, including the sound immissions caused by heat pumps, it is known that not only the energy summed sound level but also other quantities more closely related to the function of hearing are in part more consistent with experimental data (see e.g. [1] and [2]). These include above all loudness, i.e. the perception of loudness, but also psychoacoustic roughness due to rapid amplitude modulations or sharpness due to high-frequency components.

The aim of the present study was to psychoacoustically evaluate noise from heat pumps in different directions and by applying different, potentially noise-reducing, measures. Stationary noises of 4 different heat pump variants were investigated[7]:

- Original condition
- Heat pump with diffuser
- Heat pump with deflection
- Heat pump with deflection and splitter silencer

Emission measurements in 4 microphone positions at a height of 127 cm above the floor were selected (including microphone position in the acoustic dome):

- 0°: Fan axis air inlet (B5)
- 180°: Fan axis air outlet (E5)
- 90°, 270°: Normal to the fan axis (C6, F6)

7.2.2 Methods

Test persons

A total of 20 normal-hearing subjects were available for the perception tests, 10 of whom were female and 10 male. The average age was 28.6±6.6 years. If data were not yet available, the hearing threshold was determined by means of a hearing test in the frequency range between 125 and 8000 Hz. All subjects had thresholds below 20 dB with one exception, which had a slightly elevated threshold of 30 dB at 8000 Hz. Since in this test the same noise was presented in both ears, this test person was nevertheless included in the study.

Noise selection

In order to guarantee comparable operating conditions across the different measures, noises 60 seconds after the end of a de-icing cycle were used. The duration was selected as 5

[7] Im Angebot wurde von 5 Wärmepumpenvarianten ausgegangen. Da verschiedene Richtungen ebenfalls untersucht wurden ergeben sich nun 16 Varianten insgesamt

seconds, as stated in the proposal. This is a usual signal length in this range and represents a compromise. On the one hand the test person should get an impression of the signal, on the other hand the whole test should not take too long in order not to lose concentration.

Annoyance assessment

On the basis of the data provided, a free size estimation was performed, which has already been used for similar questions [1] [2] [3].

This differs from other size estimates in that no reference scale is given (e.g. from not at all to very annoying). This means that no absolute annoyance can be derived, but only the change in annoyance as a function of experimental parameters. This is not a major limitation in the present project, since the main interest of the study is the change in sensation when the acoustic parameters change. Furthermore, the specification of absolute annoyance in the laboratory is difficult per se, since it is strongly context-dependent [4].

With free size estimation, the test persons can freely select the range of numbers, but an important requirement is that a double perceived annoyance should be represented as twice as high a numerical value and that numbers less than or equal to 0 are not allowed. It is therefore always possible to specify a greater annoyance if a stimulus is more annoying than all previously heard.

In the test design, the different measured conditions were used. Furthermore, 8 samples with pink noise at different levels in the range of the A-level of the heat pump signals were added. This serves to make the results more comparable with later studies (see e.g. [5])[8].

Three runs were performed, with each run containing each stimulus three times. Thus, each condition was tested ten times. The presentation of the sounds in each run was randomized. Between the runs, the subjects had to have a break of at least 5 minutes.

Data preparation and evaluation

Psychoacoustic and acoustic parameters

The acoustic parameters (including psychoacoustically motivated parameters) for the 5 seconds long sounds were calculated using the Matlab toolbox psysound3 [6]. These included Glassberg and Moore tepidity [7], roughness [8], tonal quality [9], sharpness and loudness variation [10]. Furthermore, A, B, and C-frequency weighted levels (time weighting almost) were calculated. Of these, both the median and the 5% percentiles (the value that is exceeded in 5% of time) were calculated, e.g. S50 and S5 for median and 5% sharpness. From the loudness, the volume level in phon was also calculated.

Annoyance

In this test it can happen that test persons mistype. If such mistakes were reported (a total of 4 spread over 3 subjects), and these were clearly traceable (all 4 cases), a correction was made and recorded.

[8] Das rosa Rauschen ersetzen die im Angebot erwähnten Geräusche anderer Lärmquellen, da eine Auswahl solcher Geräusche sehr willkürlich wäre und zu großen Schwankungen unterliegen würde.

The judgments were logarithmized to base 2, i.e. an increase in log annoyance by 1 means a doubling. One outlier detection (mean value ± 3-fold standard deviation) per condition and subject did not result in any further outliers.

Consistency of the test persons' judgements

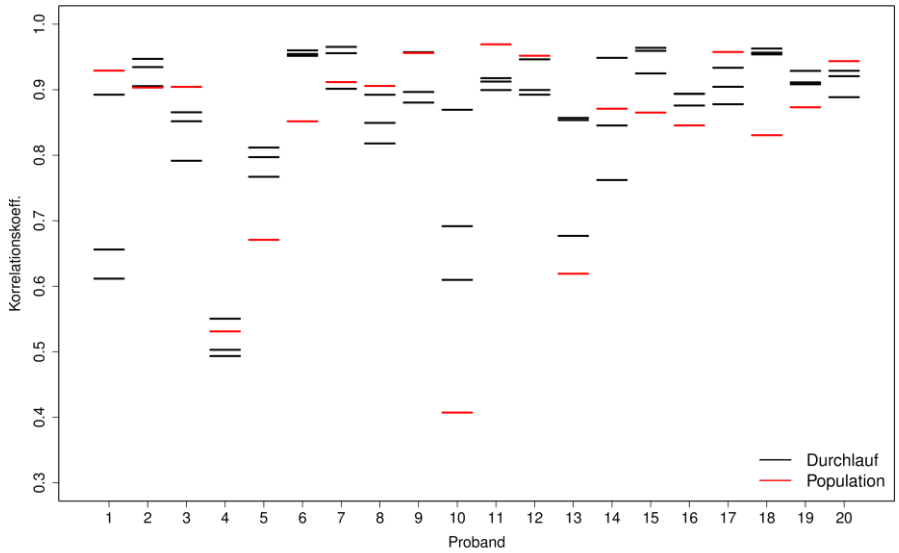

Figure 7.2-1: Correlation of all scores including pink noise per respondent between the passes (black) and compared to the judgement averaged over the group.

Figure 7.2-1 shows the correlations over the three runs (all 3 possible combinations) per respondent, whereby here the three presentations per condition and run were averaged. Overall, the judgements about the repetitions are very consistent, with the exception of one test person (VP 4). If the mean judgements per respondent are correlated with the mean overall judgement, two significant points are obtained. The test person with relatively inconsistent judgements shows a low correlation with the overall judgement. Secondly, 3 subjects seem to form a slightly different judgement than the rest (VPs 5, 10 and 13). This is expressed by the fact that, especially in the latter two (VPs 10 and 13), the annoyance values of the heat pump are significantly below the pink noise at the same A-level, whereas the rest of the test persons tend to evaluate this in the opposite way.

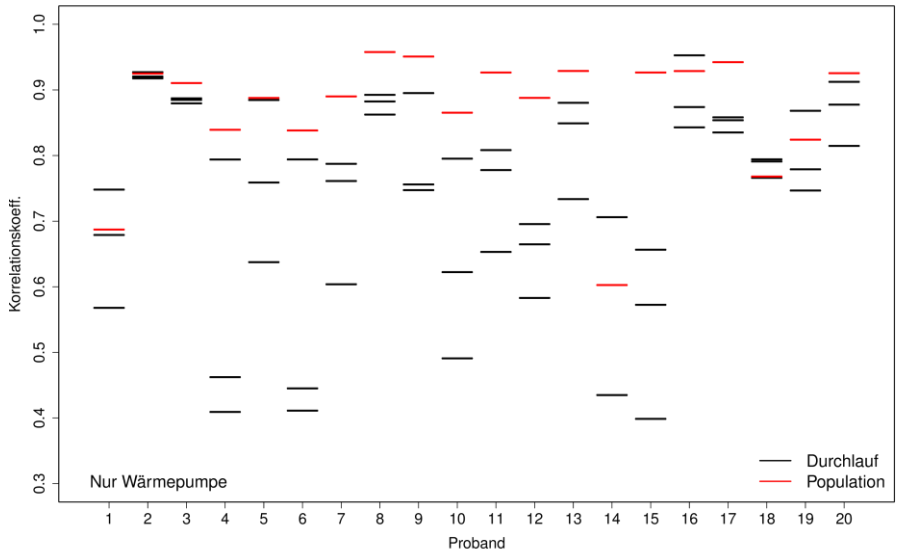

Figure 7.2-2: Correlation of the ratings of the heat pump noises per respondent between the passages (black) and compared to the judgement averaged over the group.

If only the correlations of the heat pump noises are considered (Figure 7.2-2), there is an increased scattering of the correlation, which is to be expected due to the reduced level range and the very different noise characteristics. With regard to the population mean, the picture also changes. The consistency to the mean judgment is very high. Interestingly, VPs 5, 10 and 13 do not stand out here and VP 4 also shows a greater agreement. VP 1 but especially VP 14 show a slightly reduced consistency here. Basically, however, the test persons assess the differences in the heat pump noises in a similar way.
For further analysis, the mean value of all assessments per respondent was calculated and the mean value of all mean assessments per respondent was subtracted to normalise the data (e.g. [2] [1]). For the group mean value, these proband-specific judgements were averaged over the test persons per assessment.

Statistical analysis

All statistical evaluations were performed with the software R [11]. Based on the mean judgements for the heat pump noise per respondent, the influence of measure and measuring position was examined by means of a Repeated-Measurements-Analysis-of Variance (ANOVA for dependent data). The R-package ez [12] was used for this. Based on the results of the ANOVA, post-hoc tests were performed using paired t-tests [13] [14].
In order to investigate the relationship between different acoustic characteristics of the noise and the annoyance judgement, a step-by-step procedure was used in which explanatory variables can be successively added or removed (stepAIC in the MASS package [15]). The Bayes Information Criterion (BIC [16]) was used as a quality measure for the model, which takes into account both model errors and complexity of the model.

7.2.3 Results

Acoustic and psychoacoustic quantities

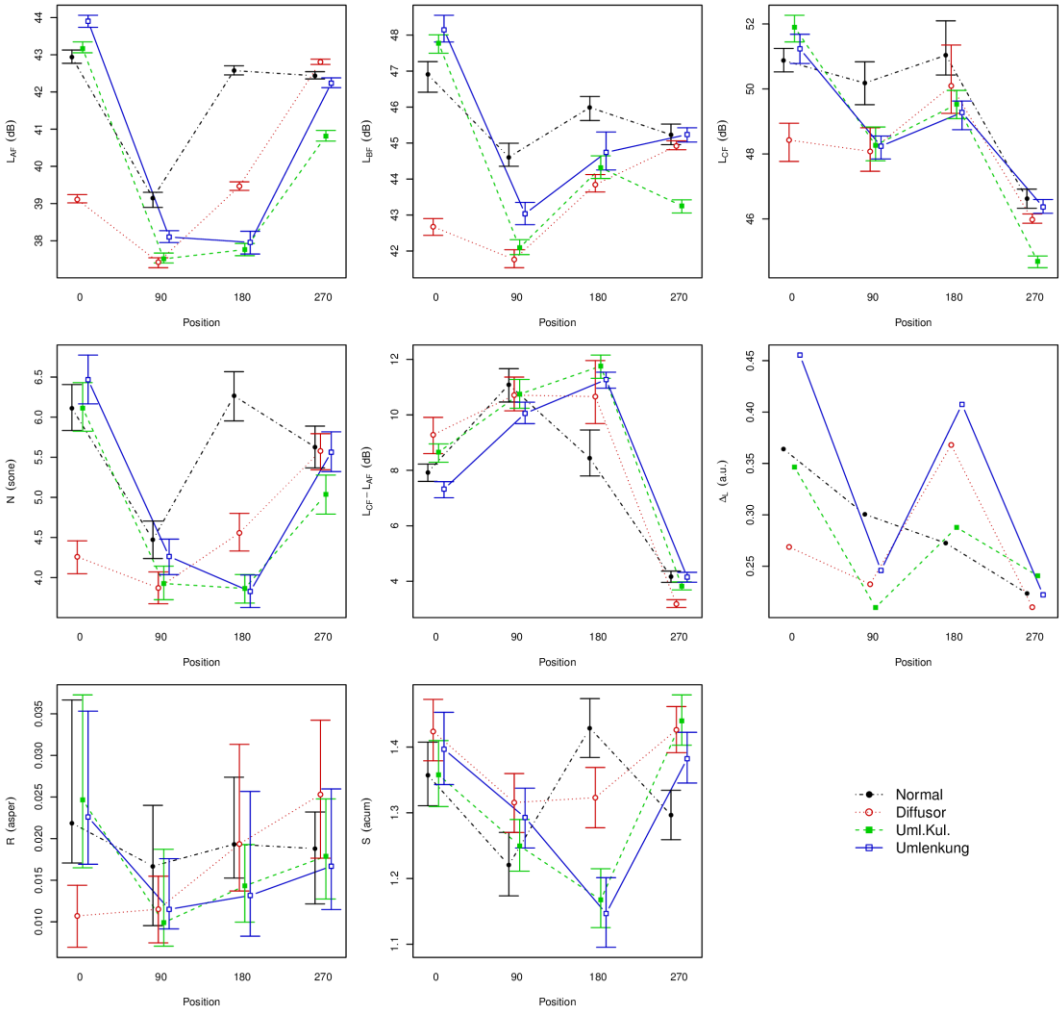

Figure 7.2-3: Different acoustic quantities depending on the direction for the four conditions. The error bars show the 25% and 75% percentiles

If we look at the sound pressure level or loudness N (Figure 7.2-3), we can see that in the direction of the ventilation outlet (180°) the highest levels/loudnesses only occur in the original state whereas at the inlet only the diffuser causes a difference. At the sides the difference is much smaller, with much lower values at 90° than at 270°. The difference between C-weighted and A-weighted levels is often used as a measure for the low frequency components. At 270° there is a much smaller difference which indicates lower low frequency noise.

At the outlet there is also a larger difference in the sharpness S with the normal state and also the diffuser showing higher values. For the roughness R the differences are relatively small compared to the scattering apart from the lower roughness of the diffuser in the inlet direction. Figure 7.2-4 shows the same data but as a function of the measure. Here it is clearly seen that the lateral positions are rather less influenced by the respective measure.

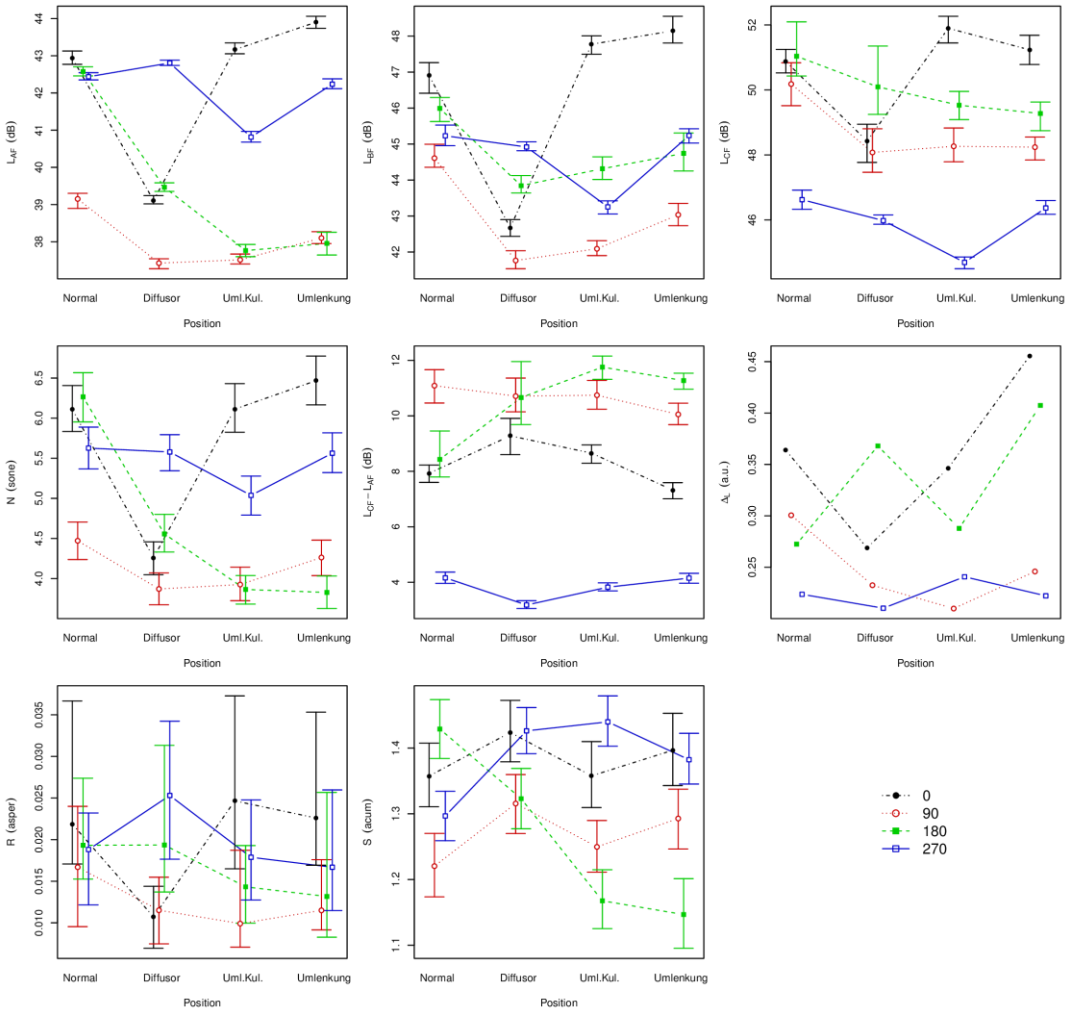

Figure 7.2-4: Different acoustic quantities depending on the conditions for the four directions

Annoyance as a function of position and state

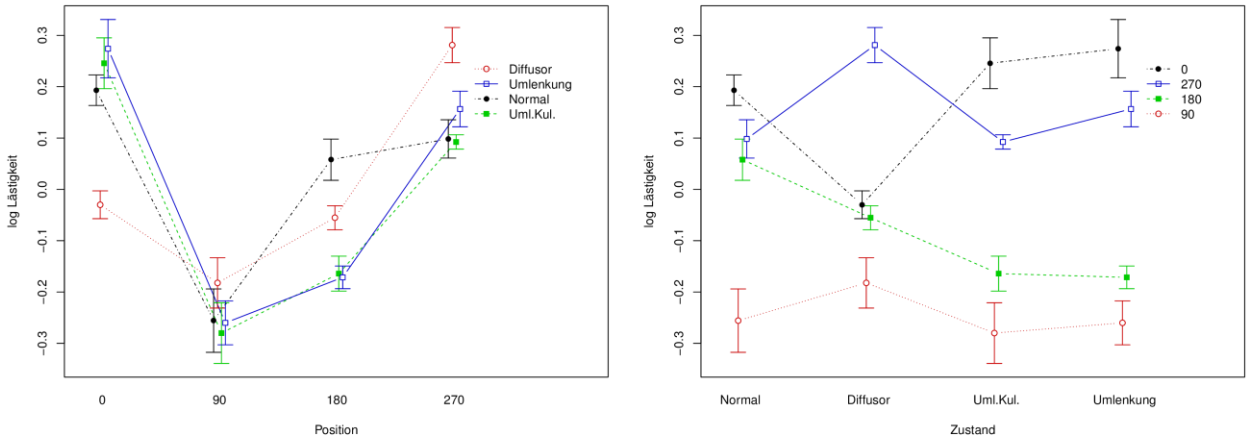

Figure 7-2.5: Annoyance judgements as a function of position and heat pump condition

Figure 7-2.5 shows the annoyance judgements as a function of the condition and position[9]. The ANOVA showed a significant main effect of position ($p<0.0001$) and also a significant interaction between position and state ($p<0.0001$). Mauchly's test showed a violation of the sphericity assumption for both effects. After correction according to Greenhouse-Geisser [17], both effects were still significant with $p<0.0001$. The condition alone showed no significant changes in annoyance.

Due to the significant interaction, this is first examined in detail before the main effect of the position is considered. The pairwise interactions are shown in Figure 7.2-6 and Figure 7.2-7 and are now systematically analyzed.

[9] With the results it is important to note that in three states, due to a problem in processing, a perceptible click was present at the end of the noise (180° normal state and much less at 180° deflection and 0° normal state). A possible influence on the annoyance judgement cannot be completely excluded, but seems unlikely. The three conditions show neither an increased variance over the test persons nor a conspicuousness with regard to loudness or level.

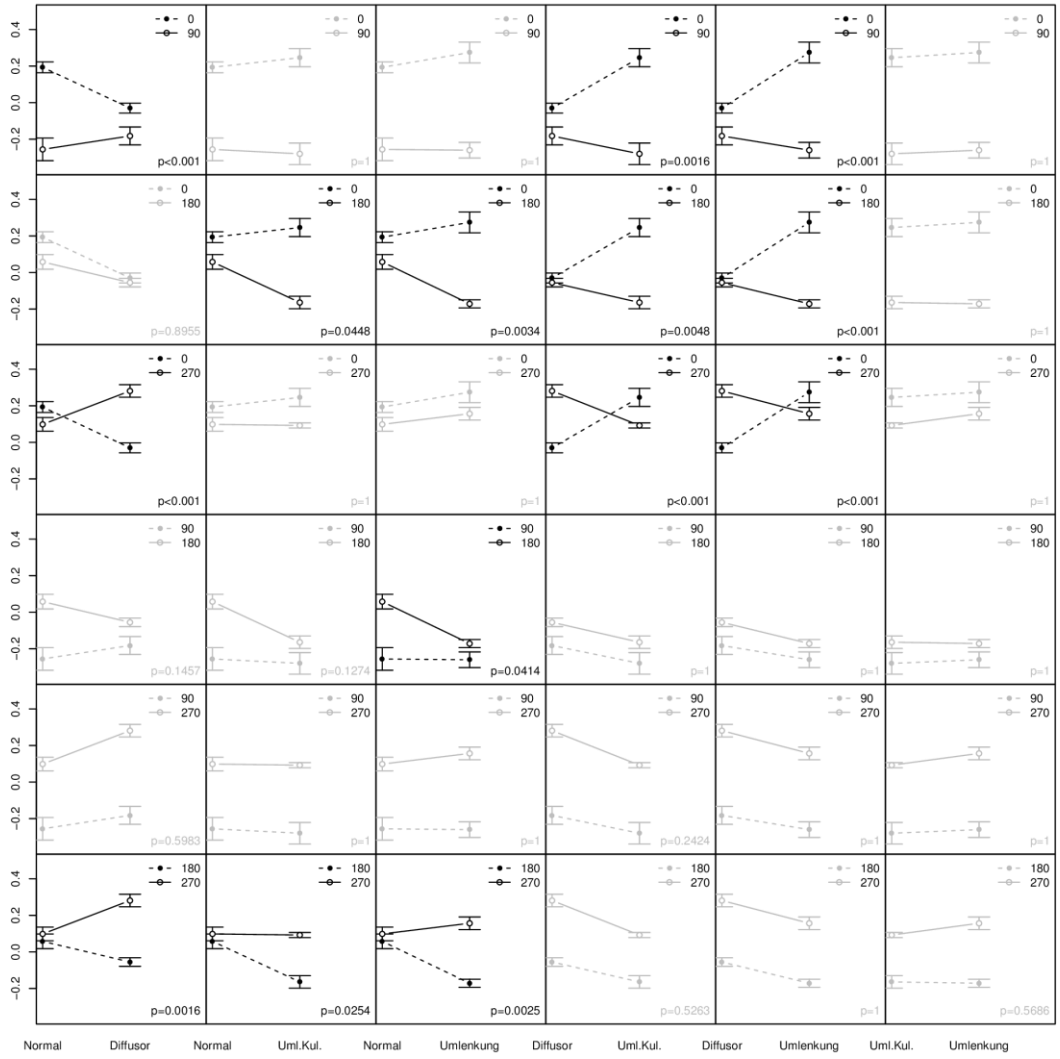

Figure 7.2-6: Pairwise interactions between the factor levels of position and state. Grey means that the effect is not significant

Interaction normal vs. Diffuser

Here the interaction effect is created by the fact that the annoyance along the fan axis (0° and 180°) is reduced by the diffuser, whereas on the sides this effect tends to be opposite.

Interaction normal vs. deflection + splitter silencer

Here, all (weakly) significant interactions are to be justified by the deviating change at 180°, where the annoyance is reduced by the measure. For the pure redirection the effect is comparable.

Interaction diffuser vs. Deflection

The perceived annoyance is lower with the diffuser at 0°, otherwise it tends to be higher. Due to this difference at 0° the interactions are significant. The splitter silencer does not produce any additional significant effects here.

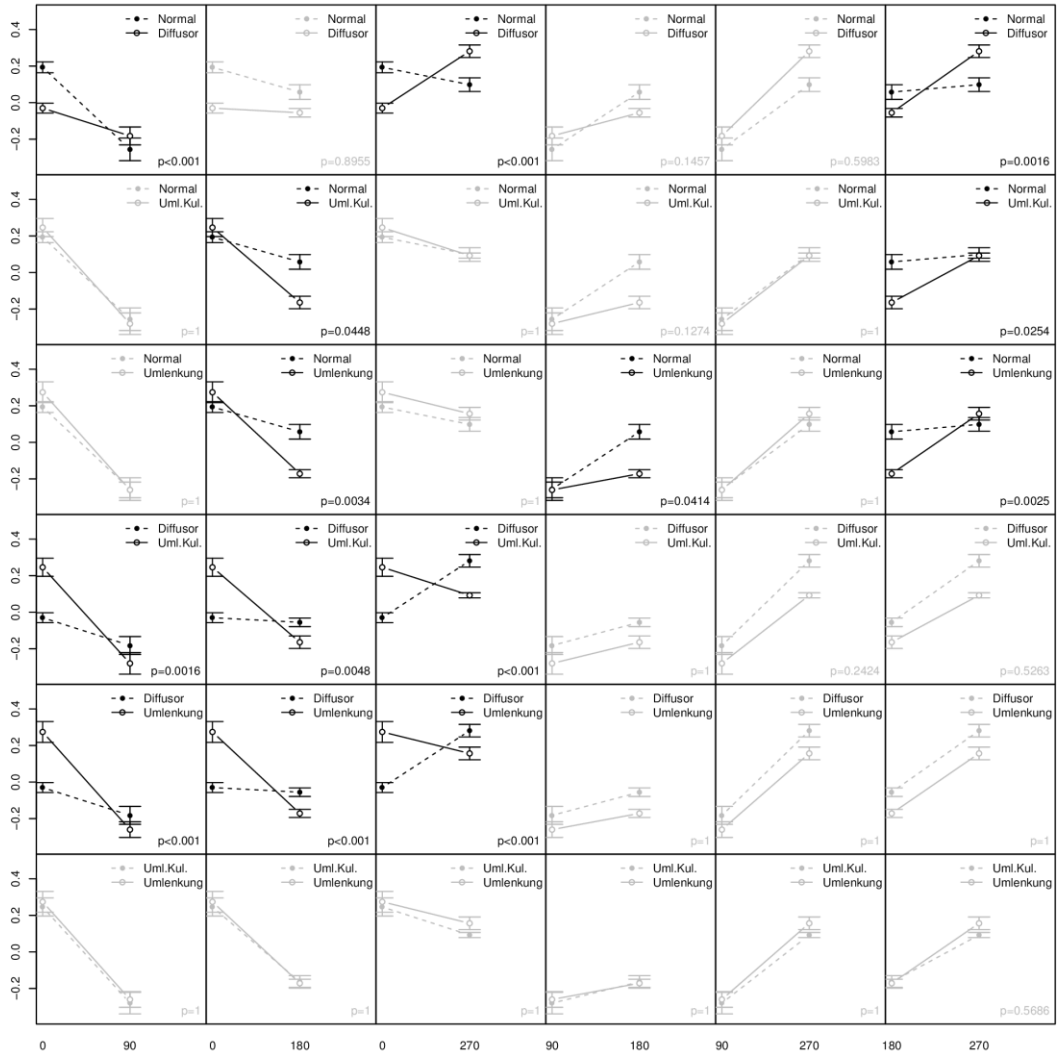

Figure 7.2-7: Pairwise interactions between the factor levels of position and state. Grey means that the effect is not significant

Main effect position

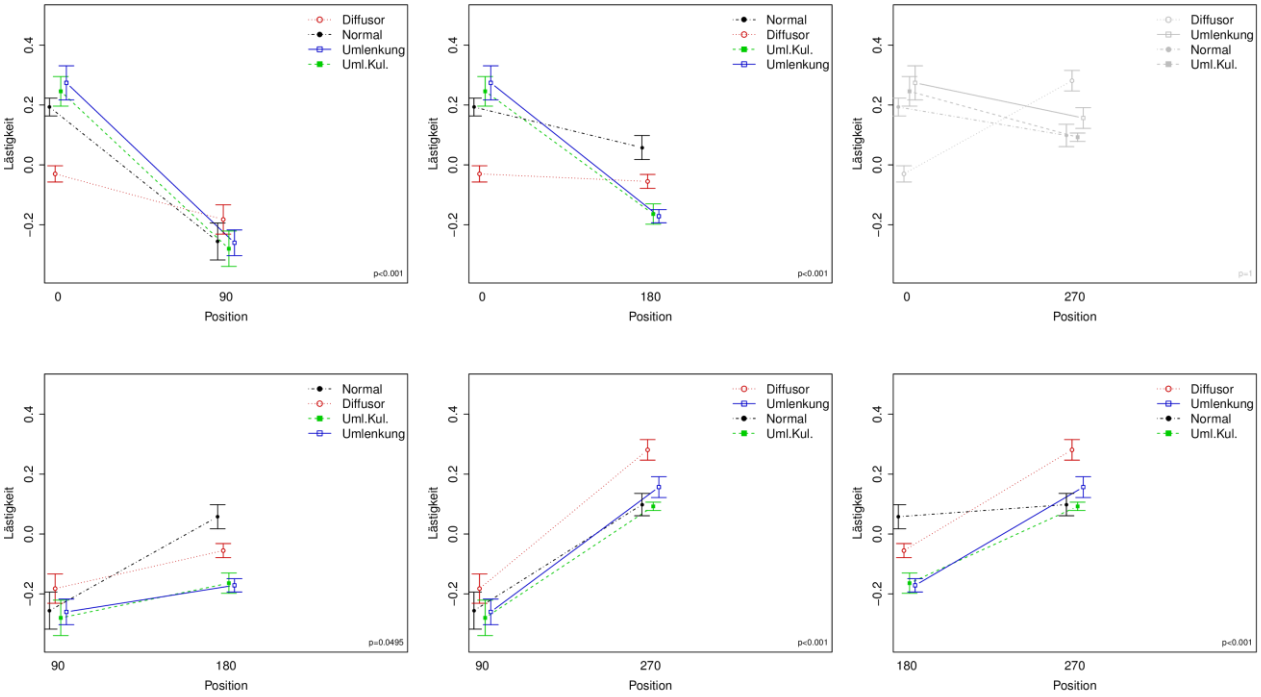

Figure 7.2-8: Interaction graphics for the pairwise main effect contrasts of the factor position and the factor state. Grey means that the main effect contrast is not significant for the position

A post-hoc test (Figure 7.2-8) shows that all possible differences between the directions are significant with the exception of the difference between 0° and 270° where the difference between 90° and 180° is just about significant. However, due to the significant interaction between position and measure, caution is required in the interpretation.
The position at 90° is perceived as significantly less annoying than the position at 0°. This shows that all interactions are purely quantitative, i.e. in every combination the average annoyance at 90° is lower.
The comparison 180° vs. 0° is similar, but the difference between these two directions is comparatively small for the diffuser. Therefore, the difference between 90° and 180° is also qualitatively the same for all measures. This also applies to the difference between 90 and 270°, whereas 180° vs. 270° is not quite clear, since the two directions of the diffuser were judged to be very similar.

Annoyance vs. acoustic characteristics

The statistical analysis showed differences in the perception of the individual conditions. The question is which acoustic characteristics are decisive for this. For this purpose, a stepwise model selection was performed using the mean annoyance judgements of the heat pump data (without pink noise).

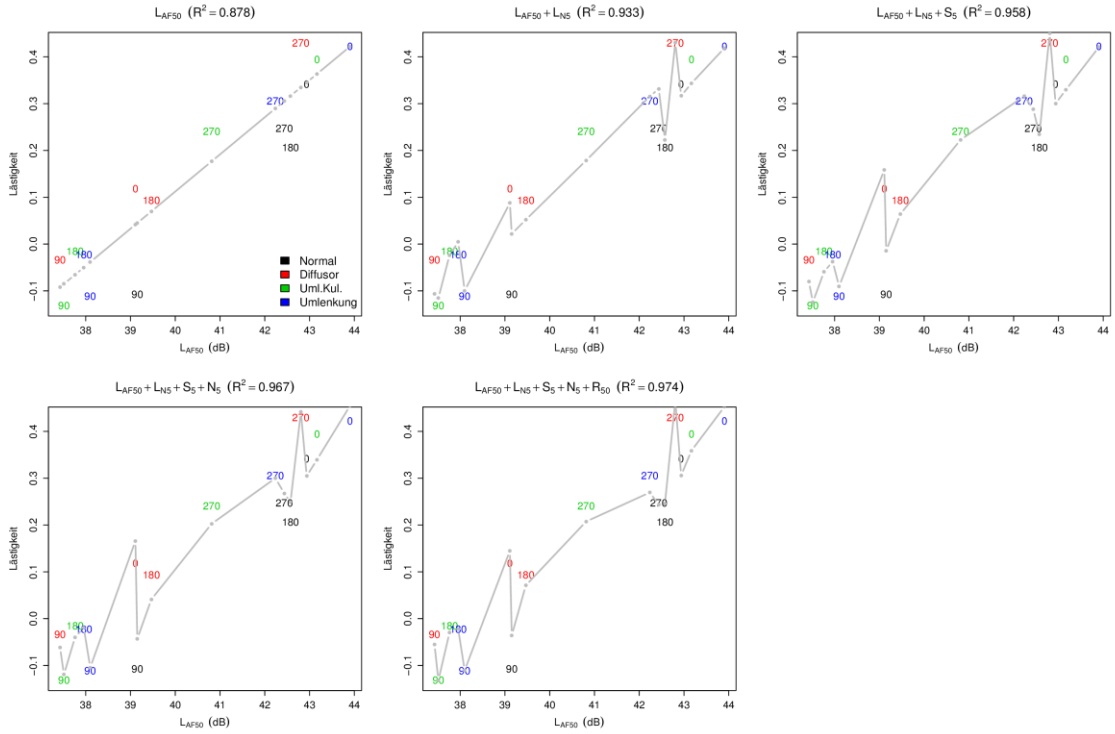

Figure 7.2-9: Annoyance as a function of the LAF50 and the gradual model selection including model fit (grey line)

The best model contained 5 acoustic variables and resulted in the following:

Logarithmic annoyance = const + 0,1640·L_{AF50} – 0,2270·L_{N5} + 0,6436·S_5 + 0,3287·N_5 + 7,3415·R_5

Figure 7.2-9 shows the relationship between the annoyance ratings for the heat pumps and the LAF50. The line shows the prediction based on the prediction of the linear model shown in the title. Furthermore, the proportion of the explained variance is also shown (R2). Here we can see that the LAF50 tends to explain the judgements and how the successively added parameters capture the existing variance more and more effectively, whereas the increase of the explained variance by the last two parameters is less than 2% (95.8% to 97.4%).

If we take only the different loudness measures (N5, N50, LN5, LN50), they explain the difference between 75% and 78%, which is significantly less than the LAF50 (approx. 87%).

In order to clarify whether the test persons deliver plausible evaluations, the pink noise was further examined. Here the loudness should explain a large part of the annoyance due to the pure scaling of the different stimuli. A correlation analysis shows that the loudness level (LN5 and LN50) explains about 99.5% of the variance, whereas an increase of about 12 phon corresponds to a doubling of the annoyance. I.e. a doubling of loudness (10 phon increase

for loudnesses > 1 sone) causes slightly less than a doubling of annoyance. With the LAF50 (99.4%), it is about 10 dB for a doubling. In comparison, the increase for heat pump data is about 16 phon or 12.5 dB (compare to 14 dB for train passing [2]).

7.2.4 Summary

The following main points have emerged from the investigations:

1. The effect of the different measures on the different acoustic and psychoacoustic measures is very strongly directional. Differences can be observed especially in levels, loudness and sharpness
2. This dependency between measure and direction also continues in perception, which is shown by a significant statistical interaction between position and state.
3. There was also a significant overall effect of the measuring position for the annoyance judgements. Due to the significant interaction with the factor measure, these effects must be interpreted with caution.
4. The differences in the annoyance judgments can be explained very well by A-level and volume level. The additional use of psychoacoustic sharpness and also roughness contribute to a better explanation.

Finally, it is important to mention that the acoustic data were emission measurements. Above all, the directional dependency can change due to distance and also due to the way the heat pump is installed. In order to investigate the directional dependency more precisely even at greater distances, measurements in corresponding situations and further perception tests would be necessary.

7.2.5 Bibliography

[1] M. Nilsson, M. Andehn and P. Lesna, „Evaluating roadside noise barriers using an annoyance-reduction criterion," *J. Acoust. Soc. Am,* Bd. 124, Nr. 6, pp. 3561-3567, 2008.

[2] C. Kasess, T. Maly, P. Majdak and H. Waubke, „The relation between psychoacoustical factors and annoyance under different noise reduction conditions for railway noise," *J. Acoust. Soc. Am,* Bd. 141, pp. 3151-3163, 2017.

[3] C. Kasess, T. Maly, W. Kluger-Eigl, E. Demmelmayr, H. Waubke, N. Ostermann and R. Blab, „Abschlussbericht Projekt "Lärmarme Rumpelstreifen"," 2017.

[4] S. FIdell, „Noise-Induced Annoyance," in *Handbook of Noise and Vibration Control*, Hoboken, New Jersey, John Wiley & Sons, 2007, pp. 316-319.

[5] G. Di, K. Lu and X. Shi, „An optimization study on listening experiments to improve the comparability of annoyance ratings of noise samples from different experimental sample sets," *Int J Environ Res Public Health,* Bd. 15, Nr. 3, 2018.

[6] D. Cabrera, S. Ferguson, F. Rizwi and E. Schubert, „PsySound3: software for acoustical and psychoacoustical analysis of sound recordings," in *Proceedings of the 13th International Conference on Auditory Display*, Montreal, Canada, 2007.

[7] B. Glasberg and B. Moore, „Derivation of Auditory Filter Shapes from Notched Noise Data," *Hearing Research,* Bd. 47, pp. 103-137, 1990.

[8] P. Daniel and R. Weber, „Psychoacoustical roughness: implementation of an optimized model," *Acustica,* Bd. 83, pp. 113-123, 1997.

[9] E. Terhardt, G. Stoll and M. Seewan, "Algorithm for extraction of pitch and pitch salience from complex tonal signals," *J. Acoust. Soc. Am,* vol. 71, pp. 679-688, 1982.

[10] J. Chalupper and H. Fastl, „Dynamic Loudness Model (DLM) for Normal and Hearing-Impaired Listeners," *Acta Acustica United with Acustica,* Bd. 88, pp. 378-386, 2002.

[11] R Core Team, „R: A language and environment for statistical computing. R Foundation for Statistical Computing," 2018.

[12] M. Lawrence, „Easy Analysis and Visualization of Factorial Experiments. R package version 4.4-0.," 2016.

[13] H. Keselman, „Testing treatment effects in repeated measures designs: An update for psychophysiological researchers," *Psychophys.,* Bd. 35, p. 470–478, 1998.

[14] H. Keselman, J. Keselman and J. Shaffer, „Multiple pair-wise comparisons of repeated measures means under violation of multi-sample sphericity," *Psychol. Bull.,* Bd. 110, p. 162–170.

[15] W. Venables and B. Ripley, Modern Applied Statistics with S. Fourth Edition, New York: Springer, 2002.

[16] G. Schwarz, „Estimating the dimension of a model," *Annals of Statistics,* Bd. 6, Nr. 2, p. 461–464, 1978.

[17] S. Greenhouse and S. Geisser, „On methods in the analysis of profile data," *Psychometrika,* Bd. 24, pp. 95-112, 1959.

8 Contact

DI Dr. Christoph Reichl
AIT Austrian Institute of Technology GmbH
Giefinggasse 4
1210 Wien
Phone: +43 50550 6605
Fax: +43 50550 6679
E-Mail: Christoph.Reichl@ait.ac.at
www.ait.ac.at
https://www.ait.ac.at/themen/sustainable-thermal-energy-systems/projects/silentairhp/